MAGNETIC LOCALIZATION AND CLOSED-LOOP PROPULSION FOR ACTIVE CAPSULE ENDOSCOPY USING A SINGLE MAGNETIC DIPOLE SOURCE

by

Katie M. Popek

A dissertation submitted to the faculty of
The University of Utah
in partial fulfillment of the requirements for the degree of

Doctor of Philosophy

in

Computing

School of Computing

The University of Utah

August 2017

The University of Utah Graduate School

STATEMENT OF DISSERTATION APPROVAL

The dissertation of **Katie M. Popek**
has been approved by the following supervisory committee members:

Jake J. Abbott ,	Chair(s)	**February 17, 2017** Date Approved
Thomas C. Henderson ,	Member	**February 17, 2017** Date Approved
Tucker Hermans ,	Member	**February 17, 2017** Date Approved
John M. Hollerbach ,	Member	**February 17, 2017** Date Approved
Stephen A. Mascaro ,	Member	**February 16, 2017** Date Approved

by **Ross T. Whitaker** , Chair/Dean of
the Department/College/School of **Computing**
and by **David B. Kieda** , Dean of The Graduate School.

ABSTRACT

Closed-loop control of wireless capsule endoscopes is an active area of research because it would drastically improve screening of the gastrointestinal tract. Traditional endoscopic procedures are unable to view the entire gastrointestinal tract and current commercial wireless capsule endoscopes are limited in their effectiveness due to their passive nature. This dissertation advances the field of active capsule endoscopy by developing methods to localize the full six-degree-of-freedom (6-DOF) pose of a screw-type magnetic capsule while it is being propelled through a lumen (such as the small intestines) using an external rotating magnetic dipole. The same external magnetic dipole is utilized for both propulsion and localization.

Hardware was designed and constructed to enable testing of the magnetic localization and propulsion methods, including a robotic end-effector used as the external actuator magnet, and a prototype capsule embedded with Hall-effect sensors. Due to the use of a rotating magnetic field for propulsion, at any given time, the capsule can be in one of three regimes: synchronously rotating with the applied field, in "step-out" where it is free to move but the external field is rotating too quickly for the capsule to remain synchronously rotating, or completely stationary. We show that it is only necessary to distinguish whether or not the capsule is synchronously rotating (i.e., a single localization method can be used for a capsule in either the step-out or stationary regimes). Two magnetic localization methods are developed. The first uses nonlinear least squares to estimate the capsule's pose when it has no (or approximately no) net motion (e.g., to find the initial capsule pose or when it is stuck in an intestinal fold). The second method estimates the 6-DOF capsule pose as it synchronously rotates with the applied magnetic field using a square-root variant of the Unscented Kalman filter. A simple process model is adopted that restricts the capsule's movement to translation along and rotation about its principle axis. The capsule is actively propelled forward or backward, but it is not actively steered, rather, steering is provided by the lumen. The propulsion parameters that

transform magnetic force and torque to the capsule's spatial velocity and angular velocity are estimated with an additional square-root Unscented Kalman filter to enable the capsule to navigate heterogeneous environments such as the small intestines.

An optimized localization-propulsion system is described using the two localization algorithms and prior work in screw-type magnetic capsule propulsion with a single rotating dipole field. The capsule's regime is determined and the corresponding localization method is employed. Based on the capsule's estimated pose and the current estimates of its propulsion parameters, the actuator magnet's pose relative to the capsule is optimized to maximize the capsule's forward propulsion. Using this system, our prototype magnetic capsule successfully completed U-shaped and S-shaped trajectories in fresh bovine intestines with an average forward velocity of 5.5 mm/s and 3.5 mm/s, respectively. At this rate it would take approximately 18-30 minutes to traverse the 6 meters of a typical human small intestine.

CONTENTS

LIST OF FIGURES

LIST OF TABLES

ACKNOWLEDGEMENTS

I would like to start by thanking my advisor Dr. Jake Abbott. I could not have asked for a better mentor and without him this dissertation would not have been possible. I am also grateful to the rest of my committee (Dr. Thomas Henderson, Dr. Tucker Hermans, Dr. John Hollerbach, and Dr. Stephen Mascaro) for their guidance and help along this journey and Dr. Thomas Schmid for his help with the design and construction of the prototype capsules.

I would also like to thank my family and friends for their support throughout this endeavor, but I am especially grateful to my amazing husband, Justin. He listened to endless soliloquies about magnetics and encouraged me in times of trouble. To my fellow Telerobotics researchers, I am thankful for their entertainment and insight; without our campus walks, my sanity would no longer be intact.

Finally, I would like to thank the National Science Foundation for funding the majority of this work through a Graduate Research Fellowship, and under grants 0654414 and 0952718.

CHAPTER 1

INTRODUCTION

Diseases in the gastrointestinal tract are a major health concern (e.g., colorectal cancer is the third most common type of cancer in the United States [1]). Wireless capsule endoscopes are a promising diagnostic tool because they provide the ability to view the entire gastrointestinal tract painlessly and without anesthesia, but in their current passive form, their effectiveness is limited. Researchers have been investigating alternative methods to actively propel and localize these devices because it would transform cancer screening [2, 3]. One promising method is using magnetic fields, which has the benefit of being able to actuate [4, 5, 6, 7, 8, 9] and localize [10, 11, 12, 13, 14] the capsule using the same technology. A small permanent magnet is embedded inside the capsule, and an externally placed magnetic source is used to manipulate the device, with no additional power source needed for the capsule's propulsion.

Prior work in closed-loop control of magnetic capsules has focused on utilizing magnetic gradients for dragging or pulling [6, 15, 16], but magnetic force decreases with distance as $\|\mathbf{p}_c\|^{-4}$ whereas magnetic torque decreases as $\|\mathbf{p}_c\|^{-3}$ where $\mathbf{p}_c$ is the position vector from the actuator magnet to the capsule. In clinical applications where the ability to increase that distance would be advantageous, the use of magnetic torque is preferable. A propulsion method for capsule endoscopes was previously developed that utilizes a single rotating dipole to simultaneously employ magnetic force and torque [8]. Use of this method relied on a six-degree-of-freedom (6-DOF) robotic arm to manipulate the actuator magnet, but was subject to singularity and workspace issues. Chapter 2 describes the spherical-actuator-magnet manipulator (SAMM), which will be used as the actuator magnet in all subsequent localization and propulsion work. This device is a robotic end-effector that provides singularity-free rotation about any arbitrary axis and is almost perfectly approximated by the point-dipole model.

There are numerous ways to determine the position and orientation (collectively referred to as the pose) of wireless capsules endoscopes (see [17] for a full review), but the use of magnetic fields is preferable if used in conjunction with magnetic propulsion because little or no additional hardware is required.

There are two general methods used in magnetic tracking for capsule endoscopy. The first uses an array of externally placed sensors to localize a small permanent magnet placed inside the capsule [10, 11, 18, 19]. This option often is not compatible with magnetic actuation because the sensors are corrupted by the larger external magnet. While it is possible to subtract off the known applied field and estimate the 5-DOF pose of the capsule [20], a complete 6-DOF pose is preferable to optimize the capsule's control. Alternatively, magnetic sensors can be embedded inside the capsule and its pose estimated relative to an external magnetic source [12, 13, 21, 22]. This is the method we will employ. Prior work required large-range magnetic sensors to prevent saturation from their close proximity to the capsule's internal magnet. In Chapter 3, we design a prototype capsule embedded with Hall-effect sensors, which are strategically placed to measure the magnetic field at the center of the capsule with negligible interference from the capsule's magnet. Based on these magnetic field measurements, we wanted to estimate the 6-DOF capsule pose. Non-iterative localization algorithms using a rotating dipole field were investigated, but found too noise-sensitive for real-time use [23, 24]. Chapter 3 develops an iterative magnetic localization method to estimate the full 6-DOF pose of the capsule while it is stationary or in the step-out regime in which the magnetic field is rotated too quickly for the capsule to remain in synchronous rotation. While similar methods previously existed, [21, 24], the method we develop is more robust to sensor noise because it uses all sensor data independently and solves for the complete 6-DOF pose simultaneously. Furthermore, it explores the use of additional rotation axes to improve localization accuracy.

The method described in Chapter 3 assumes the capsule has no net motion, and as a result the capsule's propulsion and localization must be decoupled. This requirement limits the effectiveness of the previous localization algorithm because the capsule's actuation must be periodically paused to update the capsule's pose estimate. To provide continuous control, the full 6-DOF capsule pose must be estimated while it is actively propelled. In Chapter 4, we develop a localization method to estimate the capsule's pose

while it is synchronously rotating with the applied field. The combination of the two localization algorithms with previously published actuation methods [8] is then used to provide closed-loop propulsion of a magnetic capsule throughout an entire trajectory.

A complete localization-propulsion system is described in Chapter 4 which first estimates the capsule's current regime in the field (i.e., Is the capsule synchronously rotating with the field?) and then utilizes the corresponding localization method for pose feedback to the propulsion method. The optimal position and rotation speed of the external source is chosen, subject to constraints (e.g., to prevent collisions with the patient), to maximize the capsule's forward velocity. Experiments successfully completed in bovine intestines demonstrate the clinical feasibility of this localization-propulsion method.

Previously, a rotating magnetic field could only be used to localize stationary capsules, which restricted the usefulness of prior magnetic-actuation methods. This work demonstrates that magnetic fields are capable of providing closed-loop propulsion of magnetic capsule endoscopes using a single rotating magnetic dipole field. The ability to actuate and localize capsule endoscopes using a single external permanent magnet will provide a low-cost option for imaging the entire gastrointestinal tract and has the potential to radically alter screening for diseases. Although this project will exclusively use a permanent magnet for the actuator magnet, the methods are not restricted to this hardware, and can be used with any rotating dipole field including electromagnetic systems [25]. Chapter 5 discusses recommendations for future work.

1.1 References

[1] American Cancer Society, "Colorectal cancer facts & figures 2011 - 2013," Tech. Rep., Atlanta: American Cancer Society, 2011.

[2] F. Carpi, "Magnetic capsule endoscopy: The future is around the corner," *Expert Rev. Med. Devices*, vol. 7, no. 2, pp. 161–164, Mar. 2010.

[3] P. R. Slawinski, K. L. Obstein, and P. Valdastri, "Emerging issues and future developments in capsule endoscopy," *Tech Gastro Endo*, vol. 17, no. 1, pp. 40–46, Jan. 2015.

[4] A. Uehara and K. Hoshina, "Capsule endoscope NORIKA system," *Min. Invas. Ther. and Allied Technol.*, vol. 12, no. 5, pp. 227–334, Sept. 2003.

[5] X. Wang and M.Q.-H. Meng, "Computational aspects in actuation and guidance mechanism for wireless active capsule endoscope," in *IEEE Int. Conf. Intelligent Robots and Systems*, 2008, pp. 1198–1203.

[6] G. Ciuti, P. Valdastri, A. Menciassi, and P. Dario, "Robotic magnetic steering and locomotion of capsule endoscope for diagnostic and surgical endoluminal procedures," *Robotica*, vol. 28, pp. 199–207, Mar. 2010.

[7] F. Carpi, N. Kastelein, M. Talcott, and C. Pappone, "Magnetically controllable gastrointestinal steering of video capsules," *IEEE Trans. Biomed. Eng.*, vol. 58, no. 2, pp. 231–234, Feb. 2011.

[8] A. W. Mahoney and J. J. Abbott, "Generating rotating magnetic fields with a single permanent magnet for propulsion of untethered magnetic devices in a lumen," *IEEE Trans. Robotics*, vol. 30, no. 2, pp. 411–420, Apr. 2014.

[9] J. Kim, Y. Kwon, and Y. Hong, "Automated alignment of rotating magnetic field for inducing a continuous spiral motion on a capsule endoscope with a twistable thread mechanism," *Int. J. of Prec. Eng. & Manu.*, vol. 13, no. 3, pp. 371–377, Mar. 2012.

[10] S. Song *et al.*, "6-D magnetic localization and orientation method for an annular magnet based on a closed-form analytical model," *IEEE Trans. Mag.*, vol. 50, no. 9, pp. 5000411, Mar. 2014.

[11] D. M. Pham and S. M. Aziz, "A real-time localization system for an endoscopic capsule," in *IEEE Int. Conf. ISSNIP*, 2014, pp. 1–6.

[12] C. Di Natali, M. Beccani, and P. Valdastri, "Real-time pose detection for magnetic medical devices," *IEEE Trans. Mag.*, vol. 49, no. 7, pp. 3524–3527, July 2013.

[13] M. Salerno *et al.*, "A discrete-time localization method for capsule endoscopy based on on-board magnetic sensing," *Meas. Sci. Technol.*, vol. 23, no. 1, pp. 015701, Nov. 2012.

[14] K. M. Popek and J. J. Abbott, "6-D localization of magnetic capsule endoscope using a stationary rotating magnetic dipole field," in *Hamlyn Symp. Medical Robotics*, 2015, pp. 47–48.

[15] A. Z. Taddese, P. R. Slawinski, K. L. Obstein, and P. Valdastri, "Nonholonomic closed-loop velocity control of a soft-tethered magnetic capsule endoscope," in *IEEE/RSJ Int. Conf. Intelligent Robots and Systems*, 2016, pp. 1139–1144.

[16] M. Salerno, R. Rizzo, E. Sinibaldi, and A. Menciassi, "Force calculation for localized magnetic driven capsule endoscopes," in *IEEE Int. Conf. Robotics and Automation*, 2013, pp. 5354–5359.

[17] T. D. Than, G. Alici, H. Zhou, and W. Li, "A review of localization systems for robotic endoscopic capsules," *IEEE Trans. Bio. Eng.*, vol. 59, no. 9, pp. 2387–2399, Sept. 2012.

[18] C. Hu *et al.*, "A cubic 3-axis magnetic sensor array for wirelessly tracking magnet position and orientation," *IEEE Sensors J*, vol. 10, no. 5, pp. 903–913, May 2010.

[19] W. Weitschies, H. Blume, and H. Monnikes, "Magnetic marker monitoring: High resolution real-time tracking of oral solid dosage forms in the gastrointestinal tract," *European J Pharmaceutics and Biopharmaceutics*, vol. 74, no. 1, pp. 93 – 101, Jan. 2010.

[20] D. Son, S. Yim, and M. Sitti, "A 5-D localization method for a magnetically manipulated untethered robot using a 2-D array of hall-effect sensors," *Trans on Mech*, vol. 21, no. 2, pp. 708–716, Apr. 2016.

[21] M. Kim, Y. Hong, and E. Lim, "Position and orientation detection of capsule endoscopes in spiral motion," *Int. J of Prec. Eng. and Manu.*, vol. 11, no. 1, pp. 31–37, Feb. 2010.

[22] X. Guo, G. Yan, and W. He, "A novel method of three-dimensional localization based on a neural network algorithm," *J of Med Eng & Tech*, vol. 33, no. 3, pp. 192–198, Jan. 2009.

[23] E. Paperno, I. Sasada, and E. Leonovich, "A new method for magnetic position and orientation tracking," *IEEE Trans. Magn.*, vol. 37, no. 4, pp. 1938–1940, July 2001.

[24] K. M. Popek, A. W. Mahoney, and J. J. Abbott, "Localization method for a magnetic capsule endoscope propelled by a rotating magnetic dipole field," in *IEEE Int. Conf. Robotics and Automation*, 2013, pp. 5328–5333.

[25] A. J. Petruska and J. J. Abbott, "Omnimagnet: An omnidirectional electromagnet for controlled dipole-field generation," *IEEE Trans. Magnetics*, vol. 50, no. 7, pp. 8400810, July 2014.

CHAPTER 2

THE SPHERICAL-ACTUATOR-MAGNET MANIPULATOR: A PERMANENT-MAGNET ROBOTIC END-EFFECTOR

The work included in this chapter was published in *IEEE Transactions on Robotics*, and is included without modification. It details the development of the spherical-actuator-magnet manipulator (SAMM) that is accurately modeled by the point-dipole equation and can be rotated about any arbitrary axis instantaneously, eliminating singularity issues. This device is used as the external magnetic source in all subsequent work in this dissertation.

This was a collaborative work with Samuel Wright and Arthur Mahoney, under the guidance of Dr. Jake Abbott. My contributions to this work included: (1) I debugged the SAMM device to determine why the control system was not effective at speeds above 1 Hz; (2) I retrofitted the device with nonmetallic materials to reduce eddy currents; (3) I implemented a new control system, provided in Section IV, which improved position tracking and tripled the maximum rotation speed of the SAMM (the velocity is now limited by the chosen hardware); (4) I calibrated the Hall-effect sensor array used for feedback control of the dipole moment; (5) I wrote the software for experimental validation; and (6) I conducted and described the experiments in Section VIII.

The Spherical-Actuator-Magnet Manipulator: A Permanent-Magnet Robotic End-Effector

Samuel E. Wright, Arthur W. Mahoney, *Member, IEEE*, Katie M. Popek, *Member, IEEE*, and Jake J. Abbott, *Member, IEEE*

***Abstract*—A variety of magnetic devices can be manipulated remotely using a single permanent "actuator" magnet positioned in space by a robotic manipulator. This paper describes the spherical-actuator-magnet manipulator (SAMM), which is designed to replace or augment the singularity-prone spherical wrist used by prior permanent-magnet manipulation systems. The SAMM uses three omniwheels to enable holonomic control of the heading of its magnet's dipole and to enable its magnet to be rotated continuously about any axis of rotation. The SAMM performs closed-loop control of its dipole's heading using field measurements obtained from Hall-effect sensors as feedback, combined with modeled dynamics, using an extended Kalman filter. We describe the operation and construction of the SAMM, develop and characterize controllers for the SAMM's spherical magnet, and demonstrate remote actuation of an untethered magnetic device in a lumen using the SAMM.**

***Index Terms*—Magnetic dipole, magnetic manipulation, medical robotics, microrobotics, spherical mechanism.**

I. Introduction

THIS paper describes the spherical-actuator-magnet manipulator (SAMM), which is a mechatronic device housing a solid uniformly magnetized spherical permanent magnet that is intended to be used as the "actuator magnet" in a magnetic-manipulation system. The SAMM is designed to be used as an end-effector mounted to the tool frame of a robotic manipulator that is used to *position* the spherical magnetic in space (see Fig. 1). The SAMM enables holonomic singularity-free control of the *orientation* of its spherical magnet, as well as continuous rotation of its magnet about arbitrary axes of rotation. The SAMM was designed so as to remove kinematic limitations encountered in prior permanent-magnet manipulation systems. This distal surface of the SAMM is designed to be smooth and free of moving parts, so that the spherical magnet can be placed very close to the magnetic device that it is trying to actuate or manipulate.

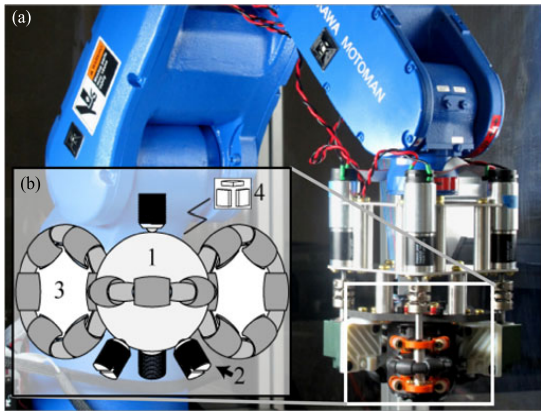

Fig. 1. (a) SAMM prototype as the end-effector of a robotic manipulator. (b) Concept diagram illustrating the spherical magnet (1), which is prevented from translating by four constraints (2) that create a rolling form-closure. Three omniwheels (3) whose axes of rotation span $\mathbb{R}^3$ contact the magnet and cause it to rotate as desired. Magnetic-field sensors (4) measure the magnet's dipole moment to be used for closed-loop control of the dipole's heading (i.e., 2-DOF orientation).

Two prior works in our lab motivated the development of the SAMM. The ability to control a screw-like untethered magnetic device (UMD) in a lumen using a single *rotating* permanent magnet as the actuation source, in a task reminiscent of active capsule endoscopy in the intestines, was described in [1]. The results of [1] enable the actuator magnet to be placed in any position relative to the UMD, provided a specific position-dependent actuator-magnet rotation axis is established. In the experimental results of [1], the actuator magnet was rotated by a single DC motor that was rigidly mounted to the tool frame of an industrial six-degree-of-freedom (6-DOF) robotic manipulator. In that setup, the rotation axis of the actuator magnet was fixed with respect to the tool frame of the robotic manipulator. Such a setup is capable of placing the actuator magnet with the

Manuscript received December 5, 2016; revised March 8, 2017; accepted April 9, 2017. This paper was recommended for publication by Associate Editor P.-C. Lin and Editor I-M. Chen upon evaluation of the reviewers' comments. This work was supported by the National Science Foundation under Grant 0952718. This paper was presented in part at the IEEE International Conference Robotics and Automation, Seattle, WA, USA, 2015. *(Corresponding author: Jake Abbott.)*

S. E. Wright was with the Department of Mechanical Engineering, University of Utah, Salt Lake City, UT 84112 USA. He is now with Sarcos Robotics, Salt Lake City, UT 84108 USA (e-mail: s.wright@sarcos.com).

A. W. Mahoney was with the School of Computing, University of Utah, Salt Lake City, UT 84112 USA. He is now with the Department of Mechanical Engineering, Vanderbilt University, Nashville, TN 37235 USA (e-mail: art.mahoney@vanderbilt.edu).

K. M. Popek was with the School of Computing and the Robotics Center, University of Utah, Salt Lake City, UT 84112 USA. She is now with The Johns Hopkins University Applied Physics Laboratory, Laurel, MD 20723 USA (e-mail: katie.popek@jhuapl.edu).

J. J. Abbott is with the Department of Mechanical Engineering and the Robotics Center, University of Utah, Salt Lake City, UT 84112 USA (e-mail: jake.abbott@utah.edu).

Color versions of one or more of the figures in this paper are available online at http://ieeexplore.ieee.org.

Digital Object Identifier 10.1109/TRO.2017.2694841

correct rotation axis to guide a UMD through relatively simple trajectories. However, when tasked with navigating a UMD through tortuous paths (e.g., the small intestines), the physical constraints of the robotic manipulator (i.e., joint limits and singularities) limit how the UMD can be actuated, and limit the workspace.

The effects of manipulator limitations on UMD actuation were also observed and were characterized in [2], where a single, *nonrotating* permanent magnet was used to levitate a semibuoyant magnetic capsule with 5-DOF (3-DOF position and 2-DOF heading) control in a task reminiscent of capsule endoscopy in the stomach. Kinematic singularities and workspace limitations were identified as the primary limiting factors to dexterous manipulation. To mitigate the effect of singularities, the authors introduced a control method that sacrificed control authority over the capsule's heading in order to maintain 3-DOF control over the capsule's position when the manipulator nears a kinematic singularity.

The SAMM has no joint limits or kinematic singularities by design. This is made possible by using three omniwheels to drive the SAMM's spherical magnet. An omniwheel is a common mechanism that incorporates small rollers that permit controlled rotation about the omniwheel's rotation axis and free rotation about the two orthogonal axes. Designing the three omniwheel rotation axes to be linearly independent enables any instantaneous magnet rotation axis to be achieved. By making the magnet's axis of rotation continuously variable, irrespective of the robotic manipulator used to position the SAMM, the kinematic singularities of the robotic manipulator can be avoided, and the robotic manipulator is free to position the actuator magnet optimally for manipulation. The SAMM will also enable robotic manipulators with less than 6-DOF to be considered for use in magnetic manipulation (e.g., a simple 3-DOF gantry system or SCARA robot). With singularity-free orientation control of its spherical magnet, the SAMM can be used to solve the problems found in both of the projects described above, and has the potential to be used for the remote actuation of a variety of magnetic devices that have been previously developed for minimally invasive medicine, including both UMDs [1], [3]–[11], and tethered magnetic devices such as catheters and cochlear-implant electrode arrays [12], [13].

There are several reasons for choosing a magnet of spherical geometry. First, being of constant radius, it is simple to maintain form-closure regardless of the magnet's orientation, enabling it to be easily incorporated into a physical device. Second, a spherical magnet makes the best use of available space in the sense that it fully fills the volume of its bounding sphere with magnetic material to maximize the strength of the magnetic dipole. Third, the field of a spherical permanent magnet is theoretically perfectly fit by the simple point-dipole model [14], [15], which enables analytic tools to be accurately applied. Finally, a spherical body has no principal directions of inertia, giving it isotropic dynamic properties, which is particularly valuable during continuous rotation.

Our SAMM design was inspired by prior "ballbot" systems, in which a robot balances itself atop a sphere (e.g., a bowling ball) [16], [17]. With ballbots, only the instantaneous angular velocity of the ball is important for control, and the ball's orientation is not measured [18] (i.e., there is no preferred "north pole" of a bowling ball). However, for remote magnetic manipulation, knowledge of the magnet's dipole heading is critical since it determines the field applied to the actuated magnetic device and how the device is controlled. Therefore, the SAMM includes a magnetic-field sensor system to estimate the spherical-magnet's dipole heading. The SAMM is fundamentally different—in terms of design, control, and end use—from spherical motors, which use electromagnetic stator coils to orient a permanent-magnet spherical rotor (see [19]).

We use the term "heading" since the dipole's magnitude is constant and known, and we are only interested in the 2-DOF pointing orientation of the dipole rather than the full 3-DOF orientation of the sphere. This is because the field generated by a spherical permanent magnet is radially symmetric about its dipole axis, so rotations about the dipole axis neither result in a change in the magnetic field to the remote device being actuated nor to the sensors measuring the field.

In this paper, we expand the results of [20] in the following ways.

1) A Kalman filter is presented that estimates the spherical magnet's dipole heading and angular velocity by synthesizing sensor feedback and modeled dynamics.
2) We describe our mechanical approach to keep the omniwheels in contact with the spherical magnet despite nonidealities.
3) We present a new "pointing mode" controller that solely controls the spherical magnet's dipole heading.
4) We present an improved version of the "rotating mode" controller.
5) We describe how to calibrate the magnetic-field sensors used to measure the spherical magnet's heading, which substantially improves the accuracy of the estimation of the spherical magnet's dipole heading.
6) We present two additional experiments that assess the performance of the controllers we present herein.

II. Velocity Kinematics and Inverse Kinematics

We follow a convention where scalars are denoted by lower case standard font (e.g., c), vectors by lower case bold font (e.g., $\mathbf{x}$), and matrices by capital bold font (e.g., $\mathbf{M}$). The "hat" symbol denotes a unit-length vector (e.g., $\hat{\mathbf{x}}$).

For some desired angular velocity $\boldsymbol{\omega}_\mathbf{m} \in \mathbb{R}^3$ of the spherical magnet, the necessary omniwheel rotation speeds must be determined. Let the unit-length vectors $\hat{\mathbf{d}}_1$, $\hat{\mathbf{d}}_2$, and $\hat{\mathbf{d}}_3$ point from the magnet's center to the contact points where the three omniwheels touch the magnet (see Fig. 2). We assume that the omniwheel axes $\hat{\mathbf{a}}_1$, $\hat{\mathbf{a}}_2$, and $\hat{\mathbf{a}}_3$ are perpendicular to $\hat{\mathbf{d}}_1$, $\hat{\mathbf{d}}_2$, and $\hat{\mathbf{d}}_3$, respectively, and assume that there is no slip between the omniwheels and the magnet. Given a magnet angular velocity $\boldsymbol{\omega}_\mathbf{m}$, the surface velocity of the magnet at the ith omniwheel–magnet contact point is given as

$$\mathbf{u}_i = r_m \boldsymbol{\omega}_\mathbf{m} \times \hat{\mathbf{d}}_i \tag{1}$$

where r_m is the radius of the magnet.

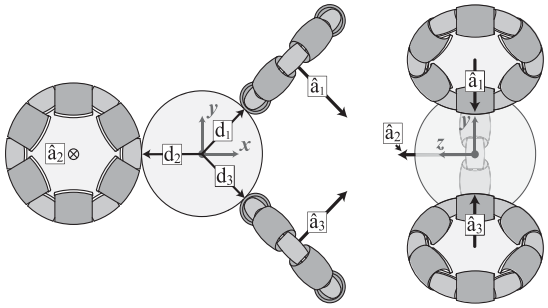

Fig. 2. Two orthogonal views of the SAMM's omniwheel configuration are shown. The vectors $\hat{\mathbf{a}}_1$, $\hat{\mathbf{a}}_2$, and $\hat{\mathbf{a}}_3$ are the omniwheel rotation axes, and $\hat{\mathbf{d}}_1$, $\hat{\mathbf{d}}_2$, and $\hat{\mathbf{d}}_3$ point from the magnet center to the corresponding omniwheel contact point. The depicted coordinate system is used throughout this paper.

The components of $\mathbf{u}_1$, $\mathbf{u}_2$, and $\mathbf{u}_3$ parallel to the respective omniwheel axes are transferred directly into rotation of the omniwheel rollers, and cause no rotation of the omniwheels themselves. All other components of $\mathbf{u}_1$, $\mathbf{u}_2$, and $\mathbf{u}_3$ cause each omniwheel to rotate with scalar rotation speeds $\omega_{\mathrm{a}1}$, $\omega_{\mathrm{a}2}$, and $\omega_{\mathrm{a}3}$, respectively. The component direction of $\mathbf{u}_i$ that causes the ith omniwheel to rotate about its axis is given as

$$\hat{\mathbf{q}}_i = \hat{\mathbf{d}}_i \times \hat{\mathbf{a}}_i. \tag{2}$$

Under the assumption of no-slip, the projection of $\mathbf{u}_1$, $\mathbf{u}_2$, and $\mathbf{u}_3$ onto the directions $\hat{\mathbf{q}}_1$, $\hat{\mathbf{q}}_2$, and $\hat{\mathbf{q}}_3$, respectively, must be mapped to the scalar rotation speeds of each omniwheel by the reciprocal of the omniwheels' radii (denoted by r_w, as we assume identical omniwheels) as

$$\omega_{\mathrm{a}i} = \frac{1}{r_w}\hat{\mathbf{q}}_i^{\mathsf{T}}\mathbf{u}_i = \frac{r_m}{r_w}\hat{\mathbf{a}}_i^{\mathsf{T}}\{\hat{\mathbf{d}}_i\}^2\boldsymbol{\omega}_{\mathrm{m}} \tag{3}$$

where $\{\hat{\mathbf{d}}_\mathbf{i}\} \in \mathrm{so}(3)$ is the skew-symmetric matrix form of the cross-product operation.

All three omniwheel rotation speeds can be packed into the vector $\boldsymbol{\omega}_\mathbf{a}$ and related to the spherical magnet angular velocity $\boldsymbol{\omega}_\mathbf{m}$, in matrix form, as

$$\boldsymbol{\omega}_\mathbf{a} = \begin{bmatrix}\omega_{\mathrm{a}1}\\ \omega_{\mathrm{a}2}\\ \omega_{\mathrm{a}3}\end{bmatrix} = \frac{r_m}{r_w}\begin{bmatrix}\hat{\mathbf{a}}_1^{\mathsf{T}}\{\hat{\mathbf{d}}_1\}^2\\ \hat{\mathbf{a}}_2^{\mathsf{T}}\{\hat{\mathbf{d}}_2\}^2\\ \hat{\mathbf{a}}_3^{\mathsf{T}}\{\hat{\mathbf{d}}_3\}^2\end{bmatrix}\boldsymbol{\omega}_\mathbf{m}. \tag{4}$$

Due to the assumption that $\hat{\mathbf{a}}_i$ is perpendicular to $\hat{\mathbf{d}}_\mathbf{i}$, (4) can be simplified to

$$\boldsymbol{\omega}_\mathbf{a} = -\frac{r_m}{r_w}\begin{bmatrix}\hat{\mathbf{a}}_1^{\mathsf{T}}\\ \hat{\mathbf{a}}_2^{\mathsf{T}}\\ \hat{\mathbf{a}}_3^{\mathsf{T}}\end{bmatrix}\boldsymbol{\omega}_\mathbf{m} = \eta\mathbf{A}^{\mathsf{T}}\boldsymbol{\omega}_\mathbf{m} \tag{5}$$

where $\eta = -r_m/r_w$ is the gear ratio from the omniwheels to the sphere (with the negative sign indicating the change in rotation direction from the omniwheels to the magnet), and $\mathbf{A} = \begin{bmatrix}\hat{\mathbf{a}}_1 & \hat{\mathbf{a}}_2 & \hat{\mathbf{a}}_3\end{bmatrix}$.

The omniwheel axes and positioning must be designed such that matrix $\mathbf{A}$ has full rank, otherwise there will exist a direction of $\boldsymbol{\omega}_\mathbf{m}$ that cannot be achieved with any selection of omniwheel rotation speeds. Although linear independence of the columns of $\mathbf{A}$ is a sufficient condition mathematically, in practice the columns should be designed to be as close to mutually orthogonal as possible. Otherwise, some desired $\boldsymbol{\omega}_\mathbf{m}$ will require an unnecessarily, and possibly unachievably, fast omniwheel rotation speed. We designed our system so that $\hat{\mathbf{a}}_1$, $\hat{\mathbf{a}}_2$, and $\hat{\mathbf{a}}_3$ are mutually orthogonal and arranged as shown in Fig. 2. This counter-opposed configuration results in the omniwheel axes: $\hat{\mathbf{a}}_1 = [\sqrt{2}/2\ \sqrt{2}/2\ 0]^{\mathsf{T}}$, $\hat{\mathbf{a}}_2 = [0\,0\,(-1)]^{\mathsf{T}}$, and $\hat{\mathbf{a}}_3 = [\sqrt{2}/2\,(-\sqrt{2}/2)\ 0]^{\mathsf{T}}$. Other feasible omniwheel arrangements are possible [21].

III. System Dynamics

The net applied torque $\boldsymbol{\tau}_\mathbf{m}$ on the actuator magnet is related to the magnet's instantaneous angular velocity $\boldsymbol{\omega}_\mathbf{m}$ and angular acceleration $\dot{\boldsymbol{\omega}}_\mathbf{m}$ by

$$\boldsymbol{\tau}_\mathbf{m} = \mathbf{J}\dot{\boldsymbol{\omega}}_\mathbf{m} + \mathbf{B}(\boldsymbol{\omega}_\mathbf{m})\boldsymbol{\omega}_\mathbf{m} + \mathbf{c}(\boldsymbol{\omega}_\mathbf{m}, \boldsymbol{\tau}_\mathbf{m}) \tag{6}$$

where the manipulator's rotational inertia matrix is denoted by $\mathbf{J} \in \mathbb{R}^{\mathbf{3\times3}}$, the viscous friction matrix is denoted by $\mathbf{B}(\boldsymbol{\omega}_\mathbf{m}) \in \mathbb{R}^{\mathbf{3\times3}}$, and the Coulomb friction is denoted by $\mathbf{c}(\boldsymbol{\omega}_\mathbf{m}, \boldsymbol{\tau}_\mathbf{m}) \in \mathbb{R}^{\mathbf{3}}$.

The rotational inertia matrix $\mathbf{J}$ is the combination of the inertia due to the spherical magnet $\mathbf{J}_\mathbf{m}$ and the inertia due to the motors and omniwheels $\mathbf{J}_\mathbf{w}$:

$$\mathbf{J} = \mathbf{J}_\mathbf{m} + \eta^2\mathbf{J}_\mathbf{w} = \frac{2}{5}m_m r_m^2\,\mathbf{I_3} + \eta^2\left(\frac{1}{2}m_w r_w^2 + j_{\mathrm{mot}}\right)\mathbf{I_3} \tag{7}$$

where the gear ratio η is defined in Section II, m_m is the mass of the spherical magnet, and r_m is its radius. The rotational inertia of each omniwheel includes the omniwheel's inertia (approximated as a rotating disk with radius r_w and mass m_w) and the corresponding driving motor's inertia j_{mot} (this term includes the motor's rotor inertia reflected through any gearing in the motor, as seen at the output shaft). Matrix $\mathbf{I_3} \in \mathbb{R}^{3\times3}$ is the identity matrix.

We have observed viscous and Coulomb friction effects [22] that are asymmetric. The viscous friction matrix $\mathbf{B}(\boldsymbol{\omega}_\mathbf{m})$ is modeled as $\mathbf{B} = \mathrm{diag}(B_1, B_2, B_3)$, where the coefficients B_i are determined according to the sign of the corresponding terms of $\boldsymbol{\omega}_\mathbf{m}$:

$$B_i = \begin{cases} B_i^+ : \omega_{\mathrm{m},i} > 0 \\ B_i^- : \omega_{\mathrm{m},i} < 0. \end{cases} \tag{8}$$

The Coulomb friction term $\mathbf{c}(\boldsymbol{\omega}_\mathbf{m}, \boldsymbol{\tau}_\mathbf{m})$, which models static friction, is defined as

$$c_i = \begin{cases} \tau_i : \omega_{\mathrm{m},i} = 0 \text{ and } c_i^- \le \tau_{\mathrm{m},i} \le c_i^+ \\ c_i^+ : \omega_{\mathrm{m},i} = 0 \text{ and } \tau_{\mathrm{m},i} > c_i^+ \\ c_i^- : \omega_{\mathrm{m},i} = 0 \text{ and } \tau_{\mathrm{m},i} < c_i^- \\ c_i^+ : \omega_{\mathrm{m},i} > 0 \\ c_i^- : \omega_{\mathrm{m},i} < 0. \end{cases} \tag{9}$$

Note that similarly to how magnet angular velocity $\boldsymbol{\omega}_\mathbf{m}$ is mapped to motor angular velocity $\boldsymbol{\omega}_\mathbf{a}$ via (5), the magnet torque $\boldsymbol{\tau}_\mathbf{m}$ is mapped to motor torque $\boldsymbol{\tau}_\mathbf{a}$ through $\mathbf{A}^{\mathsf{T}}$, but with the

inverse of the gear ratio:

$$\boldsymbol{\tau}_{\mathbf{a}} = \frac{1}{\eta}\mathbf{A}^{\mathsf{T}}\boldsymbol{\tau}_{\mathbf{m}}. \tag{10}$$

IV. Sensing the Magnet's Dipole Moment

The dipole moment of the magnetic body (denoted by the vector $\mathbf{m}$) is the vector from the south to north poles of the magnet. Methods of magnetic manipulation using a single permanent magnet require the magnet's dipole moment to be specifically directed and thus known. The dipole moment $\mathbf{m}$ of the SAMM's magnet can be determined by measuring the magnetic field $\mathbf{h}$ that it generates in space.

One approach to measuring the magnetic field uses Hall-effect sensors, which measure the component of the field in the direction normal to (i.e., passing through) the sensor's face. We assume the general case of n Hall-effect sensors. Let each sensor be positioned in space such that the vectors $\mathbf{p}_1$ through $\mathbf{p}_n$, in units of meters, measure each sensor's position relative to the spherical magnet's center, and let $\hat{\mathbf{v}}_1$ through $\hat{\mathbf{v}}_n$ be unit-magnitude vectors that describe the directions that are sensed by each sensor; all vectors are expressed in the same frame as $\mathbf{m}$. Let the magnetic field at each sensor position be denoted by $\mathbf{h}_1$ through $\mathbf{h}_n$, in units $\mathrm{A}\cdot\mathrm{m}^{-1}$. The measured component of the field produced by the ith sensor is denoted with the scalar s_i and is given by

$$s_i = \hat{\mathbf{v}}_i^{\mathsf{T}}\mathbf{h}_i. \tag{11}$$

The magnetic field $\mathbf{h}_i$, at each sensor position $\mathbf{p}_i$, can be predicted with the point-dipole model

$$\mathbf{h}_i = \frac{1}{4\pi\,\|\mathbf{p}_i\|^3}\left(3\hat{\mathbf{p}}_i\hat{\mathbf{p}}_i^{\mathsf{T}} - \mathbf{I_3}\right)\mathbf{m} = \mathbf{H}_i\mathbf{m} \tag{12}$$

which exactly predicts the field produced by a spherical permanent magnet [14], [15]. For all other geometries, it is an approximation that becomes more accurate with increasing distance [23].

Substituting (12) into (11) produces an expression relating the magnet's dipole moment $\mathbf{m}$ to each of the n sensor measurements, which can be aggregated into the following matrix equation:

$$\mathbf{s} = \begin{bmatrix} s_1 \\ \vdots \\ s_n \end{bmatrix} = \begin{bmatrix} \hat{\mathbf{v}}_1^{\mathsf{T}}\mathbf{H}_1 \\ \vdots \\ \hat{\mathbf{v}}_n^{\mathsf{T}}\mathbf{H}_n \end{bmatrix}\mathbf{m} = \mathbf{S}\mathbf{m}. \tag{13}$$

The $n \times 3$ constant matrix $\mathbf{S}$ encapsulates the complete geometric description of the sensor arrangement, as it pertains to estimating $\mathbf{m}$. If the matrix $\mathbf{S}$ has full column rank, then a solution for the dipole moment $\mathbf{m}$ can be found as

$$\mathbf{m} = \mathbf{S}^{\dagger}\mathbf{s} \tag{14}$$

where $\mathbf{S}^{\dagger} = \mathbf{V}\boldsymbol{\Sigma}^{\dagger}\mathbf{U}^{\mathsf{T}}$ is the Moore–Penrose pseudoinverse of $\mathbf{S}$, using the singular-value decomposition $\mathbf{S} = \mathbf{U}\boldsymbol{\Sigma}\mathbf{V}^{\mathsf{T}}$, where the columns of $\mathbf{U}$ and $\mathbf{V}$ are the output and input singular vectors of $\mathbf{S}$, respectively, $\boldsymbol{\Sigma}$ contains the singular values of $\mathbf{S}$ on the main diagonal and zeros elsewhere, and $\boldsymbol{\Sigma}^{\dagger}$ is the transpose of $\boldsymbol{\Sigma}$ in which the nonzero singular values have been replaced by their reciprocals [24]. The matrix $\mathbf{S}$ should be made to have full column rank by using at least three Hall-effect sensors and appropriately selecting the positions ($\mathbf{p}_i$) and directions ($\hat{\mathbf{v}}_i$) of each sensor. When $n > 3$, (14) provides the best estimate of $\mathbf{m}$ in a least-squares sense. Along with making $\mathbf{S}$ full rank, the sensors should also be ideally arranged to minimize the variance of the measured dipole moment by decreasing the singular values of $\mathbf{S}$. Note that the constant matrix $\mathbf{S}^{\dagger}$ can be calculated offline.

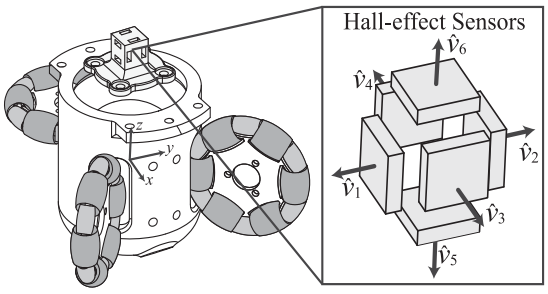

Fig. 3. Sensor cluster comprising six Hall-effect sensors, mounted directly above the housing, with coordinate system and numbering convention shown.

For our system, we designed a sensor cluster comprising six 1-DOF Allegro A1302 Hall-effect sensors that are arranged on the surface of a cube and positioned in close proximity to each other. The sensor cluster is mounted to the SAMM, as shown in Fig. 3. In addition to being a space free from moving parts, this location ensures that magnetic-field disturbances in the workspace below the SAMM (e.g., from the magnet of a device being manipulated by the SAMM) have a minimal impact on the estimation of the SAMM magnet's dipole heading. The sensors, which have a sensitivity of 13 mV/mT, utilize their full output-voltage range without saturation. We describe the poses of the sensors quantitatively in Section VIII. Other sensor arrangements are considered in [21].

V. State Estimation

Although (14) provides an instantaneous measurement of the magnet's dipole, filtering incorporates knowledge of the manipulator's dynamics to reduce the effects of sensor noise. We have chosen to implement the hybrid extended Kalman filter (EKF) [25], which linearizes the system's nonlinear dynamic and observation equations about the current predicted state before employing the Kalman filter algorithm, and which uses continuous-time equations to model the system's dynamics but performs system observation in discrete time.

A. Review of the Hybrid EKF

We briefly review the hybrid EKF as described in [25] for completeness. The hybrid implementation (otherwise known as the discrete-time implementation) of the EKF allows for the state $\mathbf{x}(t)$ and state estimate covariance to transition continuously according to the models

$$\dot{\mathbf{x}}(t) = \mathbf{f}\big(\mathbf{x}(t), \mathbf{u}(t)\big) + \mathbf{w}(t) \tag{15}$$

$$\dot{\mathbf{P}}(t) = \mathbf{F}(t)\mathbf{P}(t) + \mathbf{P}(t)\mathbf{F}(t)^{\mathsf{T}} + \mathbf{Q} \tag{16}$$

respectively, where $\mathbf{f}\big(\mathbf{x}(t), \mathbf{u}(t)\big)$ models the system's dynamics given the input $\mathbf{u}(t)$ and process noise $\mathbf{w}(t) \sim \mathcal{N}(0, \mathbf{Q})$, and the linearization matrix $\mathbf{F}(t)$ is given as

$$\mathbf{F}(t) = \left.\frac{\partial \mathbf{f}}{\partial \mathbf{x}}\right|_{\bar{\mathbf{x}}(t), \mathbf{u}(t)}. \tag{17}$$

Discrete measurements at the jth time step are modeled as

$$\mathbf{z}_j = \mathbf{g}(\mathbf{x}_j) + \mathbf{v}_j \tag{18}$$

where $\mathbf{x}_j = \mathbf{x}(t_j)$ and $\mathbf{v}_j \sim \mathcal{N}(0, \mathbf{R})$ is zero-mean measurement noise that is uncorrelated in time.

1) Predict: An *a priori* state estimate $\mathbf{x}_{j|j-1}$ and covariance $\mathbf{p}_{j|j-1}$ can be recursively predicted from the *a posteriori* estimate at the previous time step t_{j-1} by integrating (15) and (16) using a zero-order hold on the system inputs $\mathbf{u}(t)$:

$$\mathbf{x}_{j|j-1} = \mathbf{x}_{j-1|j-1} + \int_{t_{j-1}}^{t_j} \mathbf{f}(\mathbf{x}(t), \mathbf{u}(t_{j-1}))dt \tag{19}$$

$$\mathbf{P}_{j|j-1} = \mathbf{P}_{j-1|j-1} + \int_{t_{j-1}}^{t_j} \dot{\mathbf{P}}(t)dt. \tag{20}$$

2) Update: The *a priori* estimate is updated to become the *a posteriori* estimate by performing a Kalman update with sensor observations. The Kalman gain $\mathbf{K}_j$ is computed using the *a priori* covariance, the linearization of the observation model $\mathbf{g}$, and the covariance of observation noise $\mathbf{R}$ as

$$\mathbf{K}_j = \mathbf{P}_{j|j-1}\mathbf{G}_j^{\mathsf{T}}(\mathbf{G}_j\mathbf{P}_{j|j-1}\mathbf{G}_j^T + \mathbf{R})^{-1} \tag{21}$$

where $\mathbf{G}_j$ is given as

$$\mathbf{G}_j = \left.\frac{\partial \mathbf{g}}{\partial \mathbf{x}}\right|_{\bar{\mathbf{x}}_{j|j-1}}. \tag{22}$$

The Kalman update is calculated by comparing the actual sensor observation $\mathbf{z}$ with the predicted observation $\mathbf{g}(\mathbf{x}_{j|j-1})$:

$$\mathbf{x}_{j|j} = \mathbf{x}_{j|j-1} + \mathbf{K}_j\big(\mathbf{z}_j - \mathbf{g}(\mathbf{x}_{j|j-1})\big) \tag{23}$$

$$\mathbf{P}_{j|j} = \big(\mathbf{I} - \mathbf{K}_j\mathbf{G}_j\big)\mathbf{P}_{j|j-1}. \tag{24}$$

B. Implementing the Hybrid EKF

The SAMM state is represented as the vector

$$\mathbf{x} = \begin{bmatrix} \hat{\mathbf{m}} \\ \boldsymbol{\omega}_{\mathbf{m}} \end{bmatrix} \in \mathbb{S}^2 \times \mathbb{R}^3 \tag{25}$$

packed with the unit-length dipole moment heading $\hat{\mathbf{m}} \in \mathbb{S}^2$ and the magnet's angular velocity $\boldsymbol{\omega}_{\mathbf{m}} \in \mathbb{R}^3$.

The continuous-time evolution of the SAMM state and covariances are given by (15) and (16), where $\mathbf{f}(\mathbf{x}, \mathbf{u})$ is

$$\mathbf{f}(\mathbf{x}, \mathbf{u}) = \begin{bmatrix} \boldsymbol{\omega}_{\mathbf{m}} \times \hat{\mathbf{m}} \\ \mathbf{J}^{-1}\big(\boldsymbol{\tau}_{\mathbf{m}} - \mathbf{B}(\boldsymbol{\omega}_{\mathbf{m}})\boldsymbol{\omega}_{\mathbf{m}} - \mathbf{c}\left(\boldsymbol{\omega}_{\mathbf{m}}, \boldsymbol{\tau}_{\mathbf{m}}\right)\big) \end{bmatrix} \tag{26}$$

where $\mathbf{u} = \boldsymbol{\tau}_{\mathbf{m}}$ is the system input, and $\mathbf{F}$ is calculated as

$$\mathbf{F} = \frac{\partial \mathbf{f}}{\partial \mathbf{x}} = \begin{bmatrix} \{\boldsymbol{\omega}_{\mathbf{m}}\} & -\{\hat{\mathbf{m}}\} \\ \mathbf{0} & -\mathbf{J}^{-1}\mathbf{B}(\boldsymbol{\omega}_{\mathbf{m}}) \end{bmatrix}. \tag{27}$$

Note that the Coulumb friction term $\mathbf{c}(\boldsymbol{\omega}_{\mathbf{m}}, \boldsymbol{\tau}_{\mathbf{m}})$ does not vary with $\hat{\mathbf{m}}$ or $\boldsymbol{\omega}_{\mathbf{m}}$ when $\boldsymbol{\omega}_{\mathbf{m}} \neq \mathbf{0}$, additionally both $\mathbf{B}(\boldsymbol{\omega}_{\mathbf{m}})$ and $\mathbf{c}(\boldsymbol{\omega}_{\mathbf{m}}, \boldsymbol{\tau}_{\mathbf{m}})$ are not differentiable when $\boldsymbol{\omega}_{\mathbf{m}} = \mathbf{0}$ but we neglect this issue for simplicity since $\boldsymbol{\omega}_{\mathbf{m}}$ is rarely $\mathbf{0}$.

Observations are performed in discrete-time using the Hall-sensor system described in Section IV, which estimates the dipole moment $\mathbf{m}$, and using measurements of the magnet's angular velocity obtained by differentiating the motor encoder position and using (5). The observation model is structured as

$$\mathbf{z} = \mathbf{g}(\mathbf{x}) = \begin{bmatrix} \mathbf{S}\,\|\mathbf{m}\| & \mathbf{0} \\ \mathbf{0} & \mathbf{I_3} \end{bmatrix}\mathbf{x} \tag{28}$$

where $\mathbf{S}$ is the Hall-sensor matrix defined in (13). The observation model $\mathbf{g}(\mathbf{x})$ is then linearized as

$$\mathbf{G} = \frac{\partial \mathbf{g}}{\partial \mathbf{x}} = \begin{bmatrix} \mathbf{S}\,\|\mathbf{m}\| & \mathbf{0} \\ \mathbf{0} & \mathbf{I_3} \end{bmatrix}. \tag{29}$$

VI. Control

The SAMM has two modes of operation: *pointing* and *rotating*. Examples of where the pointing mode would be useful include any tasks requiring quasistatic magnetic fields, such as the actuation of an endoscopic capsule in the stomach [2], a magnet-tipped catheter [12], or a magnet-tipped cochlear-implant electrode array [13]. Examples of where the rotating mode would be useful include any task where a rotating magnetic field is fundamental to the actuation strategy, such as rolling UMDs along a surface [6]–[8], swimming through a fluid or crawling through a lumen via helical propulsion [9], [10], [26]–[28], or screwing through soft tissue [11].

Subsequent to [20] and [21], additional testing revealed that the original rotating-mode controller was not stable for all rotation axes at speeds greater than 1 Hz. The improved controller presented here provides stable rotation for all axes and speeds tested (up to 3 Hz); this maximum is due to hardware limitations. In this updated implementation, custom pointing-mode and rotating-mode controllers output a necessary magnet angular velocity $\boldsymbol{\sigma}$, which is mapped to the motor-space by the transmission matrix $\mathbf{A}$. The desired motor velocity of each omniwheel is input to its corresponding Maxon motor controller (ESCON 36/2), which provides onboard closed-loop velocity control and is tuned specifically for its wheel. We found a simple proportional controller was sufficient for both our pointing- and rotating-mode controllers because of the closed-loop velocity control.

A. Pointing-Mode Controller

The pointing-mode controller governs the *heading* of the actuator-magnet dipole moment $\hat{\mathbf{m}}$ to align along a desired heading $\hat{\mathbf{m}}_{\mathbf{des}} \in \mathbb{S}^2$. A proportional heading-control scheme is employed using the Kalman filter's estimate of the dipole moment $\hat{\hat{\mathbf{m}}}$. In order to drive $\hat{\hat{\mathbf{m}}}$ toward $\hat{\mathbf{m}}_{\mathbf{des}}$, the heading's restoration error vector $\mathbf{e}$ is computed as

$$\mathbf{e} = \theta\hat{\mathbf{n}} \tag{30}$$

where θ is the angle between $\hat{\hat{\mathbf{m}}}$ and $\hat{\mathbf{m}}_{\mathbf{des}}$, and the vector $\hat{\mathbf{n}}$ lies in the direction of $\hat{\hat{\mathbf{m}}} \times \hat{\mathbf{m}}_{\mathbf{des}}$. The angular velocity $\boldsymbol{\sigma}$

commanded to the individual motors' velocity controllers is computed as

$$\boldsymbol{\sigma} = k_p \mathbf{e} \tag{31}$$

where k_p is the proportional gain.

B. Rotating-Mode Controller

The purpose of the rotating-mode controller is to generate continuous rotation of the actuator-magnet dipole with some desired angular velocity $\boldsymbol{\omega}_{\mathbf{m},\mathbf{des}}$, with the dipole orthogonal to $\boldsymbol{\omega}_{\mathbf{m},\mathbf{des}}$, without any concern for the phase of the dipole within the cycle. Similar to the previous rotating-mode controller [20], [21], the updated version simultaneously employs two control laws: a feedforward angular-velocity subcontroller that rotates $\hat{\mathbf{m}}$ about a desired angular velocity vector $\boldsymbol{\omega}_{\mathbf{m},\mathbf{des}}$, and a proportional heading subcontroller to drive $\hat{\mathbf{m}}$ to the plane *orthogonal* to $\boldsymbol{\omega}_{\mathbf{m},\mathbf{des}}$ with control effort given by $\boldsymbol{\sigma}_\perp$. The two control laws are combined to form the total output angular velocity

$$\boldsymbol{\sigma} = \boldsymbol{\omega}_{\mathbf{m},\mathbf{des}} + \boldsymbol{\sigma}_\perp \tag{32}$$

which is sent to the motors' velocity controllers. Note that the terms $\boldsymbol{\omega}_{\mathbf{m},\mathbf{des}}$ and $\boldsymbol{\sigma}_\perp$ are always orthogonal to each other and hence they do not fight each other in the control effort.

Control effort in the direction orthogonal to $\boldsymbol{\omega}_{\mathbf{m},\mathbf{des}}$ is computed as

$$\boldsymbol{\sigma}_\perp = k_{p\perp} \mathbf{e}_\perp. \tag{33}$$

The rotation-plane restoration vector $\mathbf{e}_\perp$ used to drive $\hat{\mathbf{m}}$ to the desired rotation plane is found as

$$\mathbf{e}_\perp = \hat{\mathbf{m}} \times \widehat{\boldsymbol{\Pi}\hat{\mathbf{m}}} \tag{34}$$

where

$$\boldsymbol{\Pi} = \left(\mathbf{I_3} - \hat{\boldsymbol{\omega}}_{\mathbf{m},\mathbf{des}} \hat{\boldsymbol{\omega}}_{\mathbf{m},\mathbf{des}}{}^{\mathsf{T}}\right) \tag{35}$$

$\boldsymbol{\Pi}$ is a projection operator onto the plane defined by the normal vector $\boldsymbol{\omega}_{\mathbf{m},\mathbf{des}}$, and the rightmost term in the cross product in (34) represents the normalized projection of $\hat{\mathbf{m}}$ onto the desired plane. $\mathbf{e}_\perp$ was chosen to connote "error"; it does approximate the true angular error at small angles, but will have a magnitude that is smaller than the angular error (i.e., sinusoidal in angular error) at larger values, preventing large misalignments from resulting in abrupt accelerations and undesirable slipping between the omniwheels and the spherical magnet. Unlike in the pointing mode, the cross product can be used in place of error because the deviation of $\hat{\mathbf{m}}$ from the desired rotation plane is at most 90°, so the magnitude of $\mathbf{e}_\perp$ is guaranteed to be monotonic with angular error. Equation (34) breaks down when $\hat{\mathbf{m}}$ is parallel to $\hat{\boldsymbol{\omega}}_{\mathbf{m},\mathbf{des}}$. In this case, the error between $\hat{\mathbf{m}}$ and the desired rotation plane is 90°, and any direction of motion will decrease the error from the plane equally well, so we calculate the restoration vector as $\mathbf{e}_\perp = \hat{\mathbf{m}} \times \widehat{\boldsymbol{\Pi}\boldsymbol{\xi}}$, where $\boldsymbol{\xi}$ is an arbitrary vector not parallel to $\hat{\mathbf{m}}$ (in our implementation of the controller it is randomly generated).

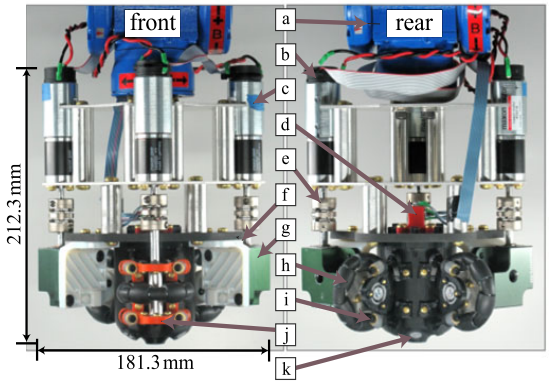

Fig. 4. Prototype SAMM shown mounted to the tool frame (a) of robotic manipulator. Encoders (b) measure the gearmotors' (c) position. The cluster of Hall-effect sensors (d) measures the spherical magnet's dipole. Power is transmitted through aluminum helical shaft couplings (e) to omniwheel axles or 90° gearboxes (g), which pivot for omniwheel compliance (f). Omniwheels (h) are tensioned to the spherical magnet through adjustable spring-tensioned pillow blocks (i), whose tension can be manually tuned through adjustment screws (j). Adjustable ball-roller-tip set-screws (k) create rolling form-closure for the spherical magnet.

VII. Prototype Implementation

Our prototype SAMM is shown in Fig. 4. The magnetic body is a 50.8-mm-diameter, Grade-N42, spherical permanent magnet with a dipole strength of 66.0 A·m^2. The field produced by the spherical magnet, which is accurately modeled by the point-dipole model (12), is strong in close proximity. During the design process, we eliminated soft-magnetic components (e.g., steel, iron, etc.) from the SAMM where possible, since soft-magnetic material near the magnet becomes magnetized under applied fields and would then exert an undesirable magnetic torque and force on the spherical magnet. For example, we chose to use plastic screws (instead of steel) to hold the SAMM mechanism together. Where it was not possible to eliminate soft-magnetic material (e.g., the gearmotors), we designed the SAMM mechanism in a way that placed soft-magnetic material as far from the spherical magnet as possible, where the fields are weakest and the soft-magnetic material would be magnetized the least.

Additionally, time-varying magnetic fields (caused by rotating the magnet) induce eddy currents in nearby electrically conductive material; these circulating currents create their own magnetic field, resulting in drag on the magnet. When possible, we used nonconductive material for components that are close to the spherical magnet (where the fields are largest and eddy currents would be highest). For example, the magnet enclosure is milled out of black Nylon and the ball-roller-tip set-screws that touch the magnet are made out of polyacetal and ceramic.

The form-closure constraints [see Figs. 1(b) and 4(k)] that allow only rotation of the spherical magnet are implemented with a set of four ball-roller-tipped precision set-screws. The smallest number of such constraints needed to guarantee form-closure is four, with three constraints whose contact points on

the magnet do not form a hemispherical great circle on the actuator magnet and a fourth constraint contacting normal to the plane established by the first three. Housed inside the tip of the set-screw is a freely rotating 5.56-mm ball that is supported by 1.50-mm subrollers. The set-screws are threaded into the housing of the mechanism so that they constrain the magnet in its desired position with minimal perceptible play when installed flush with reference bosses on the exterior of the housing. The body of the set-screws are polyacetal Misumi set-screws (BCS-BJJ) with the ball-tips and subrollers replaced with ceramic parts, making each set-screw nonmagnetic and nonconductive.

The housing of the device resembles a cylindrical structure with a hemisphere at one end where three of the four form-closure constraints are mounted. The housing is constructed out of nonconductive ABS plastic to mitigate eddy currents. The omniwheels contact the magnet through windows in the cylindrical body. The omniwheels are arranged in a counter-opposed configuration, which results in the normal forces from each omniwheel being supported by the other omniwheels, which mutually increases their traction, unlike other potential configurations where the normal forces are supported by the form-closure constraints resulting in higher rotating friction.

The custom omniwheels [see Fig. 4(h)] are based on designs described in [29] and [16], and provide nearly continuous contact with the magnet. Each omniwheel roller contains dual ceramic ball bearings for minimal friction under load, as well as a soft neoprene heat-shrink sleeve on the surface for increased traction. It is important to maximize traction to maximize achievable acceleration and bandwidth. The omniwheels are constructed with fully nonmagnetic components. Some components are conductive, but their volume is small and effects from eddy currents are not noticeable. When fully assembled, the major diameter of each omniwheel is 58.2 mm.

The omniwheels are driven by three Maxon RE-max 29 gearmotors [see Fig. 4(c)], which have a 24:1 gear ratio and 512 CPT encoders [see Fig. 4(b)], mounted with their shafts in parallel. The torques applied to omniwheel axes $\hat{\mathbf{a}}_1$ and $\hat{\mathbf{a}}_3$ are redirected via 90° gearboxes [see Fig. 4(g)]; the torque applied to omniwheel axis $\hat{\mathbf{a}}_2$ is transmitted without an additional gearbox. The 90° gearboxes comprise nylon gears mounted to aluminum shafts and are supported by dual acetal ball bearings inside an aluminum case, making the 90° gearboxes entirely nonmagnetic. The gearmotors are connected to the respective drive shafts by aluminum helical couplings [see Fig. 4(e)].

Due to irregularities that exist in the omniwheels' circularity caused by gaps between omniwheel rollers and unintentional eccentricity in the mechanical mounting, we found in our prototype development that it was beneficial to include mechanical compliance to maintain robust contact between the omniwheels and the magnet. The compliance should compensate for irregularities without altering the torque transmission matrix $\mathbf{A}$, keeping $\hat{\mathbf{a}}_i$ constant and perpendicular to $\hat{\mathbf{d}}_i$ through its range of travel. Our SAMM prototype employs two different approaches. In the case of omniwheels 1 and 3 [see Fig. 2(f)], 1-DOF rotary compliance is employed as illustrated in Fig. 5(a). The rotary axes lie parallel to the respective omniwheel axes. The 90° gearboxes make the rotary axis perpendicular to the respective

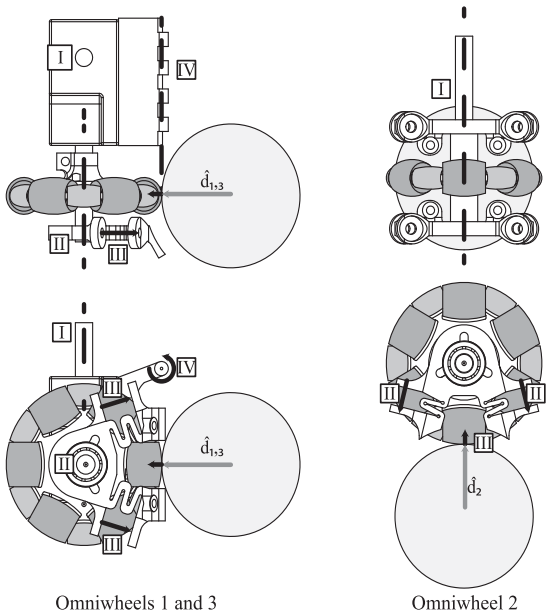

Fig. 5. Compliance at the omniwheel–magnet interface axes $\hat{\mathbf{a}}_i$. (a) Omniwheels 1 and 3 are depicted. The motor's axis (I) is transmitted through the 90° gearbox to the omniwheel's axis (II). Adjustable spring-tensioned pillow blocks provide force (III) between the omniwheel and the magnet, creating compliance (IV) locally parallel with $\hat{\mathbf{d}}_i$. (b) Omniwheel 2 is depicted. The motor's axis and the omniwheel's axis are coaxial, but the remainder of the design is similar.

motor axis, which decouples the direction of compliance from the direction of motor torque transmission (avoiding potential problems related to binding or traction loss). Tension is applied to the omniwheel assemblies by adjustable spring-tensioned pillow blocks constructed of three-dimensional (3-D)-printed ABS plastic with cutouts revealing serpentine-shaped springs, which are reinforced with a silicone compression spring whose tension can be increased or decreased by tightening or loosening an adjustment screw [see Fig. 4(j)]. For omniwheel 2, approximate straight-line motion is formed utilizing two adjustable spring-tensioned pillow blocks, similar to those used on axes 1 and 3, to tension the omniwheel directly onto the magnet in the direction $\hat{\mathbf{d}}_2$, illustrated in Fig. 5(b). Although the motion is not strictly constrained to $\hat{\mathbf{d}}_2$, we have found that the deviation is insignificant.

The Hall-effect sensor cluster depicted in Fig. 3 is fabricated by 3-D printing a housing from ABS plastic with slots in which the Hall-effect sensors are inserted and affixed with adhesive. The nominal positions and sensing directions of the sensors are given in Table I. However, as we describe in Section VIII, the values were updated using a calibration procedure.

Our SAMM prototype is intended to be mounted as the end-effector of a robotic manipulator [see Fig. 1(a)]. In this configuration, the SAMM can be positioned so that its distal surface [the hemispherical side where three of the four set-screws are

TABLE I
HALL-EFFECT SENSOR PARAMETERS FOR SAMM PROTOTYPE

Sensor	Nominal Position Vector $\mathbf{p}_i^{\mathsf{T}}$ (mm)	Nominal Sensing Direction $\mathbf{v}_i^{\mathsf{T}}$	Calibrated Position Vector $\mathbf{p}_i^{\mathsf{T}}$ (mm)	Calibrated Sensing Direction $\mathbf{v}_i^{\mathsf{T}}$
1	$[0 \quad 0 \quad 51.0]$	$[0 \quad 0 \quad 1]$	$[-0.611 \quad 0.112 \quad 50.8]$	$[0.00520 \quad -0.0604 \quad 0.998]$
2	$[0 \quad 0 \quad 58.5]$	$[0 \quad 0 \quad 1]$	$[-0.953 \quad -0.101 \quad 59.0]$	$[0.0126 \quad 0.0527 \quad 0.999]$
3	$[3.75 \quad 0 \quad 54.7]$	$[1 \quad 0 \quad 0]$	$[4.38 \quad 0.0474 \quad 55.3]$	$[0.995 \quad -0.0969 \quad -0.0148]$
4	$[-3.75 \quad 0 \quad 54.7]$	$[1 \quad 0 \quad 0]$	$[-4.03 \quad 0.407 \quad 55.9]$	$[0.987 \quad -0.133 \quad -0.0948]$
5	$[0 \quad 3.75 \quad 54.7]$	$[0 \quad 1 \quad 0]$	$[-0.0210 \quad 3.78 \quad 55.2]$	$[0.0453 \quad 0.998 \quad 0.0359]$
6	$[0 \quad -3.75 \quad 54.7]$	$[0 \quad 1 \quad 0]$	$[0.0768 \quad -3.52 \quad 54.6]$	$[0.0894 \quad 0.996 \quad -0.0388]$

Note: See Section IV for parameter definitions.

located, as shown in Fig. 4(k)], which is streamlined and free of moving parts, is presented to the manipulation workspace (e.g., a human body), reducing the risk of collisions or damage to the moving SAMM components and enabling the actuator magnet to be positioned close to the remote magnetic device being manipulated in order to maximize the strength of the applied magnetic field. In our case, we use a 6-DOF manipulator, but a 3-DOF Cartesian manipulator would be sufficient due to the 3-DOF of the SAMM.

VIII. EXPERIMENTATION

All experiments were performed with the SAMM mounted to a 6-DOF Yaskawa Motoman robotic manipulator, which is housed in an enclosure to mitigate environmental disturbances. The SAMM was always oriented "vertically," as depicted in Fig. 1. The control system and data recording were implemented in C++ and using a Sensoray 626 PCI DAQ card. The control system is designed in a multithreaded structure with the control loop, the Kalman-estimator loop, and the SAMM I/O loop all operating at 200 Hz.

A. Parameter Estimation

1) Coulomb and Viscous Friction: Friction in the SAMM was estimated using a directional Coulomb-plus-viscous friction model described in Section III. The friction parameters were experimentally obtained by driving the motors at open-loop velocities ranging, in discrete increments, from 0 to 2π rad/s. Each increment lasted for 30 s while the resulting motor torque ($\boldsymbol{\tau}_{\mathrm{a}}$) and sensed motor angular velocity ($\boldsymbol{\omega}_{\mathrm{a}}$) were recorded at a rate of 20 Hz. The motor torque is automatically computed by the Maxon motor controllers that drive the three motors. Lines were fit to the positive- and negative-velocity data [21], using least squares, whose y-intercept and slope corresponding to the Coulomb friction ($\mathbf{c}$) and viscous friction ($\mathbf{B}$), respectively, were found to be

$$\mathbf{B}^{+} = \mathrm{diag}\,(0.0001, 0.0014, 0.0001)\ \mathrm{N}\cdot\mathrm{s/rad},$$
$$\mathbf{B}^{-} = \mathrm{diag}\,(0.00001, 0.0014, 0.0005)\ \mathrm{N}\cdot\mathrm{s/rad},$$
$$\mathbf{c}^{+} = [0.0632 \ \ 0.0411 \ \ 0.0436]^{\mathsf{T}}\mathrm{N},$$
$$\mathbf{c}^{-} = [-0.0455 \ \ -0.0330 \ \ -0.0723]^{\mathsf{T}}\mathrm{N}.$$

2) Sensor Noise: Noise from each of the sensors is modeled with the observation covariance matrix $\mathbf{R}$ described in Section V. The submatrix of $\mathbf{R}$ that corresponds to the Hall-sensor covariance is directly estimated by removing the spherical magnet from the SAMM and reading the idle sensor values to determine their intrinsic noise. The submatrix corresponding to the angular-velocity-measurement covariance is measured by recording the covariance of the angular-velocity sensor values with the motors driven open-loop with a constant input (which we assume results in approximately constant motor angular velocity). In both cases, sensor data are collected at a rate of 20 Hz for a duration of 10 min. The covariances and means of the first 50% of the data were compared to the final 50% to verify that the estimation had converged and enough data were collected. Each sensor was independently evaluated for a dc offset, which is then removed in implementation to ensure that the noise measured by each sensor is zero-mean. Note that we assume the Hall-sensor measurements to be independent from the angular-velocity measurements, which causes the off-diagonal terms of $\mathbf{R}$ to be zero. The observation covariance measured and implemented in our SAMM prototype is given as

$$\mathbf{R} = \mathrm{diag}(2.9, 2.9, 2.9, 2.8, 2.9, 2.8, 6.0, 6.0, 6.0)\cdot 10^{-3}$$

where the units of the top-left 6×6 submatrix of $\mathbf{R}$ is mT^2, and the bottom-right 3×3 submatrix of $\mathbf{R}$ have units $\mathrm{rad}^2/\mathrm{s}^2$.

3) Process Noise: Process noise, represented by the covariance matrix $\mathbf{Q}$, is difficult to measure directly, so we experimentally tuned the process-noise covariance to produce desirable tracking performance:

$$\mathbf{Q} = \mathrm{diag}(0.002, 0.002, 0.002, 2.0, 2.0, 2.0).$$

The top-left 3×3 submatrix, which corresponds to heading uncertainty, was set to the value of δ (0.001 in the prototype SAMM) multiplied by the value used in the bottom-right 3×3 submatrix, which in turn corresponds to the magnet's angular-velocities uncertainty represented by a constant multiplied by an identity matrix; the rationale behind this choice is that dipole heading is estimated by integrating angular velocity over one time step, so angular-velocity error is mapped to heading error in a predictable way. This constraint reduced the tuning search to a 1-DOF search. Similar to the structure of $\mathbf{R}$, the off-diagonal terms of $\mathbf{Q}$ have been set to zero as we assume all of the states to be independent. The units of $\mathbf{Q}$ correspond to the units of the

state, where the upper left block matrix denotes the covariance of the dipole heading (which is a unitless heading on the unit-sphere), and the lower right block matrix is the covariance of the dipole's angular velocity measured in rad^2/s^2.

4) Hall-Effect Sensor Calibration: Discrepancies in the Hall-effect sensors' nominal design values (see Table I) will lead to errors when estimating the magnet's dipole heading. To address this problem, the 5-DOF pose of each of the SAMM's six Hall-effect sensors was calibrated, utilizing an external three-axis Metrolab THM1176-LF gaussmeter mounted below the SAMM. To find the position directly below the magnet, a manual gradient-ascent search was employed by moving the SAMM in a horizontal plane to find the location that resulted in the maximum field component in the vertical direction, which is known from (12) to occur directly below the magnet if the dipole is oriented vertically. The search was accomplished by alternately moving the SAMM in a 1 mm grid pattern and manually adjusting the omniwheels to maximize the vertical field component measured. Upon convergence, we knew the magnet was located directly above the gaussmeter, and that it was oriented vertically. The distance of the dipole above the sensor is then calculated using (12) and knowledge of the dipole's magnitude.

Next, with the SAMM's position stationary, 26 random dipole headings were generated by randomly moving the omniwheels between each trial. For each dipole heading, the SAMM's Hall-effect sensor data and the gaussmeter data were collected. With a known and constant position vector, we used the gaussmeter readings to approximate the true heading $\hat{\mathbf{m}}$ of the dipole for each of the 26 tests, using the Levenberg–Marquardt least-squares algorithm in MATLAB to minimize $\|\mathbf{h}_e - \mathbf{h}_m\|^2$, where $\mathbf{h}_m$ is the 3-D field measured by the gaussmeter, and $\mathbf{h}_e$ is the field estimated by (12) using the current estimate of $\hat{\mathbf{m}}$.

Next, using our dataset with known dipole headings, a similar method was utilized to estimate the 5-DOF pose of each Hall-effect sensor independently, using the complete dataset. The point-dipole equation is projected onto the measuring axis of each sensor, $\hat{\mathbf{v}}_i$, to estimate the scalar magnetic field at each sensor position as in (11). Starting from the initial nominal estimates in Table I, the unit vector $\hat{\mathbf{v}}_i$ and the position vector $\mathbf{p}_i$ are approximated using a constrained nonlinear least-squares algorithm to minimize $\|\mathbf{s_e} - \mathbf{s_m}\|^\mathbf{2}$, where $\mathbf{s_m}$ is an array of scalar field measurements by an individual sensor at each of the 26 dipole headings, and $\mathbf{s_e}$ contains the corresponding values estimated by (11) using the current estimates of $\hat{\mathbf{v}}_i$ and $\mathbf{p}_i$. To average sensor noise, 100 measurements from each of the 26 dipole headings were recorded, for a total of 2600 measurements per sensor.

Finally, this calibration process was tested by comparing an additional ten random dipole headings measured by the gaussmeter with those reported by the SAMM sensors. The error across these ten tests was $1.5^\circ \pm 0.6^\circ$ (mean $\pm$ standard deviation). For comparison, using the nominal values from Table I in (14) would have resulted in an error across these ten tests of $5.3^\circ \pm 2.6^\circ$. Note that in our calibration procedure, we assumed that the Hall-effect sensors' sensitivities were accurately provided by the manufacturer. This assumption will lead to a small error in the calibrated position $\mathbf{p}_i$ in Table I (increased/decreased sensitivity would translate the sensor's position estimate radially inward/outward from the dipole), but the resulting estimated dipole heading will be the same.

B. Controller Tuning

This section describes the gain tuning for both controllers introduced in Section VI. In order to implement the proportional pointing-mode and "orthogonal" rotating-mode controllers, which are both effectively forms of heading regulation, we must select the respective controller gains. The Ziegler–Nichols tuning method is a heuristic-based approach to tuning such controllers [30]. The method involves creating a proportional controller and slowly increasing its gain until marginal stability is observed (i.e., when the experimentally observed oscillations are neither decreasing nor increasing over time). This gain defines the "ultimate gain" k_u, and the period of the resulting oscillations defines the "ultimate period" t_u. These identified parameters, which are specific to the SAMM for a given magnitude of step input (since the SAMM is not a linear system), are used to determine all relevant gains. The tuning parameters were experimentally found to be $k_u = 21.0$ s^{-1} and $t_u = 0.65$ s, when tuning for a step-input magnitude of 5°. The Ziegler–Nichols formulation for a proportional controller, which sets $k_p = 0.5\,k_u = 10.5$ s^{-1}, was found to generate desirable performance in both the pointing and rotating modes.

C. Performance Demonstrations

1) Pointing Mode: To test the pointing mode, we performed a Monte Carlo experiment where the SAMM was initialized with the dipole moment $\hat{\mathbf{m}}$ at a random heading and then commanded to go to a new desired heading in a random direction with an angular change of 5°, 90°, or 175°. In total, 150 random trials were performed, with 50 trials for each magnitude of angular change. Each random heading was held constant for 10 s. The root-mean-square (RMS) error was measured during the last 5 s of each trial. Across the 150 trials, the RMS error mean $\pm$ standard deviation was $0.2^\circ \pm 0.1^\circ$.

During the Monte Carlo experiment, we measured the time required to converge to each random desired heading for each magnitude of angular change. The convergence time t_c was defined as the time to reach and stay within 1.0° of the desired heading. Fig. 6(a) shows the mean and standard deviation of t_c as a function of the step input θ's magnitude. There is no appreciable difference in t_c at 5° and 90°; the increase in t_c at 175° is likely due to saturation from hardware limitations, which occurs for steps larger than approximately 103° in our system. The best and worst case time responses for each magnitude are depicted in Fig. 6(b). It is worth noting that we did occasionally observe slip between the omniwheels at the magnet, which did not cause any problems in control.

2) Rotating Mode: The rotating mode was tested by selecting five axes to rotate the dipole moment around at three selected speeds (0.5, 1.5, and 2.5 Hz). The five axes were the $\hat{\mathbf{x}}$, $\hat{\mathbf{y}}$, and $\hat{\mathbf{z}}$ axes (see Fig. 2), and the omniwheel axes $\hat{\mathbf{a}}_1$ and $\hat{\mathbf{a}}_3$. (Note that $\hat{\mathbf{z}}$ and the omniwheel axis $\hat{\mathbf{a}}_2$ are parallel.) To evaluate the SAMM's ability to drive the dipole moment to the desired ro-

TABLE II
DIPOLE MOMENT WAS ROTATED ABOUT FIVE DISTINCT AXES FOR 30 S EACH

κ		x			y			z & $\mathbf{a}_2$			$\mathbf{a}_1$			$\mathbf{a}_3$		
ω_m (Hz)		0.5	1.5	2.5	0.5	1.5	2.5	0.5	1.5	2.5	0.5	1.5	2.5	0.5	1.5	2.5
45°	$\epsilon_\perp$ (deg)	0.83	1.35	1.53	1.61	3.13	4.41	1.05	2.06	2.70	1.27	3.37	3.22	1.65	3.43	4.19
	t_s (sec)	0.28	0.41	0.41	0.26	0.20	0.25	0.30	0.57	0.46	0.37	0.61	0.41	0.32	0.60	0.40
	ϵ_κ (Hz)	0.02	0.02	0.02	0.05	0.05	0.04	0.01	0.01	0.01	0.03	0.04	0.03	0.02	0.02	0.02
90°	$\epsilon_\perp$ (deg)	1.08	2.01	1.35	1.54	4.83	4.41	0.82	1.82	2.50	1.30	2.25	**2.65**	1.17	3.15	3.86
	t_s (sec)	0.38	0.43	0.38	0.38	0.26	0.50	0.36	0.25	0.26	0.33	0.65	**0.42**	0.43	0.43	0.31
	ϵ_κ (Hz)	0.02	0.02	0.02	0.07	0.05	0.04	0.01	0.01	0.01	0.04	0.04	**0.03**	0.02	0.02	0.02

Note: $\epsilon_\perp$ is the RMS angular error from the desired plane and ϵ_κ is the RMS angular velocity error during the last 15 s of rotation. The settling time (t_s) is defined as the time from rest to the dipole moment first crossing the desired plane. Bold response is shown in Fig. 7.

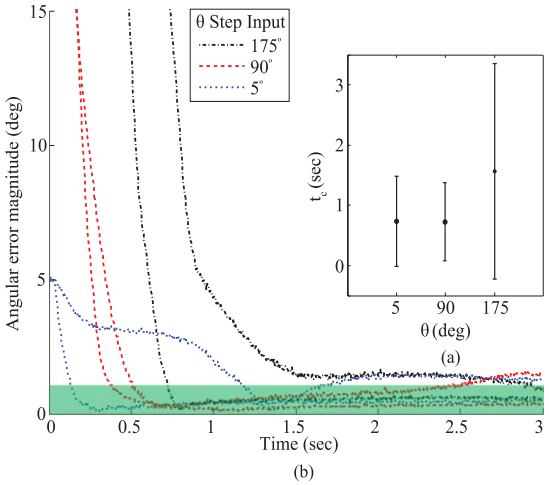

Fig. 6. (a) Inset shows the mean ± standard deviation of the convergence time to the desired heading with random changes in heading of angular magnitude θ. 50 trials were performed for each angular magnitude. (b) Best and worst case convergence time responses for each of the tested step-input magnitudes.

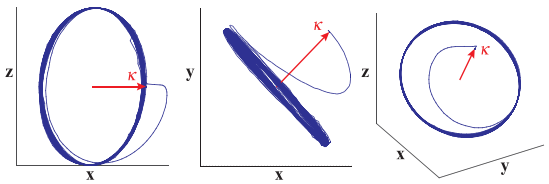

Fig. 7. Multiple views of a typical response using the rotating-mode controller with the dipole heading starting 90° off the desired plane and $\hat{\boldsymbol{\kappa}} = \hat{\mathbf{a}}_1$ at 2.5 Hz. The corresponding trial is bold in Table II.

tation plane, the dipole moment was started with a heading of either 45° or 90° off the desired rotation plane. Table II gives the RMS error in angular error off the desired rotation plane ($\epsilon_\perp$), the time required to converge to the plane t_s, and the RMS error in angular speed (ϵ_κ). Note that $\epsilon_\perp$ and ϵ_κ were both calculated from the last 15 s of each trial. Rotation axes do not perform identically across the workspace as illustrated in Table II due to nonlinearities and slight differences in the omniwheels. As expected, $\epsilon_\perp$ generally increases as the angular speed increases. Fig. 7 depicts a typical response with $\hat{\boldsymbol{\kappa}} = \hat{\mathbf{a}}_1$ at 2.5 Hz.

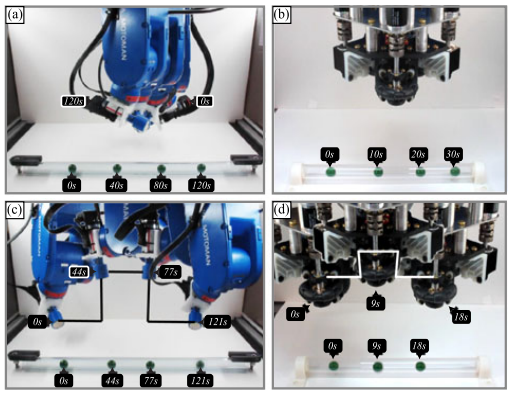

Fig. 8. (a) In prior work [1], a spherical UMD was rolled down a lumen using a rotating field generated by a permanent-magnet actuator, whose position was held stationary while its rotation axis was controlled appropriately. (b) For comparison, performing the same maneuver with the SAMM requires no motion of the robot manipulator. (c) In another example from [1], the UMD is rolled down a lumen while the permanent-magnet actuator's position follows a trajectory independent of the UMD's position while its rotation axis was controlled appropriately. (d) For comparison, when using the SAMM the manipulator's wrist only moves slightly to keep the SAMM in a constant orientation.

Next, we demonstrate the benefits of the SAMM relative to previous permanent-magnet actuation technology. In [1], we performed experiments where a spherical UMD was propelled down a lumen using a rotating field generated by a cylindrical permanent magnet as the UMD's position $\mathbf{p}$ was continuously measured by a stereo-camera system. The actuator magnet was rigidly attached orthogonally to the shaft of a DC motor, which was maneuvered in space by the same robotic manipulator used in this paper to control the magnet's rotation axis $\hat{\boldsymbol{\kappa}}$ according to

$$\hat{\boldsymbol{\kappa}} = \widehat{\mathbf{H}(\mathbf{p})\hat{\boldsymbol{\kappa}}_\mathbf{h}} \tag{36}$$

where $\hat{\boldsymbol{\kappa}}_\mathbf{h}$ is the instantaneous magnetic-field rotation axis that causes the UMD to roll down the lumen, and $\mathbf{H}(\mathbf{p}) = 3\hat{\mathbf{p}}\hat{\mathbf{p}}^\mathsf{T} - \mathbf{I}_3$ [1]. In one experiment, the UMD was rolled down the lumen while the Cartesian position of the actuator magnet was kept stationary [see Fig. 8(a)], which required the actuator-magnet's rotation axis, and thus the robot manipulator's wrist, to turn almost 180°. For comparison, Fig. 8(b) shows a similar experiment using the SAMM, but in this case the manipulator remains completely stationary. In a second experiment, the UMD was rolled down the lumen while the Cartesian position

of the actuator magnet followed a step trajectory independent of the UMD's position [see Fig. 8(c)], and the necessary actuator-magnet rotation axis from (36) caused the robot manipulator's wrist to contort dramatically (nearly violating joint limits at $t = 77$ s). For comparison, Fig. 8(d) shows a similar experiment performed with the SAMM. In this case, the manipulator's wrist remains nearly stationary throughout the trajectory, only changing slightly to keep the SAMM in a constant orientation. In both experiments, the SAMM dramatically reduces the manipulator motion required to perform the maneuvers. Note that both experiments were possible with the SAMM held in a constant orientation, demonstrating that a much simpler robot manipulator (e.g., a Cartesian gantry robot) could have been used to accomplish the same results.

IX. Conclusion

We have presented the spherical-actuator-magnet manipulator (SAMM), which is a singularity-free permanent-magnet robot end-effector for magnetic manipulation. The SAMM uses three omniwheels to enable holonomic control of a spherical magnet's heading and enable the magnet's rotation axis to be set arbitrarily. The SAMM performs closed-loop control of its magnet's heading using field measurements obtained from Hall-effect sensors as feedback, combined with modeled dynamics, using an extended Kalman filter. We experimentally characterized the quasi-static error in the estimate of the dipole's heading to be $1.5^\circ \pm 0.6^\circ$ (mean $\pm$ standard deviation). We described the operation and construction of the SAMM, developed and characterized pointing-mode and rotating-mode controllers, and demonstrated remote actuation of an untethered magnetic device in a lumen. Prior work in magnetic manipulation using permanent-magnet actuation was limited by robot joint limitations and singularities, but the SAMM end-effector substantially eliminates these limitations.

References

[1] A. W. Mahoney and J. J. Abbott, "Generating rotating magnetic fields with a single permanent magnet for propulsion of untethered magnetic devices in a lumen," *IEEE Trans. Robot.*, vol. 30, no. 2, pp. 411–420, Apr. 2014.

[2] A. W. Mahoney and J. J. Abbott, "Five-degree-of-freedom manipulation of an untethered magnetic device in fluid using a single permanent magnet with application in stomach capsule endoscopy," *Int. J. Robot. Res.*, vol. 35, no. 1–3, pp. 129–147, 2016.

[3] B. J. Nelson, I. K. Kaliakatsos, and J. J. Abbott, "Microrobots for minimally invasive medicine," *Annu. Rev. Biomed. Eng.*, vol. 12, pp. 55–85, 2010.

[4] J. L. Toennies, G. Tortora, M. Simi, P. Valdastri, and R. J. Webster III, "Swallowable medical devices for diagnosis and surgery: the state of the art," *J. Mech. Eng. Sci.*, vol. 224, no. 7, pp. 1397–1414, 2010.

[5] G. Ciuti, P. Valdastri, A. Menciassi, and P. Dario, "Robotic magnetic steering and locomotion of capsule endoscope for diagnostic and surgical endoluminal procedures," *Robotica*, vol. 28, no. 2, pp. 199–207, 2010.

[6] M. T. Hou, H.-M. Shen, G.-L. Jiang, C.-N. Lu, I -J. Hsu, and J. A. Yeh, "A rolling locomotion method for untethered magnetic microrobots," *Appl. Phys. Lett.*, vol. 96, pp. 1–3, 2010, Art. no. 024102.

[7] S. Yim and M. Sitti, "Design and rolling locomotion of a magnetically actuated soft capsule endoscope," *IEEE Trans. Robot.*, vol. 28, no. 1, pp. 183–194, Feb. 2012.

[8] A. W. Mahoney and J. J. Abbott, "Managing magnetic force applied to a magnetic device by a rotating dipole field," *Appl. Phys. Lett.*, vol. 99, pp. 1–3, 2011, Art. no. 134103.

[9] J.-S. Lee, B. Kim, and Y.-S. Hong, "A flexible chain-based screw propeller for capsule endoscopes," *Int. J. Precis. Eng. Manuf.*, vol. 10, no. 4, pp. 27–34, 2009.

[10] L. Zhang, J. J. Abbott, L. X. Dong, B. E. Kratochvil, D. Bell, and B. J. Nelson, "Artificial bacterial flagella: Fabrication and magnetic control," *Appl. Phys. Lett.*, vol. 94, pp. 1–3, 2009, Art. no. 064107.

[11] K. Ishiyama, K. I. Arai, M. Sendoh, and A. Yamazaki, "Spiral-type micro-machine for medical applications," *J. Micromechatronics*, vol. 2, no. 1, pp. 77–86, 2003.

[12] G. T. Gillies, R. C. Ritter, W. C. Broaddus, M. S. Grady, M. A. Howard III, and R. G. McNeil, "Magnetic manipulation instrumentation for medical physics research," *Rev. Sci. Instrum.*, vol. 65, no. 3, pp. 533–562, 1994.

[13] J. R. Clark, L. Leon, F. M. Warren, and J. J. Abbott, "Magnetic guidance of cochlear implants: Proof-of-concept and initial feasibility study," *J. Med. Devices*, vol. 6, 2012, Art. no. 035002.

[14] R. C. O'Handley, *Modern Magnetic Materials*. Hoboken, NJ, USA: Wiley, 2000.

[15] E. P. Furlani, *Permanent Magnet and Electromechanical Devices: Materials, Analysis, and Applications*. San Diego, CA, USA: Academic, 2001.

[16] M. Kumaga and T. Ochiai, "Development of a robot balanced on a ball: Application of passive motion to transport," in *Proc. IEEE Int. Conf. Robot. Autom.*, 2009, pp. 4106–4111.

[17] U. Nagarajan, G. Kantor, and R. Hollis, "The ballbot: An omnidirectional balancing mobile robot," *Int. J. Robot. Res.*, vol. 33, no. 6, pp. 917–930, 2014.

[18] M. Kumaga and R. L. Hollis, "Development of a three-dimensional ball rotation sensing system using optical mouse sensors," in *Proc. IEEE Int. Conf. Robot. Autom.*, 2011, pp. 5038–5043.

[19] L. Yan, I.-M. Chen, G. Yang, and K.-M. Lee, "Analytical and experimental investigation on the magnetic field and torque of a permanent magnet spherical actuator," *IEEE/ASME Trans. Mechatronics*, vol. 11, no. 4, pp. 409–419, Aug. 2006.

[20] S. E. Wright, A. W. Mahoney, K. M. Popek, and J. J. Abbott, "A spherical-magnet end-effector for robotic magnetic manipulation," in *Proc. IEEE Int. Conf. Robot. Autom.*, 2015, pp. 1190–1195.

[21] S. E. Wright, "A singularity-free mechanism for holonomic orientation control of a spherical permanent magnet," Master's thesis, Univ. Utah, Salt Lake City, UT, USA, 2014.

[22] H. Olsson, K. J. Åström, C. Canudas de Wit, M. Gäfvert, and P. Lischinsky, "Friction models and friction compensation," *Eur. J. Control*, vol. 4, no. 3, pp. 176–195, 1998.

[23] A. J. Petruska and J. J. Abbott, "Optimal permanent-magnet geometries for dipole field approximation," *IEEE Trans. Magn.*, vol. 49, no. 2, pp. 811–819, Feb. 2013.

[24] R. A. Horn and C. R. Johnson, *Matrix Analysis*, reprint ed. Cambridge, U.K.: Cambridge Univ. Press, 1985.

[25] D. Simon, *Optimal State Estimation*, 1st ed. Hoboken, NJ, USA: Wiley, 2006.

[26] T. W. R. Fountain, P. V. Kailat, and J. J. Abbott, "Wireless control of magnetic helical microrobots using a rotating-permanent-magnet manipulator," in *Proc. IEEE Int. Conf. Robot. Autom.*, 2010, pp. 576–581.

[27] A. Ghosh and P. Fischer, "Controlled propulsion of artificial magnetic nanostructured propellers," *Nano Lett.*, vol. 9, no. 6, pp. 2243–2245, 2009.

[28] M. Sendoh, K. Ishiyama, and K. I. Arai, "Fabrication of magnetic actuator for use in a capsule endoscope," *IEEE Trans. Magn.*, vol. 39, no. 5, pp. 3232–3234, Sep. 2003.

[29] K.-S. Byun and J.-B. Song, "Design and construction of continuous alternate wheels for an omnidirectional mobile robot," *J. Robot. Syst.*, vol. 20, no. 9, pp. 569–579, 2003.

[30] J. G. Ziegler and N. B. Nichols, "Optimum settings for automatic controllers," *Trans. ASME*, vol. 64, no. 11, pp. 759–768, 1942.

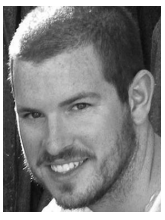

Samuel E. Wright received the B.S. and M.S. degrees in mechanical engineering from University of Utah, Salt Lake City, UT, USA, in 2012 and 2014, respectively.

After graduation, he was an Automation Engineer with Janicki Industries, Layton, UT, USA. He is currently with Sarcos Robotics, Salt Lake City, UT, USA.

Arthur W. Mahoney (S'10–M'15) received the B.S. degree in computer science from Utah State University, Logan, UT, USA, in 2009 and the Ph.D. degree in computing from University of Utah, Salt Lake City, UT, USA, in 2014.

He is a Postdoctoral Researcher with Vanderbilt University, Nashville, TN, USA.

Dr. Mahoney received an NSF IGERT Traineeship and an NSF Graduate Research Fellowship. He also received the Best Poster Award at the 2013 Hamlyn Symposium on Medical Robotics.

Katie M. Popek (S'06–M'16) received the B.S. degree in electrical engineering from University of Nebraska, Lincoln, NE, USA, in 2010 and the Ph.D. degree in computing from University of Utah, Salt Lake City, UT, USA, in 2017.

She is with The Johns Hopkins University Applied Physics Laboratory, Laurel, MD, USA.

Dr. Popek received an NSF IGERT Traineeship and an NSF Graduate Research Fellowship.

Jake J. Abbott (S'03–M'05) received the B.S. degree from Utah State University, Logan, UT, USA, in 1999; the M.S. degree from University of Utah, Salt Lake City, UT, USA, in 2001; and the Ph.D. degree from The Johns Hopkins University, Baltimore, MD, USA, in 2005, all in mechanical engineering.

In 2006, he became a Postdoctoral Researcher with ETH Zurich, Switzerland. In 2008, he joined the Department of Mechanical Engineering, University of Utah, where he is currently an Associate Professor.

Dr. Abbott is a recipient of the NSF CAREER Award. He also received the Best Manipulation Paper Award at the 2010 IEEE International Conference on Robotics and Automation, the Best Poster Award at the 2013 Hamlyn Symposium on Medical Robotics, and the Best Paper Award at the 2014 Haptics Symposium.

CHAPTER 3

SIX-DEGREE-OF-FREEDOM LOCALIZATION OF AN UNTETHERED MAGNETIC CAPSULE USING A SINGLE ROTATING MAGNETIC DIPOLE

The work in this chapter was co-advised by Dr. Jake Abbott and Dr. Thomas Schmid and was published in *IEEE Robotics and Automation Letters*. It is reproduced here without modification. It first develops a capsule approximately 1.2 times larger than commercial capsule-endoscope devices embedded with magnetic sensors. A 6-DOF localization algorithm is described that assumes the capsule has approximately no net motion (i.e., the applied field is rotated above the step-out frequency such that the capsule is not able to remain synchronously rotating with the field). A simple propulsion scheme is implemented where the capsule's movement is periodically paused to re-localize to ensure the pose estimates are sufficiently accurate. The experimental results utilized the SAMM device described in Chapter 2. Table II is not formatted correctly in the published work, the corrected version is shown in the Errata.

Six-Degree-of-Freedom Localization of an Untethered Magnetic Capsule Using a Single Rotating Magnetic Dipole

Katie M. Popek, Thomas Schmid, and Jake J. Abbott

***Abstract*—This paper presents a method to estimate the six-degree-of-freedom pose of a magnetic capsule, with an embedded permanent magnet and Hall-effect sensors, using a rotating dipole field. The method's convergence properties as a function of the number of distinct rotation axes of the applied field and the number of complete rotations about each axis are characterized. Across our tested workspace, the localization error was 4.9 $\pm$ 2.7 mm and 3.3 $\pm$ 1.7 degrees (mean $\pm$ standard deviation). We experimentally demonstrate this is sufficient for propulsion of a screw-type magnetic capsule through a lumen using a single dipole to both propel and localize the capsule.**

***Index Terms*—Localization, medical robots and systems.**

I. Introduction

WIRELESS capsule endoscopes are a promising diagnostic tool, providing the ability to view the entire gastrointestinal tract with minimal patient discomfort. Their effectiveness is currently limited due to their uncontrolled nature, which causes the capsule to miss regions of interest. Researchers have been investigating a variety of methods to actively propel and localize these devices to enable views of the entire gastrointestinal tract painlessly and without anesthesia [1]. Propelling capsules with magnetic fields is clinically feasible [2], and utilizing magnetic fields has the benefit of being able to propel/control [3]–[7] and localize [8]–[17] the capsule using the same technology.

Previous work from our lab characterized the use of a single rotating magnetic dipole positioned in space with a robotic manipulator to propel a screw-type magnetic capsule in a lumen from any position [6]; our experimental verification previously relied on cameras to localize the capsule. In this paper, we describe a companion localization method to estimate the six-degree-of-freedom (6-DOF) pose of a magnetic capsule with no prior location information other than the bounds of its potential workspace, using the same magnetic field that is propelling it. We then apply that estimate to propel a capsule in a lumen.

There are several previously published magnetic localization algorithms, but most rely on external magnetic sensors and are either not compatible with magnetic actuation [8]–[11] or currently have a limited workspace [16]. Methods employing internal magnetic sensors (i.e., inside the capsule) require the addition of an accelerometer [12], [13], provide less than 6-DOF information [12], [16], [17], or must manipulate the position of the external magnetic source during localization [15], [17]. Frequently, localization methods rely on complicated models of the magnetic field [13]–[15], but in certain cases, which we exploit, the external magnetic source can be modeled with the simpler point-dipole equation.

This paper presents a localization method that solves for the 6-DOF pose of a magnetic capsule while it is either stationary or in the "step-out" regime where the field is rotating too quickly for the capsule to rotate synchronously with the field. Similar methods for pose detection in rotating magnetic fields exist [14], [18], but our new method is more robust to sensor noise and data synchronization issues because it utilizes all field-sensor data independently instead of relying solely on the estimated maximum and minimum field magnitudes throughout a rotation cycle, and the entire 6-DOF pose is solved simultaneously rather than solving for position and orientation sequentially. Previous methods only rotated the field about a single axis, but we show that using additional rotation axes improves accuracy. Our improved localization method was briefly introduced in [19]. In this paper, we provide further experimental validation and analysis of the convergence properties, and we experimentally demonstrate this method's accuracy is sufficient to propel a magnetic capsule by combining the localization method and our previously published propulsion method [6].

The paper is organized as follows: Section II details our localization method. Section III describes our experimental hardware. Section IV simulates the expected results based on our method (II) and hardware (III). Section V provides experimental verification. Finally, Section VI demonstrates propulsion of a capsule using our localization method to provide position and heading feedback.

II. Localization Method

Assume that the rotating magnetic dipole (i.e., the external magnet) is positioned in space by a robotic manipulator, and

Manuscript received May 9, 2016; revised July 28, 2016; accepted August 29, 2016. Date of publication September 12, 2016; date of current version September 26, 2016. This paper was recommended for publication by Associate Editor J. Nieto and Editor C. Stachniss upon evaluation of the reviewers comments. This work was supported by the National Science Foundation under Grants 0952718 and 0654414.

K. M. Popek is with the School of Computing and the Robotics Center, University of Utah, Salt Lake City, UT 84112 USA (e-mail: katie.popek@utah.edu).

T. Schmid is with the Department of Electrical and Computer Engineering, University of Utah, Salt Lake City, UT 84112 USA (e-mail: thomas.schmid@utah.edu).

J. J. Abbott is with the Department of Mechanical Engineering and the Robotics Center, University of Utah, Salt Lake City, UT 84112 USA (e-mail: jake.abbott@utah.edu).

This paper has supplementary downloadable material available at http://ieeexplore.ieee.org, provided by the author.

Color versions of one or more of the figures in this letter are available online at http://ieeexplore.ieee.org.

Digital Object Identifier 10.1109/LRA.2016.2608421

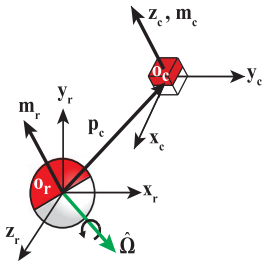

Fig. 1. Overall system setup with the robot frame origin ($\mathbf{o}_r$) at the center of the external magnetic source and the capsule frame ($\mathbf{o}_c$) at the center of the capsule's internal permanent magnet.

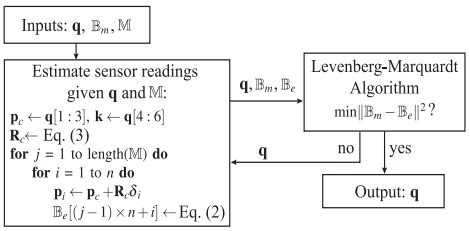

Fig. 2. A diagram depicting our localization method. $\mathbb{B}_m$ is an array of sensor measurements in one batch of data, $\mathbb{M}$ is the set of $\mathbf{m}_r$ corresponding in time to each set of n sensor measurements in $\mathbb{B}_m$, and $\mathbf{q}$ is the capsule's state, which is iteratively updated from an initial guess.

the dipole is located at the center of the robot's tool frame, $\mathbf{o}_r$, which is also our reference frame. The capsule's coordinate-frame origin, $\mathbf{o}_c$, resides at the center of the capsule's internal magnet. There exists some vector $\mathbf{p}_c$ that corresponds to the displacement between the two coordinate-frame origins as shown in Fig. 1. There also exists a rotation matrix, $\mathbf{R}_c$, that rotates the capsule's coordinate-frame to align with the robot's. By solving for the position vector, $\mathbf{p}_c$, and the rotation matrix, $\mathbf{R}_c$, the capsule's position and orientation relative to the external magnetic source is known.

The following assumptions were made in developing this method: 1) The position and orientation of the external dipole moment, $\mathbf{m}_r$, are known relative to a global frame. 2) $\mathbf{m}_r$ is rotated about an axis $\hat{\mathbf{\Omega}}$ such that $\mathbf{m}_r^T\hat{\mathbf{\Omega}} = 0$ is always true (throughout this paper, we use the "hat" symbol $\hat{}$ to indicate a unit vector). 3) The capsule is free to move, but the dipole-field rotation is well above the step-out frequency, such that we can assume no net motion, and decouple the localization and propulsion of the capsule; existing state-estimation methods can be used to ensure this is true [20]. 4) The field of the external magnet can be accurately modeled by the point-dipole equation [21]:

$$\mathbf{b}(\mathbf{p}_c) = \frac{\mu_0}{4\pi||\mathbf{p}_c||^5}\left(3\mathbf{p}_c\mathbf{p}_c^T - \mathbf{I}||\mathbf{p}_c||^2\right)\mathbf{m}_r = \frac{\mu_0}{4\pi||\mathbf{p}_c||^5}\mathbf{B}\mathbf{m}_r \tag{1}$$

where μ_0 is the permeability of free space, $\mathbf{I}$ is the identity matrix, and $\mathbf{B} = \mathbf{B}(\mathbf{p}_c)$ is a symmetric matrix. In our setup, we use a spherical permanent magnet as the external source, which is accurately approximated by (1); errors introduced by other external-magnet geometries are quantified in [22].

Consider a set of n magnetic sensors embedded inside the capsule, each with a constant known position offset, $\boldsymbol{\delta}_i$, and orientation, $\mathbf{s}_i$, expressed in the capsule frame. The position vector, $\mathbf{p}_i$, describing the position of sensor i in the robot frame, is $\mathbf{p}_i = \mathbf{p}_c + \mathbf{R}_c\boldsymbol{\delta}_i$. The scalar magnetic-field projection measured at each sensor is found by projecting (1) onto the measuring axis of the sensor, $\mathbf{s}_i$:

$$b_i(\mathbf{p}_i) = \mathbf{s}_i^T\mathbf{R}_c^T\frac{\mu_0}{4\pi||\mathbf{p}_i||^5}\left(3\mathbf{p}_i\mathbf{p}_i^T - \mathbf{I}||\mathbf{p}_i||^2\right)\mathbf{m}_r \tag{2}$$

From [23], a rotation matrix can be reduced to three variables using its exponential form:

$$\mathbf{R}_c = e^{\mathbf{S}\{\mathbf{k}\}} \tag{3}$$

where $\mathbf{S}\{\mathbf{k}\}$ is a skew-symmetric matrix packing of the angle-axis representation $\mathbf{k} = \hat{\mathbf{k}}\theta$.

The capsule's full 6-DOF pose is represented by $\mathbf{q} = \begin{bmatrix}\mathbf{p}_c^T & \mathbf{k}^T\end{bmatrix}^T$. We use the nonlinear least-squares Levenberg-Marquardt algorithm [24] to estimate the capsule pose by minimizing the cost function $c = ||\mathbb{B}_m - \mathbb{B}_e||^2$, where $\mathbb{B}_m$ is an array of the measured magnetic field readings, and $\mathbb{B}_e$ is an array of the magnetic field readings estimated by (2). A diagram of our method is shown in Fig. 2; the capsule's state is iteratively manipulated using the Levenberg-Marquardt algorithm until a minimum c is found. We use a numerically approximated Jacobian in our testing, both in MATLAB (calculated by default when using *lsqnonlin()*) and in C++ with the NonLinearOptimization module of the Eigen library [25].

A static magnetic field does not provide enough information to uniquely determine the capsule's pose; additional data must be obtained by either translating or rotating the external dipole. This method can be utilized in applications with any changing applied magnetic field that can be modeled by (1), however, this paper deals exclusively with a rotating dipole field to be consistent with our previous propulsion method [6]. Using a dipole field that rotates about only one axis will result in limited information in certain configurations; for example, if the dipole is located along the axis of rotation of the capsule, the field's magnitude along the capsule's axis may remain constant throughout the rotation of the dipole. As detailed in [18], there also exist multiple poses in the workspace that produce the same magnetic field if the dipole is rotated about only one axis. Because we do not have prior knowledge of the capsule's pose, the choice of a single $\hat{\mathbf{\Omega}}$ for robust localization across the entire workspace is not feasible. To span the workspace, we chose to populate $\mathbb{B}_m$ by rotating the dipole source about its three coordinate-frame axes $(\mathbf{x}_r, \mathbf{y}_r, \mathbf{z}_r)$ successively for a single dataset. The number of distinct $\hat{\mathbf{\Omega}}$ and the amount of data needed for the algorithm to converge is explored in Section V.

III. Experimental Hardware

A. Magnetic Dipole Source

The experimental setup is shown in Fig. 3(a). The spherical-actuator-magnet manipulator (SAMM) [26] is used as the external dipole. The device provides a singularity-free method for controlling a spherical permanent magnet's dipole orientation

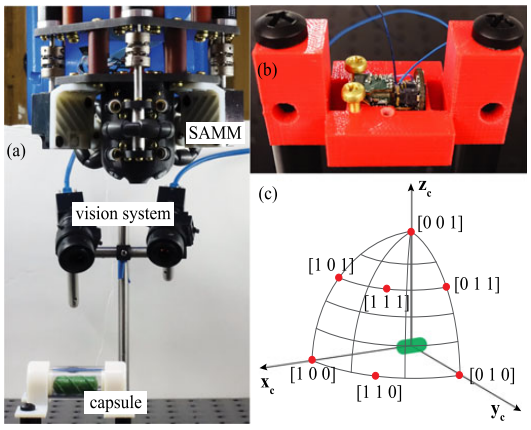

Fig. 3. (a) The experimental setup with the SAMM mounted on the end-effector of a 6-DOF robotic arm, the stereo vision system used for ground truth, and our capsule constrained to a lumen where it is free to rotate about its long axis, but not translate. (b) The test fixture used to rigidly mount the sensor array. (c) Experimentally tested positions of the dipole are denoted by red dots and their corresponding direction vectors in the capsule's frame. The distance to the capsule was varied.

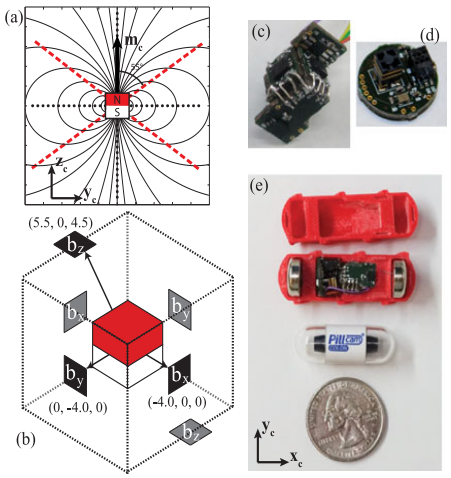

Fig. 4. (a) A magnetic dipole field has regions where the field vector points in a single cardinal direction, denoted by dashed/dotted lines. Place $\mathbf{b_z}$ sensors along the red dashed lines and $\mathbf{b_y}$ sensors in regions denoted by the black dotted lines (with $\mathbf{b_x}$ sensors placed analogously). (b) An isometric view of our final sensor layout with each sensor labeled with its measured field direction, and its position offset in mm with respect to the center of the magnet. The gray sensors are not visible from this angle, but are located at the negative counterpart of the corresponding sensor. (c) The sensor array (i.e., the hardware implementation of (b)) surrounding a permanent magnet. (d) The communications electronics. (e) Our capsule compared to Given Imaging's colon capsule. Along with the electronics shown in (c) and (d) it contains coin cell batteries on each end. The wires connnecting the batteries to the electronics run along the inside of the capsule and are not visible.

by using three mutually orthogonal omniwheels to generate rotation about arbitrary axes. The SAMM is mounted as the end-effector on a Yaskawa Motoman MH5 6-DOF robotic manipulator. We chose our workspace to span between 75–200 mm from the center of the permanent magnet to ensure a high signal-to-noise ratio. Its size is limited by a combination of the strength of the prototype SAMM's permanent magnet and the sensitivity of the Hall-effect sensors. Due the homothetic property of magnetic fields, if the SAMM's magnet radius were scaled by η the field measured at $\eta\mathbf{p}$ would be the same as that measured at $\mathbf{p}$ with the original magnet. Tested locations were normalized by the radius ρ of the SAMM magnet, which is 25.4 mm, to enable our results to generalize to other magnetic field sources. The effect of increasing the sensor's sensitivity is not as straightforward because of the exponential decrease in magnetic field magnitude with distance, but typically more sensitive sensors have a smaller range and thus less measurement noise. When using higher sensitivities, one should ensure the sensing range is large enough to accommodate the desired range of external field measurements when combined with offsets from the internal magnetic field.

To quantify the accuracy of the proposed localization method, the capsule was mounted with accuracy of 1.5 mm and 3° using the test fixture shown in Fig. 3(b). The SAMM was moved relative to the fixed position of the capsule along seven directions spread throughout an octant of the workspace as shown in Fig. 3(c). The distance $||\mathbf{p}_c||$ was varied between 4ρ to 8ρ. At each location, the SAMM's position was held constant and $\mathbf{m}_r$ was rotated about seven different rotation axes, for five complete rotations each, to characterize the convergence properties of the localization method. Ten trials were completed at each location for statistical analysis. To ensure the tests with a stationary capsule give comparable results to more clinically realistic scenarios, the capsule was also tested in a lightly lubricated clear acrylic tube where it was free to rotate (Fig. 3(a)). The SAMM's maximum rotation speed is 3 Hz; to ensure the capsule remained in the step-out regime, these tests were performed at $||\mathbf{p}_c|| = 7\rho$. Closer distances could be achievable using an electromagnetic dipole source such as an Omnimagnet [27] and localizing with rotation speeds of 20–30 Hz, or by constructing a faster SAMM.

B. Prototype Capsule

This method was designed to be used in conjunction with a magnetic capsule with Hall-effect sensors embedded. One of the major problems associated with internal magnetic sensors, if used in conjunction with magnetic propulsion, is their close proximity to the capsule's internal magnet, whose field may dominate the external field we are trying to sense. One option is to employ large-range sensors, but these typically have more noise associated with their measurements at the signals of interest. An alternative, which we first presented in [20], is to strategically surround the internal magnet with six one-axis sensors that have negligible biasing in the sensor measurements from the internal magnet's field. Assuming the capsule's internal magnet can be modeled using (1), there are positions where the magnetic field points in a single cardinal direction as illustrated by the dashed/dotted lines in Fig. 4(a). By using a one-axis Hall-effect sensor, which measures the field component orthogonal to its surface and ignores all other field components, it is possible to place the sensor such that the internal magnet's field is parallel to the sensor's surface and provides negligible interference in its measurements. For example, the sensors measuring the field component in the $\mathbf{z}_c$ direction are placed at locations

where the field vector lies solely in the $\mathbf{x}_c - \mathbf{y}_c$ plane. These positions, denoted by dashed red lines in Fig. 4(a), lie along a line drawn out from the middle of the magnet at an angle of approximately 55° measured from $\mathbf{m}_c$. The $\mathbf{b_x}$ and $\mathbf{b_y}$ sensors are placed in regions parallel and perpendicular to $\mathbf{m}_c$, denoted by black dotted lines in Fig. 4(a). Using this strategy, we placed six sensors, one on each side of a cube, to provide two sensors in each of the three cardinal axes. As a cubic magnet is not perfectly modeled by (1) in the region where the sensors are placed, our final sensor positions were confirmed using finite-element-analysis software. The final sensor layout is illustrated in Fig. 4(b) and was chosen to be as close as possible to the ideal while still being feasible within our hardware constraints.

The sensor array was created using six printed circuit boards (Fig. 4(c)); on each was placed a one-axis Allegro A1392 linear Hall-effect sensor with a range of ±62 mT and a sensitivity of 25 V/T. The boards were mounted directly to the 108 mm^3 cubic NdFeB Grade N52 magnet in the layout shown in Fig. 4(b). Using our sensor configuration, the maximum offset from the internal magnet is 8.2 mT, which is measured by a $\mathbf{b_y}$ sensor. The average field offset across all six sensors is 2.9 mT. This is a significant improvement over the naive alternative of placing the $\mathbf{b_z}$ sensor along the $\mathbf{z}_c$-axis at 4.0 mm, similar to the $\mathbf{b_x}$ and $\mathbf{b_y}$ sensors; the field from the capsule's magnet at this position was measured by a Hirst GM08 gaussmeter as approximately 300 mT, which would saturate the sensor and make it useless. The small constant biases can be subtracted in software because the sensors remain fixed relative to the internal magnet.

The four-layer circular board (Fig. 4(d)) contains all the components to wirelessly transmit the six sensor readings to a computer. A Texas Instruments CC2530 microcontroller (MCU) was chosen for its low-power consumption and its internal transceiver. The MCU uses an interrupt-based approach to transition between the capsule's states and execute functions that require constant timing intervals. During a test, the sensors are read every 10 ms, but are sent wirelessly in batches of five readings per sensor at 20 Hz back to the computer. Before transmission, the measurements are timestamped on the MCU. The MCU and PC clocks are synchronized to ensure each $\mathbf{m}_r$ is correctly attributed to its corresponding sensor measurements by sending a flag to the MCU to start its timers at a known PC time. Two 1.55 V silver-oxide Energizer 386/301 watch batteries were used to power the capsule, which typically last one hour. The batteries and electronics were incorporated into a 3D-printed capsule as shown in Fig. 4(e).

The capsule used here (Fig. 4(e)) is a scaled down version of the one first presented in [20]. It is approximately 1.4 times the length of commercial capsule endoscopes and 1.2 times the width, with a length of 42 mm and diameter of 13.5 mm, not including a 1 mm helical thread used for propulsion. For comparison, Fig. 4(e) shows our capsule with Given Imaging's colon capsule along with a U.S. quarter. The size is constrained by the batteries. With these components a 1.2-scaled capsule was originally designed, but our batteries' steel casings became magnetized in the rotating field and created an unmodeled disturbance resulting in poor pose estimation. As a result, we lengthened our capsule slightly to mitigate this problem. In the future, custom non-magnetic batteries could be utilized; commercial low-magnetic batteries do not meet both our size and power constraints [28].

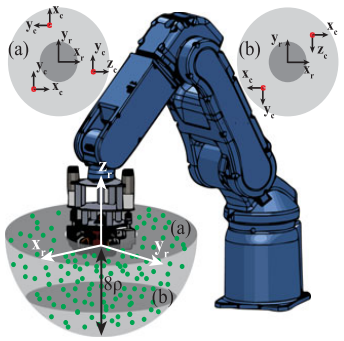

Fig. 5. Assuming the origin is located at the center of the external magnetic source, the workspace is restricted to a hemisphere in the negative $\mathbf{z}_r$ direction. Poses were randomly generated across the workspace, depicted by dots. The five initial states corresponding to the bottom rows of Table II are depicted in planes (a) and (b).

C. Sensor Calibration

Assuming the magnitude of the SAMM's dipole and each sensor's position offset is known, the sensitivities and orientations of the sensors were estimated using a constrained nonlinear least-squares algorithm to ensure accurate measurements. The sensor array was placed in the rigid test fixture (Fig. 3(b)) and the SAMM was moved relative to the capsule in a grid pattern (60 (w) × 60 (d) × 20 (h) mm^3) in 10 mm step increments, with the center of the grid 110 mm above the capsule; $\mathbf{m}_r$ was fixed throughout the test. A single dataset combined from two trials with dipole orientations of $[0\ 0\ 1]^T$ and $[0\ 0.707\ 0.707]^T$ was used. The sensitivity and orientation of each of the six sensors was solved simultaneously by estimating the readings using (2) and comparing them to the sensor measurements using the cost function $e = ||\mathbb{V}_m - \mathbb{V}_e||^2$. The comparisons were done in terms of the voltage output of the sensor because the sensitivity constant (α) that converts volts to mT was unknown. $\mathbb{V}_m$ is an array of voltage readings from the six sensors, and $\mathbb{V}_e = \mathbb{B}_e\alpha$. A total of 24 parameters were estimated: the fixed 6-DOF pose of the capsule, and three parameters for each of the sensors (the 2-DOF pointing orientation $\mathbf{s}$, and the scalar sensitivity α).

To evaluate the results of our sensor calibration, we compared the localization results using both the original nominal sensor values and the calibrated values across 210 tests with $||\mathbf{p}_c||$ spread evenly between 4ρ, 6ρ, and 7ρ. The nominal values (before calibration) resulted in a mean error of 4.9 mm and 7.8°, and a maximum error of 10.0 mm and 12.6°. The mean error using the calibrated values was reduced to 4.1 mm and 3.0° with the maximum error reduced to 8.6 mm and 6.2°.

IV. Characterization Using Simulations

Initial testing of the localization method was performed with a MATLAB simulation based on our experimental hardware, as depicted in Fig. 5. The origin of the SAMM's magnet was centered on the top surface of the workspace, whose plane lies orthogonal to the $\mathbf{z}_r$ axis. A spherical workspace was chosen to

TABLE I
COMPONENTS WHERE NOISE AND UNCERTAINTY WERE ADDED TO IMITATE EXPERIMENTALLY MEASURED RESULTS

Source of error	range
Sensor noise	$\pm$0.114 mT
Time difference between sensor and dipole readings	$\pm$2 ms
Capsule position uncertainty	1.5 mm
Capsule orientation uncertainty	3°
Dipole position uncertainty	0.5 mm
Dipole orientation uncertainty	2.4°
Dipole magnitude uncertainty	$\pm$5%

test positions uniformly; it can be reduced to a hemisphere in our application of capsule endoscopy because the capsule will reside in the human body, whose local tangent plane can be drawn to cut the spherical workspace in half. Due to hardware constraints, the capsule cannot be closer than 3ρ to the center of the SAMM's magnet, so the hemisphere shape is further reduced to a spherical shell that spans from 3ρ to 8ρ as shown in Fig. 5. Each of the tested 6-DOF poses were randomly generated from the workspace.

In ideal conditions, if no noise or uncertainty is modeled, the algorithm estimates the capsule's pose with only rounding error in both the position (4.6×10^{-14} mm) and orientation (3.4×10^{-14} °), across 100 random poses. However, the sensor array and the dipole field have uncertainties, and signals are noisy, so a more realistic simulation was conducted where noise and uncertainties were added. These sources, which were derived from our experimental hardware, are listed along with their ranges in Table I. Note the sensor noise remains constant, so as $||\mathbf{p}_c||$ increases, the magnitude of the external field and the signal-to-noise ratio decrease, resulting in worse localization. The position and orientation uncertainty, both for the capsule and dipole source, stem from how accurately our ground truth is known. The time difference is a result of our time resolution. Including the noise and uncertainty resulted in an error of 2.2$\pm$ 0.8 mm and $1.7° \pm 0.9°$ across 100 random poses (throughout this paper all errors are reported as the mean $\pm$ standard deviation). The orientation error is in terms of the angle-axis representation.

A known limitation of iterative methods is their dependence on the initial condition; if it is not in close proximity to the global minimum (the true capsule pose) the method may converge to a local minimum and result in poor localization. We do not assume prior knowledge of the capsule's pose, so the initial guess was chosen directly below the SAMM centered vertically in the hemispherical workspace with an orientation matching the external magnetic source's frame. Across 1,000 random poses, 98.7% resulted in a average error of 2.3 ± 1.0 mm and $1.8° \pm 0.8°$. The remaining 1.3% converged to an incorrect local minimum, typically, a pose that mirrors the true capsule pose. To ensure safety, we desire an algorithm that always converges to the global minimum.

One option to overcome the problem of local minimums is using an additional algorithm to estimate an initial condition that will be in close proximity to the optimal pose [10], and our previous non-iterative algorithm could be used to provide an initial guess [18]. Another option is to choose multiple initial conditions spread throughout the workspace and select the one that results in the minimum norm in the residual error between the sensor measurements and their estimates. Because we have a known workspace, if the algorithm converges to a position outside of the workspace (e.g., $\mathbf{p}_c$ has a positive $\mathbf{z}$ component) it is not considered a failure; instead, the initial conditions are modified by adding randomly generated noise from a uniform distribution on the interval $\pm$70 mm to each position component and a rotation on the interval of $\pm 45°$ about a random axis and the algorithm is run again. If the algorithm converges to a position inside the workspace that is not within 10 mm of the true capsule pose, it is considered a failure. We found using five structured initial conditions was sufficient for 100% convergence across 10,000 random poses. The five initial conditions are split across two planes in the hemispherical workspace as shown in Fig. 5. Other tested initial configurations along with their convergence rate to the true capsule pose are shown in Table II. Converging outside of the workspace is extremely rare, it occurs less than 0.5% of the time, when using five initial conditions. If a larger workspace is used, additional initial states may be necessary.

TABLE II
PERCENT CONVERGENCE TO TRUE CAPSULE POSE USING VARIOUS INITIAL STATES WITH POSITION VECTOR $\mathbf{p}_c$ IN MM AND ORIENTATION ANGLE-AXIS $\mathbf{k}$ IN RAD

Initial State $\mathbf{p}_c$	Initial State $\mathbf{k}$	Tested poses	Convergence
$[0\ 0\ -140]^T$	$[0\ 0\ 0]^T$	1000	98.7%
$[-81\ -81\ -81]^T$	$[0\ 0\ 0]^T$	1000	99.4%
$[81\ 81\ -81]^T$	$[0\ 0\ \frac{\pi}{2}]^T$		
$[-81\ -81\ -81]^T$	$[0\ 0\ 0]^T$	1000	99.8%
$[110\ -30\ -81]^T$	$[\frac{\pi}{2}\ 0\ 0]^T$		
$[-30\ 110\ -81]^T$	$[0\ \frac{\pi}{2}\ 0]^T$		
$[-81\ -81\ -81]^T$	$[0\ 0\ 0]^T$	10000	99.9%
$[110\ -30\ -81]^T$	$[\frac{\pi}{2}\ 0\ 0]^T$		
$[-30\ 110\ -81]^T$	$[0\ \frac{\pi}{2}\ 0]^T$		
$[0\ 0\ -140]^T$	$[0\ 0\ \frac{\pi}{2}]^T$		
$[-99\ -99\ 0]^T$	$[0\ 0\ 0]^T$	10000	100%
$[135\ -36\ 0]^T$	$[0\ \frac{\pi}{2}\ 0]^T$		
$[-36\ 135\ 0]^T$	$[0\ 0\ \frac{\pi}{2}]^T$		
$[-81\ -81\ -81]^T$	$[0\ 0\ \pi]^T$		
$[81\ 81\ -81]^T$	$[\frac{\pi}{2}\ 0\ 0]^T$		

If there is prior knowledge of the capsule's pose, using a single initial condition that is within 5 cm and 90° was sufficient to converge to the capsule's true pose every time over 10,000 randomly chosen poses. When used for capsule endoscopy, the initial localization will have no prior information about the capsule, but for subsequent tracking, the position of the capsule will generally be in close proximity to the previous position. However, prior knowledge of the capsule's orientation will be much less certain, particularly considering the use of rotating fields. By reducing the bounds on the position to 3 cm, the orientation constraints could be relaxed to 180° and still converge to the true pose in 99.9% of cases across 10,000 randomly chosen poses.

V. EXPERIMENTAL RESULTS AND DISCUSSION

When localizing the capsule, there is a trade-off between accuracy and the time to collect the sensor data. Fig. 6 compares

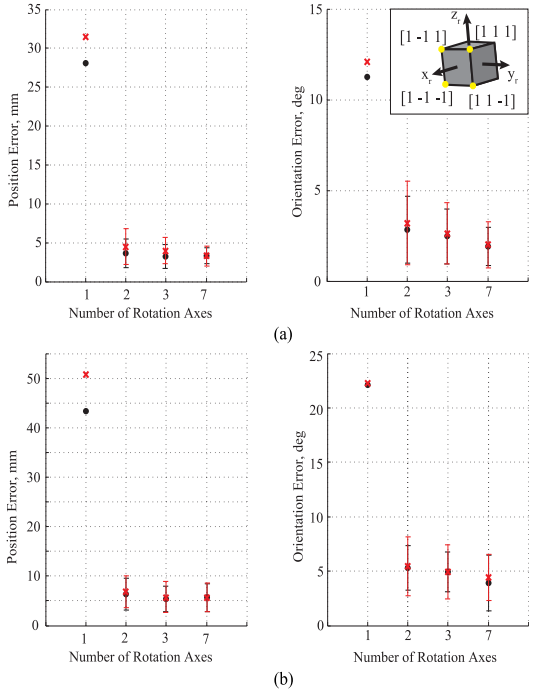

Fig. 6. Comparison of the effect of the angular velocity of the applied field and number of rotation axes on the accuracy of the localization. Data is represented as mean ± standard deviation over 70 trials for 2 Hz (black dot) and 3 Hz (red x). The standard deviation for one axis was too large to show graphically. (a) shows the results from a capsule rigidly mounted at 6ρ, and (b) show results for a capsule in step-out at 7ρ. The inset depicts the additional four axes used when testing seven rotation axes.

the average and standard deviation in error across different rotation speeds $||\boldsymbol{\Omega}||$ and number of rotation axes. Intuitively, the rotation speed of the dipole field should not substantially influence the accuracy of the localization if both data sets use the same number of complete dipole rotations and are below the Nyquist frequency such that no aliasing has occurred; our tests confirm this. The data sets in Fig. 6 each include 10 trials from seven positions, for a total of 70 trials. There is no appreciable difference between $||\boldsymbol{\Omega}|| = 2$ Hz or 3 Hz. Larger $||\boldsymbol{\Omega}||$ are recommended because the time required to collect the localization data is reduced.

Fig. 6 also shows the error when rotating the dipole field about one, two, three, or seven distinct rotation axes. One full rotation of data is collected about each axis. For one axis, Fig. 6 combines the data from all three coordinate axes $(\mathbf{x}_r, \mathbf{y}_r, \mathbf{z}_r)$ considered individually, and for two axes Fig. 6 combines the data across the three possible combinations of axes ($\mathbf{x}_r$ and $\mathbf{y}_r$, $\mathbf{x}_r$ and $\mathbf{z}_r$, $\mathbf{y}_r$ and $\mathbf{z}_r$) considered individually. The additional four axes chosen when rotating about seven axes are shown in the inset of Fig. 6. Rotating about two axes provides a significant advantage over one; an increasingly diminishing return in accuracy results when adding additional rotation axes. When the capsule is rigidly mounted (Fig. 6(a)), there is a 12% reduction in position error when using three axes instead of two; the error is reduced an additional 8% between three and seven axes, but the time to collect the data more than doubles. A capsule in the step-out regime (Fig. 6(b)) has a larger disparity, with a 15% reduction in position error between two and three axes and less than 1% additional reduction when increasing to seven axes. For the remainder of this paper we chose to rotate about the *three* robot-frame coordinate axes as it provides a good balance between speed and accuracy. For more time-sensitive applications, rotating the external field about a set of any two orthogonal axes will provide similar results.

Next, we tested whether collecting more data about each of the three rotation axes $(\mathbf{x}_r, \mathbf{y}_r, \mathbf{z}_r)$ would provide a more accurate pose estimate. Table III shows that using more than one rotation about each of the three orthogonal axes leads to negligible improvement in accuracy. This is true both when the capsule is held stationary and when it is free to rotate in the step-out regime.

Table IV shows the localization error with distances varying from 4ρ to 8ρ, which in our setup is approximately 100–200 mm. All reported errors used one rotation of the dipole field at 3 Hz about each of the three robot-frame coordinate axes. As expected, the error increases as the distance increases. In our setup, there are six signal-to-noise ratios, one for each sensor, at 8ρ all have fallen below 10:1. This results in large increases to the variance of the position errors in certain directions (011, 111, 101, 100; see Fig. 3(c)), which implies these regions are more sensitive to noise and uncertainty. Actuating and localizing near

TABLE III
COMPARISON OF ERROR (MEAN ± STANDARD DEVIATION OVER 70 TRIALS) FOR ONE AND FIVE ROTATIONS ABOUT $\mathbf{x}_r$, $\mathbf{y}_r$, AND $\mathbf{z}_r$

	Rotations	
Pose	1	5
Rigid, 6ρ	4.0 ± 1.7 mm, $2.6 \pm 1.2°$	3.9 ± 1.7 mm, $2.6 \pm 1.2°$
Step-out, 7ρ	5.7 ± 3.0 mm, $4.9 \pm 2.4°$	5.6 ± 2.9 mm, $4.7 \pm 2.4°$

TABLE IV
POSITION (MM) AND ORIENTATION ERROR (MEAN ± STANDARD DEVIATION OVER 10 TRIALS) OF CAPSULES RIGIDLY MOUNTED (4ρ TO 8ρ) AND IN STEP-OUT (7ρ). DATA COLLECTED BY ROTATING THE EXTERNAL FIELD ONCE AROUND EACH OF THREE ORTHOGONAL AXES AT 3 HZ. SEE FIG. 3(C) FOR LOCATION DEFINITIONS

Rigid?	Y	Y	Y	N	Y
Location	4ρ	6ρ	7ρ	7ρ	8ρ
001	2.8 ± 0.4	2.8 ± 0.7	4.9 ± 1.3	4.5 ± 1.6	4.0 ± 1.0
	$2.7° \pm 0.6°$	$3.4° \pm 0.8°$	$2.4° \pm 0.8°$	$4.3° \pm 0.8°$	$2.9° \pm 1.0°$
011	4.2 ± 2.0	4.1 ± 1.6	5.6 ± 1.9	4.9 ± 1.7	8.1 ± 3.4
	$2.8° \pm 1.9°$	$1.7° \pm 0.3°$	$2.1° \pm 0.8°$	$6.6° \pm 2.0°$	$2.4° \pm 1.2°$
111	4.0 ± 0.9	3.4 ± 1.4	5.5 ± 1.8	11.5 ± 1.8	4.6 ± 2.4
	$4.2° \pm 0.3°$	$2.1° \pm 0.9°$	$4.0° \pm 0.9°$	$6.3° \pm 1.0°$	$2.0° \pm 1.0°$
101	3.6 ± 1.0	5.9 ± 1.4	6.1 ± 0.8	6.8 ± 2.3	7.6 ± 2.5
	$3.5° \pm 0.7°$	$1.9° \pm 0.6°$	$3.0° \pm 0.6°$	$6.3° \pm 1.0°$	$2.8° \pm 1.3°$
100	2.8 ± 1.2	4.9 ± 1.6	4.7 ± 2.5	3.5 ± 1.6	11.7 ± 3.8
	$3.4° \pm 0.6°$	$2.9° \pm 0.8°$	$3.1° \pm 0.7°$	$1.6° \pm 0.9°$	$4.6° \pm 1.4°$
110	3.5 ± 0.6	4.3 ± 0.9	6.8 ± 1.4	4.5 ± 1.4	7.0 ± 1.3
	$1.8° \pm 0.4°$	$1.7° \pm 0.4°$	$2.0° \pm 1.4°$	$7.2° \pm 0.3°$	$2.1° \pm 0.8°$
010	2.3 ± 0.6	2.4 ± 1.2	3.5 ± 1.3	3.9 ± 1.0	3.1 ± 0.9
	$5.5° \pm 0.6°$	$4.8° \pm 0.4°$	$3.5° \pm 0.9°$	$1.9° \pm 1.0°$	$3.4° \pm 0.5°$

the "radial" positions of (001, 010) is recommended because these have the lowest mean error, and the control authority of the desired rotation axis is the most robust to localization errors [29]. According to the simulation, the algorithm should perform equally well across the entire workspace; the differences we see experimentally across locations are likely due to environmental factors such as unmodeled magnetic disturbances.

For comparison, results from both a rigidly fixed capsule and one that was free to rotate during the test are provided in Table IV for 7ρ. The position error when the capsule is free to rotate is comparable to that when it is held rigid. This is expected as the field is rotating above the step-out frequency such that the capsule has little net motion in these tests. The notable exception is in direction 111. It is unclear why this location performs consistently worse in the step-out regime than when rigidly fixed. The rigidly held capsules, which do not rely on battery power, give the best-case results. In an attempt to further isolate the batteries from the sensor array by lengthening the capsule by 4 mm, the error at 111 was cut almost in half, to 6.4 ± 1.0 mm. The remaining locations are already consistent with the rigidly fixed capsules.

The orientation error reported in Table IV is half of what we reported in our preliminary presentation of this method [19]. Subsequent to that publication, we performed additional calibration on the sensor array and SAMM device and were able to more accurately estimate the capsule's orientation during testing. As expected, the orientation error of the capsule in step-out is worse than when rigidly held because its orientation is not as accurately known and it changes slightly throughout the data collection as it wiggles back and forth in the rotating field.

VI. Demonstration of Capsule Propulsion

A proof-of-concept propulsion system was designed that utilizes the estimated pose from our localization method to propel a magnetic capsule through both straight and curved lumens using a single rotating dipole source for both propulsion and localization. Although in the current form these are decoupled such that the capsule's movement is periodically paused to re-localize, this provides the first step toward utilizing rotating magnetic fields in a more clinically realistic fashion. The demonstrations confirm that our localization method provides sufficient accuracy for propulsion using rotating dipole fields; all prior work from our group relied on cameras for position feedback [6].

From [30], if a dipole source is rotated about an axis $\hat{\mathbf{\Omega}}$, such that its magnetic moment is always orthogonal to the rotation axis, the applied field at any position in space rotates orthogonal to some constant axis $\hat{\boldsymbol{\omega}}_c$. Assuming a screw-type capsule is constrained to a lumen, at the capsule's position, we desire $\hat{\boldsymbol{\omega}}_c$ to be aligned with the lumen (and the capsule's principle axis $\mathbf{x}_c$) to provide a useful magnetic torque. Given the capsule's pose from our localization method, we calculate the actuator magnet's desired rotation axis, from [6]:

$$\hat{\mathbf{\Omega}} = \widehat{\mathbf{B}\hat{\boldsymbol{\omega}}_c} \tag{4}$$

where $\mathbf{B}$ is from (1). Prior to propulsion the capsule must be localized. We assume the capsule is placed within our known workspace (in capsule endoscopy this would be the abdomen); no additional information about the pose is required. In our experimental demonstrations, the SAMM was started in an arbitrary position above the approximate center of the workspace. The first localization used five initial guesses as described in Section IV. For the remainder of the trajectory, the previously estimated pose was used as the initial condition for the iterative algorithm. During the propulsion phase, we assume the capsule's position and heading remain constant. Prior to collecting a batch of localization data, the SAMM was raised 50 mm in the vertical direction to ensure the capsule would be in the step-out regime. This additional movement of the SAMM is not necessary for our algorithm; it was required due to our hardware's limited $||\mathbf{\Omega}||$. Approximately one rotation about each of the $\mathbf{x}_r$, $\mathbf{y}_r$, and $\mathbf{z}_r$ axes in the SAMM's coordinate frame was collected. After each localization, the SAMM's pose was updated based on the capsule's estimated state before resuming propulsion. A block diagram of the propulsion system is depicted in Fig. 7.

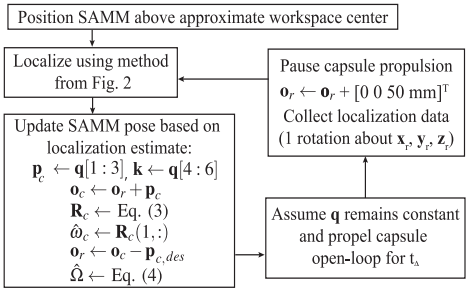

Fig. 7. A block diagram of the system used to propel the capsule through the two lumen trajectories. $\mathbf{q}$ is the capsule's state, $\hat{\boldsymbol{\omega}}$ is the SAMM's desired rotation axis, $\hat{\boldsymbol{\omega}}_c$ is the heading of the capsule, $\mathbf{p}_{c,\,des}$ is the desired position of the capsule ($\mathbf{o}_c$) relative to the SAMM ($\mathbf{o}_r$) for propulsion, and t_Δ is the time interval between localizations. Note $\mathbf{p}_{c,\,des}$ may be user-specified or the result of an optimization routine.

When propelling the capsule through the straight lumen (Fig. 8(a)), a configuration where the external magnet leads the capsule was chosen because in these positions the attractive magnetic force combines with the magnetic torque to result in faster capsule propulsion than in "radial" positions [6]. It took two minutes for the capsule to traverse the straight path with an average forward velocity of 2.1 mm/s. Using the same propulsion system, the capsule was also propelled through a semi-circular trajectory shown by the composite image in Fig. 8(b). For this path, an arbitrary relative position was chosen to ensure our method can be generalized to any position. It took approximately 6.5 minutes to complete the trajectory, with an average speed of 1.4 mm/s. It should be noted that neither the actuation configuration and parameters during the propulsion phase nor the time between localizations have been optimized in these demonstrations so it should not be assumed that we have achieved maximum average speed. Additionally, the plastic tubing does not accurately model intestine properties so these velocities should not be assumed to be clinically realistic.

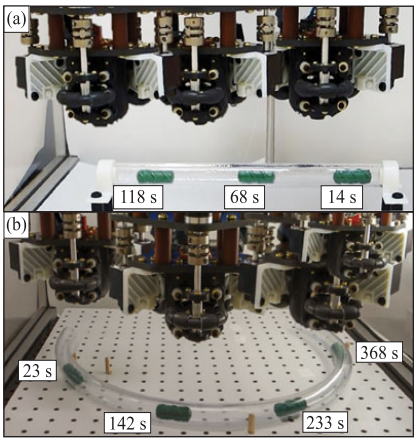

Fig. 8. Experimental demonstration of capsule propulsion using the system described in Fig. 7. (a) The SAMM was placed in a leading configuration with $\mathbf{p}_{c,\,des} = [0\ 58\ -100]^T$ mm and $||\mathbf{\Omega}|| = 0.5$ Hz during propulsion. (b) The SAMM was placed in an arbitrary configuration with $\mathbf{p}_{c,\,des}$ a function of the capsule's heading such that the SAMM's relative placement to the capsule remains constant regardless of the capsule's heading with $||\mathbf{p}_{c,\,des}|| = 100$ mm and $||\mathbf{\Omega}|| = 0.5$ Hz during propulsion. The capsule's propulsion was periodically paused for localization with $t_\Delta = 12$ sec in (a) and $t_\Delta = 15$ sec in (b). Please see supplementary video.

VII. Conclusion

We have described and characterized a magnetic-localization method that enables a screw-type magnetic capsule, equipped with an embedded permanent magnet and Hall-effect sensors, to be localized using a rotating magnetic-dipole field. We showed the localization method provided accurate pose estimation to within a few millimeters in position and a few degrees in orientation throughout a usable workspace. This localization method was developed as a complement to methods previously developed to propel a screw-type magnetic capsule using a single rotating magnetic dipole. We experimentally demonstrated that the localization is sufficiently accurate to enable the use of our propulsion method with no other form of localization. The target application of this technology is active capsule endoscopy of the small intestines, with potential for use in the colon as well.

References

[1] P. R. Slawinski, K. L. Obstein, and P. Valdastri, "Emerging issues and future developments in capsule endoscopy, " *Techn. Gastrointestinal Endo*, vol. 17, no. 1, pp. 40–46, 2015.

[2] Z. Liao *et al.*, "Feasibility and safety of magnetic-controlled capsule endoscopy system in examination of human stomach: A pilot study in healthy volunteers, " *J. Interventional Gastroenterol.*, vol. 2, no. 4, pp. 155–160, 2012.

[3] X. Wang and M.-H. Meng, "Computational aspects in actuation and guidance mechanism for wireless active capsule endoscope, " in *Proc. IEEE Int. Conf. Intel. Robots Syst.*, 2008, pp. 1198–1203.

[4] G. Ciuti, P. Valdastri, A. Menciassi, and P. Dario, "Robotic magnetic steering and locomotion of capsule endoscope for diagnostic and surgical endoluminal procedures, " *Robotica*, vol. 28, pp. 199–207, 2010.

[5] F. Carpi, N. Kastelein, M. Talcott, and C. Pappone, "Magnetically controllable gastrointestinal steering of video capsules, " *IEEE Trans. Biomed. Eng.*, vol. 58, no. 2, pp. 231–234, Feb. 2011.

[6] A. W. Mahoney and J. J. Abbott, "Generating rotating magnetic fields with a single permanent magnet for propulsion of untethered magnetic devices in a lumen, " *IEEE Trans. Robot.*, vol. 30, no. 2, pp. 411–420, Apr. 2014.

[7] J. Kim, Y. Kwon, and Y. Hong, "Automated alignment of rotating magnetic field for inducing a continuous spiral motion on a capsule endoscope with a twistable thread mechanism, " *Int. J. Precision Eng. Manuf.*, vol. 13, no. 3, pp. 371–377, 2012.

[8] S. Song *et al.*, "6-d magnetic localization and orientation method for an annular magnet based on a closed-form analytical model, " *IEEE Trans. Mag.*, vol. 50, no. 9, Sep. 2014, Art. no. 5000411.

[9] D. M. Pham and S. Aziz, "A real-time localization system for an endoscopic capsule, " in *Proc. IEEE 9th Int. Conf. Intell. Sens., Sens. Netw. Inf. Process.*, 2014, pp. 1–6.

[10] C. Hu, M. Li, S. Song, W. Yang, R. Zhang, and M. Q.-H. Meng, "A cubic 3-axis magnetic sensor array for wirelessly tracking magnet position and orientation, " *IEEE Sensors J.*, vol. 10, no. 5, pp. 903–913, May 2010.

[11] W. Weitschies, H. Blume, and H. Monnikes, "Magnetic marker monitoring: High resolution real-time tracking of oral solid dosage forms in the gastrointestinal tract, " *Eur. J. Pharmaceutics Biopharmaceutics*, vol. 74, no. 1, pp. 93–101, 2010.

[12] M. Salerno, F. Mulana, R. Rizzo, A. Landi, and A. Menciassi, "Magnetic and inertial sensor fusion for the localization of endoluminal diagnostic devices, " *Int. J. Comput. Assisted Radiol. Surgery*, vol. 7, no. S1, pp. 229–235, 2012.

[13] C. D. Natali, M. Beccani, N. Simaan, and P. Valdastri, "Jacobian-based iterative method for magnetic localization in robotic capsule endoscopy, " *IEEE Trans. Robot.*, vol. 32, no. 2, pp. 327–338, Apr. 2016.

[14] M. Kim, Y. Hong, and E. Lim, "Position and orientation detection of capsule endoscopes in spiral motion, " *Int. J. Precision Eng. Manuf.*, vol. 11, no. 1, pp. 31–37, 2010.

[15] M. Salerno *et al.*, "A discrete-time localization method for capsule endoscopy based on on-board magnetic sensing, " *Meas. Sci. Technol.*, vol. 23, no. 1, 2012, Art. no. 015701.

[16] D. Son, S. Yim, and M. Sitti, "A 5-d localization method for a magnetically manipulated untethered robot using a 2-d array of hall-effect sensors, " *IEEE/ASME Trans. Mechatronics*, vol. 21, no. 2, pp. 708–716, Apr. 2016.

[17] S. Yim and M. Sitti, "3-d localization method for a magnetically actuated soft capsule endoscope and its applications, " *IEEE Trans. Robot.*, vol. 29, no. 5, pp. 1139–1151, Oct. 2013.

[18] K. M. Popek, A. W. Mahoney, and J. J. Abbott, "Localization method for a magnetic capsule endoscope propelled by a rotating magnetic dipole field, " in *Proc. IEEE Int. Conf. Robot. Autom.*, 2013, pp. 5328–5333.

[19] K. M. Popek and J. J. Abbott, "6-d localization of a magnetic capsule endoscope using a stationary rotating magnetic dipole field, " in *Proc. Hamlyn Symp. Med. Robot.*, 2015, pp. 47–48.

[20] K. M. Miller, A. W. Mahoney, T. Schmid, and J. J. Abbott, "Proprioceptive magnetic-field sensing for closed-loop control of magnetic capsule endoscopes, " in *Proc. IEEE Int. Conf. Intel. Robots Syst.*, 2012, pp. 1994–1999.

[21] E. P. Furlani, *Permanent Magnet and Electromechanical Devices: Materials, Analysis, and Applications*, 1st ed. San Diego, CA, USA: Academic Press, 2001.

[22] A. J. Petruska and J. J. Abbott, "Optimal permanent-magnet geometries for dipole field approximation, " *IEEE Trans. Mag.*, vol. 49, no. 2, pp. 811–819, Feb. 2013.

[23] R. M. Murray, Z. Li, and S. S. Sastry, *A Mathematical Introduction to Robotic Manipulation*. Boca Raton, FL, USA: CRC Press, 1994.

[24] J. Nocedal and S. J. Wright, *Numerical Optimization*, 2nd ed.New York, NY, USA: Springer, 2006.

[25] G. Guennebaud *et al.*, "Eigen v3, " 2010. [Online]. Available: http://eigen.tuxfamily.org

[26] S. E. Wright, A. W. Mahoney, K. M. Popek, and J. J. Abbott, "A spherical-magnet end-effector for robotic magnetic manipulation, " in *Proc. IEEE Int. Conf. Robot. Autom.*, 2015, pp. 1190–1195.

[27] A. J. Petruska and J. J. Abbott, "Omnimagnet: An omnidirectional electromagnet for controlled dipole-field generation, " *IEEE Trans. Magn.*, vol. 50, no. 7, Jul. 2014, Art. no. 8400810.

[28] *CR1130*, Powerstream. 2016. [Online]. Available: http://www.powerstream.com

[29] A. W. Mahoney and J. J. Abbott, "Control of untethered magnetically actuated tools with localization uncertainty using a rotating permanent magnet, " in *Proc. IEEE Int. Conf. Biomed. Robot. Biomechatronics*, 2012, pp. 1632–1637.

[30] E. Paperno, I. Sasada, and E. Leonovich, "A new method for magnetic position and orientation tracking, " *IEEE Trans. Magn.*, vol. 37, no. 4, pp. 1938–1940, Aug. 2001.

3.9 Errata

Table 3.5. Table 3.2 Reprinted With Correct Formatting. Shows the Percent Convergence to True Capsule Pose Using Various Initial States With Position Vector $\mathbf{p}_c$ in mm and Orientation Angle-Axis $\mathbf{k}$ in rad.

Initial State $\mathbf{p}_c$	Initial State $\mathbf{k}$	Tested poses	Convergence
$[0\ 0\ -140]^T$	$[0\ 0\ 0]^T$	1000	98.7%
$[-81\ -81\ -81]^T$ $[81\ 81\ -81]^T$	$[0\ 0\ 0]^T$ $[0\ 0\ \frac{\pi}{2}]^T$	1000	99.4%
$[-81\ -81\ -81]^T$ $[110\ -30\ -81]^T$ $[-30\ 110\ -81]^T$	$[0\ 0\ 0]^T$ $[\frac{\pi}{2}\ 0\ 0]^T$ $[0\ \frac{\pi}{2}\ 0]^T$	1000	99.8%
$[-81\ -81\ -81]^T$ $[110\ -30\ -81]^T$ $[-30\ 110\ -81]^T$ $[0\ 0\ -140]^T$	$[0\ 0\ 0]^T$ $[\frac{\pi}{2}\ 0\ 0]^T$ $[0\ \frac{\pi}{2}\ 0]^T$ $[0\ 0\ \frac{\pi}{2}]^T$	10000	99.9%
$[-99\ -99\ 0]^T$ $[135\ -36\ 0]^T$ $[-36\ 135\ 0]^T$ $[-81\ -81\ -81]^T$ $[81\ 81\ -81]^T$	$[0\ 0\ 0]^T$ $[0\ \frac{\pi}{2}\ 0]^T$ $[0\ 0\ \frac{\pi}{2}]^T$ $[0\ 0\ \pi]^T$ $[\frac{\pi}{2}\ 0\ 0]^T$	10000	100%

CHAPTER 4

SIMULTANEOUS LOCALIZATION AND PROPULSION OF A MAGNETIC CAPSULE IN A LUMEN USING A SINGLE ROTATING MAGNET

Prior work utilizing rotating magnetic fields for active capsule endoscopy required the localization and propulsion to be decoupled (i.e., not simultaneous). This chapter details a localization method that can estimate the full 6-DOF capsule pose while it is synchronously rotating with the applied field. It presents a complete localization and closed-loop propulsion system that manipulates the actuator magnet's position and rotation speed to maximize the capsule's forward velocity. The method relies on the results in Chapter 3 for the initial localization, and the experimental results utilized the SAMM device described in Chapter 2. The ability to simultaneously localize and propel the capsule results in three times faster propulsion speeds compared to the decoupled propulsion and localization system described in Chapter 3. I am responsible for the bulk of this work while being advised by Dr. Tucker Hermans and Dr. Jake Abbott. Arthur Mahoney's contribution resulted in Section 5.1 and Appendix B.

4.1 Introduction

Wireless capsule endoscopes, propelled by magnetic fields, promise a low-cost, minimally invasive method to view the entire gastrointestinal tract [1]. A small permanent magnet is embedded inside the capsule, and all power needed to propel the device is obtained from an externally applied magnetic field. Actuation methods typically either use magnetic force for dragging or pulling [2, 3, 4], or magnetic torque for screw-like propulsion of a capsule with a helical thread [5, 6, 7, 8].

One benefit of using magnetic fields for propulsion of capsule endoscopes is the opportunity for concurrent localization using the same magnetic field. There are several magnetic-localization methods previously published; see [9] for a review. We focus our

discussion on those using *rotating* magnetic fields, as they are compatible with our chosen propulsion method [10]. Their time-varying nature also provides a constant influx of new information to the system, preventing the need for additional sensors (e.g., an accelerometer in the capsule). Prior localization methods typically assume the capsule has no net motion during localization [11, 12], which prevents continuous propulsion. Kim *et al.* developed an algorithm to localize a capsule as it rotates with the applied field [13], but found in practice the capsule needed to be stationary to meet their desired performance [5]. Son *et al.* describe a five-degree-of-freedom (5-DOF) localization algorithm using externally placed sensors to estimate the capsule's pose by measuring the field of the capsule's embedded permanent magnet [14], however, a full 6-DOF estimate is preferable to optimize control of the capsule.

Prior work utilizing magnetic fields for on-line closed-loop control of capsule endoscopes has focused on dragging the capsule with magnetic forces [2, 3, 4]. Salerno *et al.* developed a 2-DOF control system to measure forces during dragging tasks [3]. Taddese *et al.* experimentally demonstrated 4-DOF closed-loop control of a tethered magnetic capsule using magnetic field gradients [2]. Closed-loop propulsion with rotating fields previously either utilized computer vision for localization [10], which is not practical for clinical use, or required decoupled (i.e., not simultaneous) localization and propulsion [5, 12].

Recently, we presented the first demonstration of simultaneous localization and propulsion of a screw-type magnetic capsule using a single external magnetic dipole (which we will refer to as the "actuator magnet" herein) to generate the applied rotating magnetic field [15]. The magnetic localization method used an extended Kalman filter (EKF) to estimate the full 6-DOF capsule pose as it continuously rotates with the applied field. In this chapter, we present an extended treatment of the method introduced in [15], but with a number of improvements. We compare the EKF's performance, which is a first-order approximation, with the Square-root Unscented Kalman filter (SRUKF), which can approximate higher-order nonlinearities, and we find the SRUKF outperforms the EKF. Both nonlinear Kalman filters use a simplified 2-DOF process model that assumes the capsule's movement is restricted to translation along and rotation about its principle axis. We restrict the remaining 4-DOF in the process model and let the lumen dictate changes in the capsule's heading. In this chapter, the Kalman filter's process model has been updated to

adapt based on the capsule's movement, improving the system's robustness and enabling the capsule to successfully traverse a highly heterogeneous environment (e.g., intestines). Finally, in our previous work the placement of the actuator magnet relative to the capsule was arbitrarily chosen. In this chapter, placement of the actuator magnet is optimized to maximize the forward velocity of the capsule, subject to constraints on the actuator magnet's position (e.g., to prevent collision with a patient or other obstacles in the actuator magnet's workspace). Although [16] considered optimizing the actuator magnet's position relative to the capsule to maximize forward velocity, they did not consider the speed of the applied rotating field, and the optimization was performed with a genetic algorithm prior to experiments. This results in a constant desired position offset that is used throughout their experiments, such that there is no ability to incorporate additional constraints or adjust the actuator magnet based on the capsule's current movement in the applied field.

This chapter provides a complete methodology to localize and propel a capsule in the small intestines. The ability to move rapidly through the small intestines will be a critical capability in any system designed to perform a complete scan of the gastrointestinal tract in a timely manner. This chapter is also the culmination of many efforts from our group in magnetic capsule endoscopy. The capsule is initially localized using the method of [12]. It is propelled using the method of [10], with the permanent-magnet robotic end-effector described in [17]. Finally, the capsule's movement in the applied field is constantly monitored (i.e., Is the capsule synchronously rotating with the field, is the capsule able to rotate but the field is rotating too quickly for the capsule to remain rotating synchronously, or is the capsule stuck?), using the method described in [18]. A block diagram depicting the full localization and propulsion system is shown in Fig. 4.1. Each component is labeled with its corresponding section.

4.2 Nomenclature

Throughout this chapter scalars are represented by italic lowercase font (e.g., s), vectors are denoted by lowercase bold font (e.g., ${}^{i}\mathbf{v}$) where the optional superscript i denotes a specific coordinate frame the vector is being expressed with respect to, and subscripts may also be used in the naming convention. The "hat" symbol (e.g., $\hat{\mathbf{v}}$) denotes a vector of unit length, and it can also represent the operation $\hat{\mathbf{v}} = \frac{\mathbf{v}}{\|\mathbf{v}\|}$. Matrices are represented by

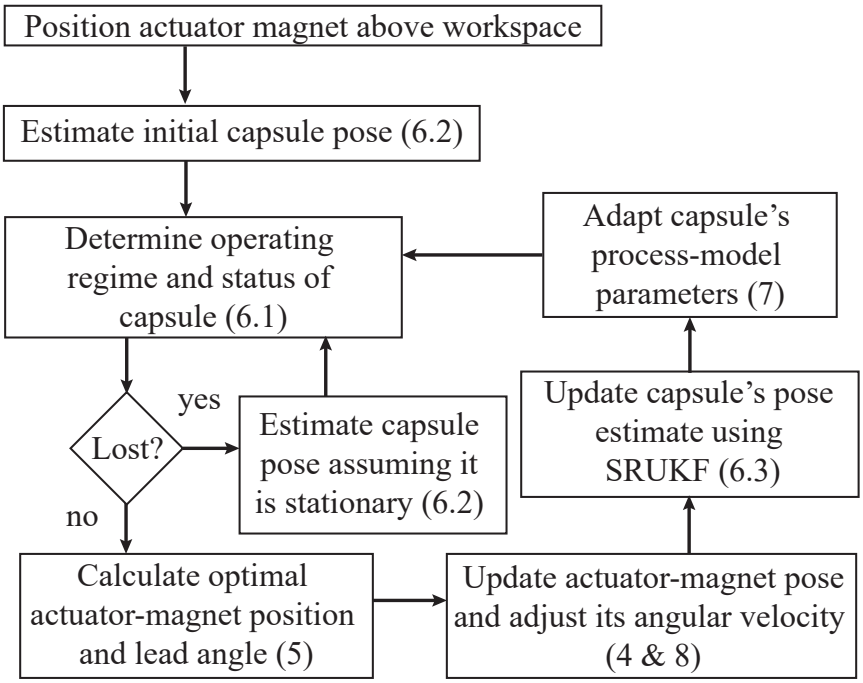

Figure 4.1. Block diagram depicting our localization and propulsion system. The numbers correspond to the section in which each component is described.

uppercase bold font; for rotation matrices ${}^{j}\mathbf{R}_{i}$ the subscript i and superscript j denote the starting and ending coordinate frames, respectively; this is also true for quaternions. $\mathbf{I}_{n}$ is an $n \times n$ identity matrix. $\mathbb{S}[\cdot]$ is the skew-symmetric matrix representation of the cross product operation (e.g., $\mathbb{S}[\mathbf{a}]\mathbf{b} = \mathbf{a} \times \mathbf{b}$). Units are shown by standard font in curly brackets (e.g., $\{\mathrm{m}\}$).

4.3 Actuation and Sensing System

We will briefly describe the actuation and sensing system because it influences our propulsion and localization methods discussed in subsequent sections. Our setup shown in Fig. 4.2 uses the Spherical-actuator-magnet Manipulator (SAMM) [17], mounted on a 6-DOF robotic arm, for the actuator magnet. The SAMM uses three mutually orthogonal omniwheels to generate singularity-free continuous rotation of its spherical permanent magnet about arbitrary axes. The field of a spherical permanent magnet is nearly perfectly approximated by the point-dipole model such that the applied field ${}^{r}\mathbf{b}_{c}\ \{\mathrm{T}\}$ at the location of the capsule's magnet can be calculated with [19]:

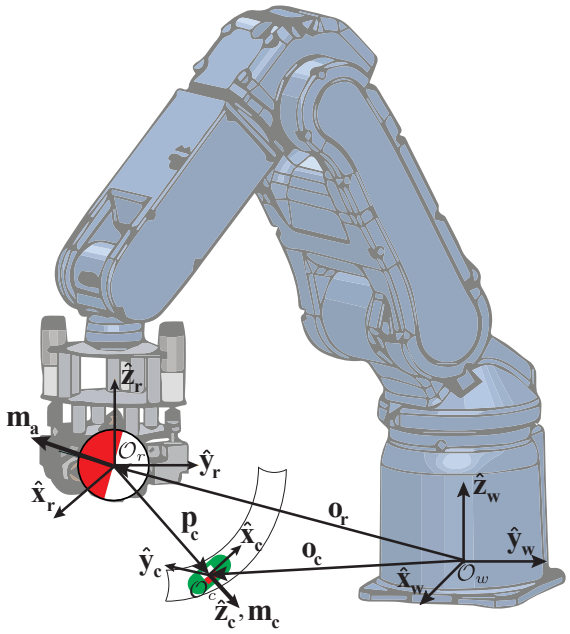

Figure 4.2. Overall system setup with the SAMM mounted as the end-effector of a robot arm. The capsule's coordinate frame origin $\mathcal{O}_c$ is placed at the center of its internal magnet, the robot's tool frame origin $\mathcal{O}_r$ resides at the center of the actuator magnet, and $\mathbf{o}_c$ and $\mathbf{o}_r$ are the respective position offset vectors relative to a static world frame origin $\mathcal{O}_w$ placed at the base of the robot. We enforce that the robot and world frames are aligned (i.e., ${}^{w}\mathbf{R}_r = \mathbf{I}_3$).

$$ {}^{r}\mathbf{b}_c = \frac{\mu_0}{4\pi||{}^{r}\mathbf{p}_c||^3}\mathbf{B}_c\,{}^{r}\mathbf{m}_a \tag{4.1} $$

$$ \mathbf{B}_c = 3\,{}^{r}\hat{\mathbf{p}}_c\,{}^{r}\hat{\mathbf{p}}_c^{\mathsf{T}} - \mathbf{I}_3 \tag{4.2} $$

where $\mu_0 = 4\pi \times 10^{-7}\,\{\mathrm{N{\cdot}A^{-2}}\}$ is the permeability of free space, $\mathbf{m}_a\,\{\mathrm{A{\cdot}m^2}\}$ is the magnetic moment of the SAMM's actuator magnet, and ${}^{r}\mathbf{p}_c\,\{\mathrm{m}\}$ is the position of the capsule relative to the robot's tool frame, expressed with respect to the robot tool frame (see Fig. 4.2). Note that $\mathbf{p}_c$ is frame invariant and can be expressed with respect to any desired frame. Although we utilize the SAMM exclusively in this dissertation, the methods presented here generalize to other magnetic-dipole sources as well (e.g., Omnimagnets [20, 21]).

There are six Hall-effect sensors rigidly placed inside the capsule, surrounding its internal magnet but minimally effected by its field, as described in [12]. The position offset ${}^{c}\boldsymbol{\delta}_i\,\{\mathrm{m}\}$ of sensor i from the center of the capsule's magnet along with the orientation of the sensor's measuring axis ${}^{c}\hat{\boldsymbol{\beta}}_i$ are known and remain constant. The position vector to the

i^{th} sensor from the robot's tool frame is calculated as

$$ {}^{r}\mathbf{p}_i = {}^{r}\mathbf{p}_c + {}^{r}\mathcal{Q}_c^{c}\boldsymbol{\delta}_i{}^{r}\mathcal{Q}_c^{*} \tag{4.3} $$

where ${}^{r}\mathcal{Q}_c$ is the quaternion representation of the rotation matrix ${}^{r}\mathbf{R}_c$ (see Appendix A). The scalar measurement of sensor i is the projection of the field onto the sensor's measuring axis:

$$ b_i = \frac{\mu_0}{4\pi||{}^{r}\mathbf{p}_i||^3}{}^{c}\hat{\boldsymbol{\beta}}_i^{\mathsf{T}}{}^{r}\mathcal{Q}_c^{*}\left(\mathbf{B}_i{}^{r}\mathbf{m}_a\right){}^{r}\mathcal{Q}_c \tag{4.4} $$

where $\mathbf{B}_i$ is calculated with (4.2), utilizing (4.3).

4.4 Propulsion

We summarize the method of [10]. If a magnetic field $\mathbf{b}_c$ is applied by the actuator magnet on the capsule's magnetic dipole moment $\mathbf{m}_c$ $\{\text{A}\cdot\text{m}^2\}$, then a magnetic torque $\boldsymbol{\tau}$ $\{\text{N}\cdot\text{m}\}$ and force $\mathbf{f}$ $\{\text{N}\}$ are generated on the capsule:

$$ \begin{aligned} {}^{r}\boldsymbol{\tau} &= {}^{r}\mathbf{m}_c \times {}^{r}\mathbf{b}_c = -{}^{r}\mathbf{b}_c \times {}^{r}\mathbf{m}_c \\ &= \gamma_1 \mathbb{S}[\mathbf{B}_c^{r}\hat{\mathbf{m}}_a]^{\mathsf{T}}{}^{r}\hat{\mathbf{m}}_c = \gamma_1 \mathbf{T}^{r}\hat{\mathbf{m}}_c \end{aligned} \tag{4.5} $$

$$ \begin{aligned} {}^{r}\mathbf{f} &= ({}^{r}\mathbf{m}_c \cdot \nabla){}^{r}\mathbf{b}_c \\ &= \gamma_2 \left({}^{r}\hat{\mathbf{m}}_a{}^{r}\hat{\mathbf{p}}_c^{\mathsf{T}} + \left({}^{r}\hat{\mathbf{m}}_a^{\mathsf{T}}{}^{r}\hat{\mathbf{p}}_c \right) \mathbf{I}_3 + {}^{r}\hat{\mathbf{p}}_c{}^{r}\hat{\mathbf{m}}_a^{\mathsf{T}}\mathbf{Z} \right) {}^{r}\hat{\mathbf{m}}_c \\ &= \gamma_2 \mathbf{F}^{r}\hat{\mathbf{m}}_c \end{aligned} \tag{4.6} $$

where $\mathbf{Z}$ and the scalar constants are defined as:

$$ \mathbf{Z} = \mathbf{I}_3 - 5{}^{r}\hat{\mathbf{p}}_c{}^{r}\hat{\mathbf{p}}_c^{\mathsf{T}} \tag{4.7} $$

$$ \gamma_1 = \frac{\mu_0 \|{}^{r}\mathbf{m}_a\| \|{}^{r}\mathbf{m}_c\|}{4\pi \|{}^{r}\mathbf{p}_c\|^3} \tag{4.8} $$

$$ \gamma_2 = \frac{3\mu_0 \|{}^{r}\mathbf{m}_a\| \|{}^{r}\mathbf{m}_c\|}{4\pi \|{}^{r}\mathbf{p}_c\|^4}. \tag{4.9} $$

Note that the magnetic torque scales as $\|\mathbf{p}_c\|^{-3}$ and the magnetic force scales as $\|\mathbf{p}_c\|^{-4}$.

The magnetic torque causes $\mathbf{m}_c$ to rotate in an attempt to align with $\mathbf{b}_c$. If the magnetic field $\mathbf{b}_c$ rotates continuously around an axis $\hat{\boldsymbol{\Omega}}_c$, then $\boldsymbol{\tau}$ will cause the capsule to continuously rotate, which is converted into screw propulsion via a helical thread. The rotation axis of the capsule's dipole moment, $\mathbf{m}_c$, tends to align with the field rotation axis $\hat{\boldsymbol{\Omega}}_c$ over time if possible.

If a dipole source $\mathbf{m}_a$ is rotated around some arbitrary axis $\hat{\boldsymbol{\Omega}}_a$ such that $\mathbf{m}_a^{\mathsf{T}}\hat{\boldsymbol{\Omega}}_a = 0$ is

always true, then at any point in space (e.g., the location of the capsule), the applied field rotates orthogonal to a local axis $\hat{\mathbf{\Omega}}_c$. Assuming the capsule is constrained to a lumen, the desired $\hat{\mathbf{\Omega}}_c$ is parallel to the capsule's principle axis $\hat{\mathbf{x}}_c$ and locally aligned with the lumen. Given some desired rotation axis $\hat{\mathbf{\Omega}}_c$ (based on the estimated capsule pose) the necessary actuator magnet rotation axis is calculated by:

$$^r\hat{\mathbf{\Omega}}_a = \widehat{\mathbf{B}_c {}^r\hat{\mathbf{\Omega}}_c} \tag{4.10}$$

where $\mathbf{B}_c$ is from (4.2). As $\mathbf{m}_a$ is rotated around $\hat{\mathbf{\Omega}}_a$, $\mathbf{b}_c$ rotates around $\hat{\mathbf{\Omega}}_c$, updated as in (4.1), with a magnitude that fluctuates elliptically as:

$$\|^r\mathbf{b}_c\| = \frac{\mu_0 \|^r\mathbf{m}_a\|}{4\pi \|^r\mathbf{p}_c\|^3} \sqrt{1 + 3(^r\hat{\mathbf{m}}_a^{\mathsf{T}} {}^r\hat{\mathbf{p}}_c)^2}. \tag{4.11}$$

4.5 Optimal Propulsion

The method reviewed in Section 4.4 provides the means to set $\hat{\mathbf{\Omega}}_a$, given some position offset between the capsule and the actuator magnet, and some desired $\hat{\mathbf{\Omega}}_c$. In this section, a constrained nonlinear optimization is performed to establish the position offset between the capsule and the actuator magnet, as well as the lead angle between the applied field $\mathbf{b}_c$ and the capsule's dipole $\mathbf{m}_c$, that results in the maximum capsule velocity.

We assume the rotation axis of the field at the capsule ($\hat{\mathbf{\Omega}}_c$) and the capsule's principle axis ($\hat{\mathbf{x}}_c$) are aligned for simplicity. For a capsule constrained in a lumen, the rotation axis of the field can be set using (4.10) to ensure this assumption is valid. When the applied magnetic field continuously rotates, the generated magnetic torque $\boldsymbol{\tau}$ tends to cause the capsule's dipole moment $\mathbf{m}_c$ to continuously attempt to align with the rotating field. Friction generated between the capsule and the lumen wall, however, impedes the alignment of $\mathbf{m}_c$ to the applied field. The resulting misalignment is measured by the angle α. We refer to α as the "lead angle." In physical systems with negligible inertia, the lead angle is largely a function of the strength of the capsule and actuator magnets' dipole moments, and in particular, the rotational friction that impedes the capsule's ability to align with the rotating magnetic field. In general, the lead angle can be controlled by varying the rotation frequency of the applied field: when the field rotates very slowly (i.e., quasistatically) the lead angle is small. The lead angle tends to increase as the field rotation frequency increases. If there is no magnetic force applied to the capsule, when the applied

magnetic field rotates at the device's step-out frequency (the maximum frequency where the device can remain synchronized with the rotating field), the lead angle is $\alpha = 90^\circ$.

4.5.1 Trade-Off Between Magnetic Force and Magnetic Torque

For every relative position $\mathbf{p}_c$, there exists a trade-off between the magnetic torque magnitude $\|\boldsymbol{\tau}\|$ and the magnetic force magnitude $\|\mathbf{f}\|$, which is determined by the lead angle α: when $\alpha = 0^\circ$ and the capsule dipole moment $\mathbf{m}_c$ is approximately aligned with the applied field $\mathbf{b}_c$, then $\|\boldsymbol{\tau}\|$ is minimized ($\|\boldsymbol{\tau}\| \approx 0$) and $\|\mathbf{f}\|$ is maximized. When $\alpha = 90^\circ$, then $\|\boldsymbol{\tau}\|$ is maximized and $\|\mathbf{f}\|$ is minimized. This is illustrated in Fig. 4.3.

Fig. 4.3(a) shows the maximum, minimum, and range of the magnetic force magnitude (normalized by $2\gamma_2$) for lead angles $\alpha = 0^\circ$ and $\alpha = 90^\circ$ over one actuator revolution plotted as a function of θ, which measures the angle between $\hat{\boldsymbol{\Omega}}_a$ and $\hat{\mathbf{p}}_c$. The maximum force magnitude occurs when $\alpha = 0^\circ$ and $\theta = 90^\circ$, which is a "radial" position in which $\hat{\mathbf{p}}_c$ is orthogonal to $\boldsymbol{\Omega}_c$ using the terminology of [10]. The minimum magnetic force magnitude is 0, and occurs when $\alpha = 90^\circ$ and $\theta = 0^\circ$ or $\theta = 180^\circ$. This effect was previously utilized to propel a magnetic helical swimmer away from a strong permanent actuator magnet in [22]. Note that the maximum magnetic force magnitude when $\alpha = 90^\circ$ is always less than the minimum magnetic force magnitude when $\alpha = 0^\circ$ for any position $\hat{\mathbf{p}}_c$.

Fig. 4.3(b) shows the maximum, minimum, and range of the magnetic torque magnitude (normalized by $2\gamma_1$) for lead angles $\alpha = 20^\circ$ and $\alpha = 90^\circ$ over one actuator revolution plotted as a function of θ. The lead angle $\alpha = 20^\circ$ was chosen for illustration, rather than $\alpha = 0^\circ$, because $\|\boldsymbol{\tau}\| = 0$ when $\alpha = 0^\circ$ regardless of the position $\hat{\mathbf{p}}_c$. The maximum magnetic torque magnitude occurs when $\alpha = 90^\circ$ and $\theta = 90^\circ$, which is a radial position.

Comparing Fig. 4.3(a) with Fig. 4.3(b) illustrates the trade-off between magnetic torque and force for the case when $\alpha = 90^\circ$ (i.e., at step-out). The trade-off can be seen for any angle of α in the range $[0^\circ, 90^\circ]$ in Fig. 4.3(c) and Fig. 4.3(d), which show the maximum, minimum, and range of magnetic force and torque magnitudes, respectively, as a function of the position $\hat{\mathbf{p}}_c$, parameterized by the angle θ. In radial positions (where $\theta = 90^\circ$), it is possible to maximize either force or torque magnitude depending on the lead angle. In general, a large α results in maximizing magnetic torque, while a small α maximizes force.

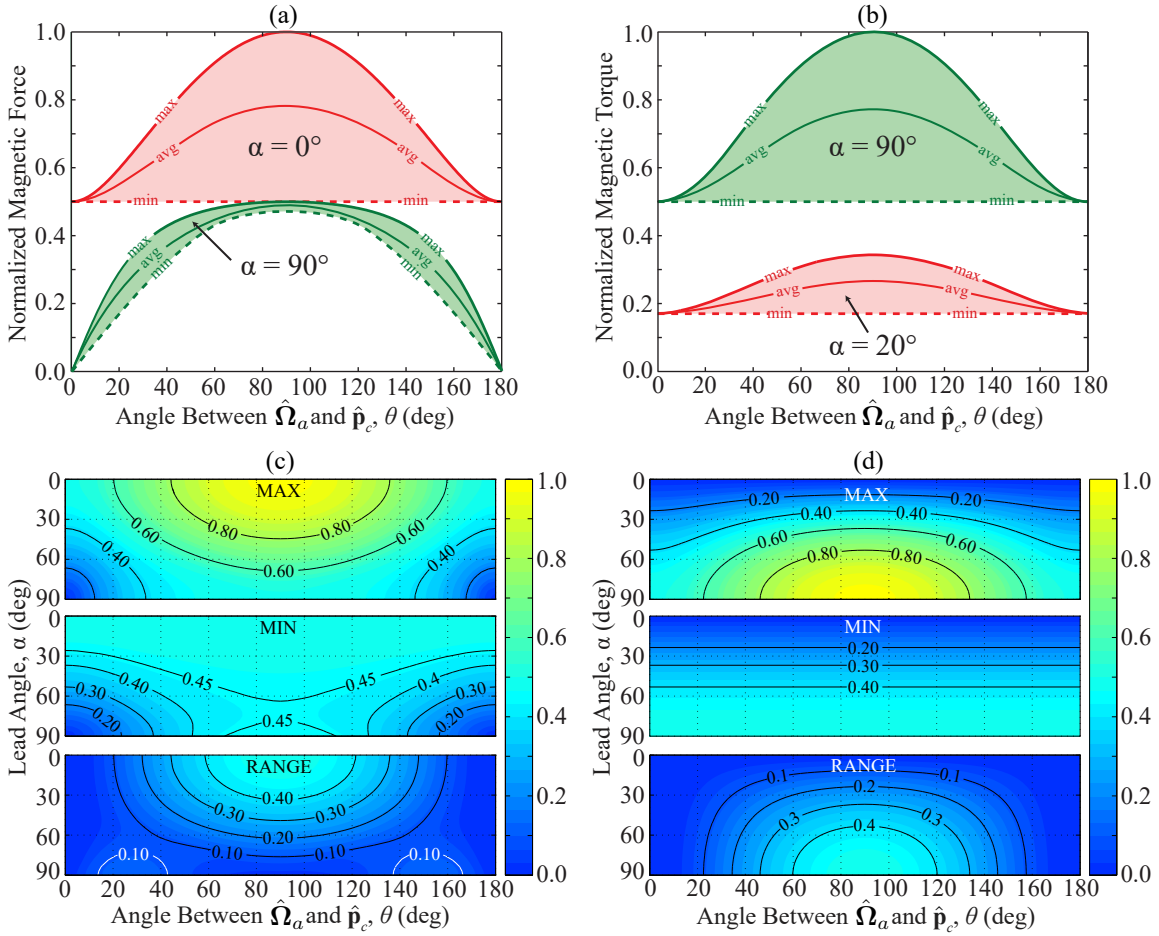

Figure 4.3. Illustrates the trade-off between magnetic force and torque magnitudes. The magnetic force and torque magnitudes (normalized by $2\gamma_2$ and $2\gamma_1$, respectively) are shown in (a) and (b), respectively, for two lead angles α, plotted as a function of the angle θ that measures the angle between $\hat{\mathbf{\Omega}}_a$ and the position $\hat{\mathbf{p}}_c$. The maximum, minimum, and range of normalized magnetic force and torque magnitudes are shown in (c) and (d), respectively, for angles of α in the range $[0°, 90°]$.

4.5.2 Propulsion With a Simplified Model

For a screw-type capsule in a lumen, the applied magnetic force and torque are converted to the capsule's spatial and angular velocity by the interaction of the capsule with the lumen. This interaction can be complex, particularly if the lumen is soft and deformable as are the small intestines. We simplify our analysis of the propulsion of an untethered capsule using a 2-DOF model that assumes the magnetic and friction torques dominate any torque caused by inertia, and that the only component of the magnetic force and torque contributing to the propulsion of the capsule is the component of the

applied force and torque parallel to the lumen axis, which we denote by $\hat{\mathbf{l}}$. We assume that the actuator magnet's rotation axis is set according to (4.10) such that $\hat{\boldsymbol{\Omega}}_c$ is always instantaneously parallel to the capsule's principle axis $\hat{\mathbf{x}}_c$, which in turn is approximately parallel to the lumen axis $\hat{\mathbf{l}}$ (i.e., $\hat{\mathbf{l}} = \hat{\mathbf{x}}_c$ or $\hat{\mathbf{l}} = -\hat{\mathbf{x}}_c$ depending on the desired direction of motion in the lumen).

As the capsule enters a turn, the geometry of the lumen will cause the capsule's axis $\hat{\mathbf{x}}_c$ to deviate from the rotation axis of the applied field ($\boldsymbol{\Omega}_c$) by an angle Ψ, as shown in Fig. 4.4. If Ψ is relatively small, the resulting magnetic restoring torque will also be small and the capsule will continue to rotate because of compliance in the magnetic field. We have previously shown that our propulsion method is robust to these types of misalignments [23]. The capsule's heading is updated based on the sensor measurements and the capsule is continually tracked and propelled throughout the curve. In this way the capsule is not steered around curves; rather, it is simply driven forward and it naturally adapts to curves.

The force and torque are mapped to the capsule's spatial velocity $\mathbf{v}_c$ and angular velocity $\boldsymbol{\omega}_c$ by the propulsion matrix $\boldsymbol{\Lambda}$:

$$\begin{bmatrix} {}^r\mathbf{v}_c \\ {}^r\boldsymbol{\omega}_c \end{bmatrix} = \begin{bmatrix} \boldsymbol{\Lambda}_1 & \boldsymbol{\Lambda}_2 \\ \boldsymbol{\Lambda}_2^\mathsf{T} & \boldsymbol{\Lambda}_3 \end{bmatrix} \begin{bmatrix} {}^r\mathbf{f} \\ {}^r\boldsymbol{\tau} \end{bmatrix} = \boldsymbol{\Lambda} \begin{bmatrix} {}^r\mathbf{f} \\ {}^r\boldsymbol{\tau} \end{bmatrix}, \tag{4.12}$$

where $\boldsymbol{\Lambda}_1, \boldsymbol{\Lambda}_2, \boldsymbol{\Lambda}_3 \in \mathbb{R}^{3\times 3}$ are matrices that depend on friction, and properties of the capsule's geometry such as radius, helix geometry, etc. The assumption that components of magnetic force and torque orthogonal to the lumen axis $\hat{\mathbf{l}}$ have no influence on propulsion parallel to the lumen can be modeled by projecting the applied magnetic force and torque onto the lumen axis, by

$$\boldsymbol{\Lambda}_1 = \lambda_1 {}^r\hat{\mathbf{l}} {}^r\hat{\mathbf{l}}^\mathsf{T}, \boldsymbol{\Lambda}_2 = \lambda_2 {}^r\hat{\mathbf{l}} {}^r\hat{\mathbf{l}}^\mathsf{T}, \text{ and } \boldsymbol{\Lambda}_3 = \lambda_3 {}^r\hat{\mathbf{l}} {}^r\hat{\mathbf{l}}^\mathsf{T}, \tag{4.13}$$

where λ_1, λ_2, λ_3 describe how the applied force and torque are related to spatial and angular velocity. This model has been demonstrated to be a good approximation to the behavior of magnetic helical swimmers in low-Reynolds number fluids [24] (as well as a slightly more complex 6-DOF variant [25]).

4.5.3 Constrained Optimization of the Average Forward Velocity

The capsule's velocity is a result of the combined instantaneous applied magnetic force and torque. Since, in general, the instantaneous direction and magnitude of the applied

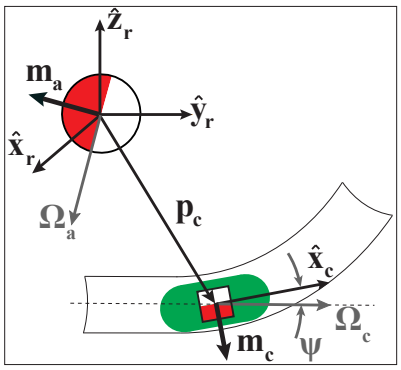

Figure 4.4. Depiction of how the lumen will cause the principle axis of the capsule, $\hat{\mathbf{x}}_c$, to lead the rotation axis of the applied field, $\boldsymbol{\Omega}_c$, by some angle Ψ as the capsule is driven "forward". The turn is then sensed and incorporated by the localization algorithm to update the "forward" direction.

torque $\boldsymbol{\tau}$ and force $\mathbf{f}$ vary as the actuator magnet rotates, the capsule's spatial and angular velocities parallel to the lumen axis (approximated with (4.12) and (4.13)) also vary in time. We propose approximating the net torque and force behavior using the average magnetic torque $\bar{\boldsymbol{\tau}}$ and force $\bar{\mathbf{f}}$ and optimizing for the capsule's average spatial velocity, $\bar{\mathbf{v}}_c$. See Appendix B for derivations of $\bar{\boldsymbol{\tau}}$ and $\bar{\mathbf{f}}$ and the accuracy of using the average magnetic force and torque to approximate the instantaneous values. Assuming the propulsion matrix is constant, the average spatial velocity $\bar{\mathbf{v}}_c$ and angular velocity $\bar{\boldsymbol{\omega}}_c$ are given by:

$$\begin{bmatrix} {}^r\bar{\mathbf{v}}_c \\ {}^r\bar{\boldsymbol{\omega}}_c \end{bmatrix} = \boldsymbol{\Lambda} \begin{bmatrix} {}^r\bar{\mathbf{f}} \\ {}^r\bar{\boldsymbol{\tau}} \end{bmatrix}. \tag{4.14}$$

As shown in Fig. 4.3, there is a trade-off between the force and torque. At any point in time, the capsule's propulsion parameters (λ_1, λ_2) determine whether magnetic torque or force contributes more to the capsule's spatial velocity. By adjusting the position of the actuator magnet relative to the static world frame $\mathbf{o}_r = \mathcal{O}_r - \mathcal{O}_w$ (see Fig. 4.2), and the lead angle α, which is controlled by the rotation speed of the actuator magnet, we can maximize the spatial velocity of the capsule. This constrained optimization problem can be formulated as:

$$\max_{\alpha, \mathbf{o}_r} \ \|\bar{\mathbf{v}}_c\|^2 = \left(\lambda_1 \hat{\mathbf{l}}^\mathsf{T} \bar{\mathbf{f}}(\alpha, \mathbf{o}_r) + \lambda_2 \hat{\mathbf{l}}^\mathsf{T} \bar{\boldsymbol{\tau}}(\alpha, \mathbf{o}_r)\right)^2 \tag{4.15}$$

subject to:

$$\hat{\mathbf{l}} \cdot \mathbf{v}_c \geq 0 \tag{4.16}$$

$$\hat{\mathbf{n}} \cdot \mathbf{p}_t \geq p_{\min} \tag{4.17}$$

where the cost function derived from (4.14) rewards higher average forward velocities. $\bar{\boldsymbol{\tau}}$ and $\bar{\mathbf{f}}$ are nonlinear functions of α and $\mathbf{o}_r$ derived in Appendix B.

In our implementation, there are two inequality constraints. (4.16) ensures the velocity is positive so the capsule moves in the desired "forward" direction. We also need to ensure the actuator magnet does not collide with the patient's abdomen (a parametric surface is defined in our setup, but it could be detected optically or through other methods). The closest point on the surface to the current actuator magnet's position is determined ($\mathcal{O}_t$) and the tangent plane is computed (see Fig. 4.5). We define an auxiliary vector $\mathbf{p}_t = \mathbf{o}_r - \mathbf{o}_t$, where $\mathbf{o}_t$ is the position of $\mathcal{O}_t$ relative to $\mathcal{O}_w$. (4.17) constrains the actuator magnet's position to remain on the outside of the tangent plane, by a minimum distance of $p_{\min}$ where $\hat{\mathbf{n}}$ is the surface normal and $p_{\min} \geq r$ where r is the radius of the actuator magnet. We only consider a single obstacle here, but if there were more than one obstacle, each would be handled accordingly [26].

We use sequential quadratic programming (SQP) to solve the nonlinear constrained optimization problem with the SNOPT library [27]. A locally optimal solution is found by iteratively solving a series of quadratic programming subproblems that maximizes the Langrangian of (4.15) subject to its linearized constraints. The analytic solutions of the partial derivatives of the cost function and constraints with respect to $\mathbf{o}_r$ and α are derived in Appendix C.

4.6 Localization

To use the optimized propulsion system described in the previous section, the full 6-DOF pose of the capsule must be estimated to control for the lead angle. We have developed two localization algorithms; one for use with capsules which have negligible net motion [12], and the other for use with capsules synchronously rotating with the applied field; introduced in [15]. To determine which of the localization methods to use, we first must estimate the capsule's regime.

4.6.1 Detecting the Capsule's Operating Regime

At any given time, the capsule will be operating in one of three regimes: 1) The capsule is rotating synchronously with the applied field. 2) The capsule is in the "step-out" regime

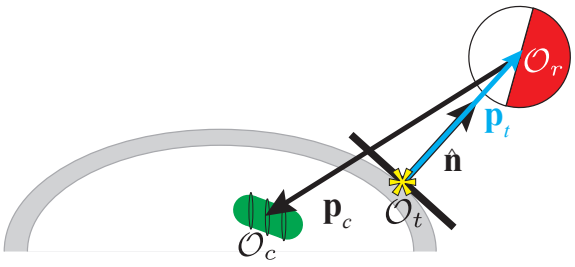

Figure 4.5. The closest point on the patient's abdomen to the actuator magnet is determined ($\mathcal{O}_t$, shown with a *), and a local tangent plane and surface normal $\hat{\mathbf{n}}$ are computed. The actuator magnet is constrained to remain outside of the tangent plane such that the $\hat{\mathbf{n}} \cdot \mathbf{p}_t \geq p_{\text{min}}$ where $\mathbf{p}_t$ is the relative offset between the actuator magnet and $\mathcal{O}_t$.

where the external field is rotated too quickly for the capsule to remain synchronously rotating. When this occurs the capsule rotates erratically back and forth trying to align with the field with little net motion. 3) The capsule is stuck (i.e., effectively stationary). We only need to distinguish whether or not the capsule is synchronously rotating with the external field because the method of [12] can be used to estimate the pose of a capsule that is either stationary or in step-out. We have previously shown that knowledge of the lead angle, α, which is the angle between the applied field $\mathbf{b}_c$ and the capsule's dipole moment $\mathbf{m}_c$, is sufficient to distinguish this [18]. To summarize, if the lead angle remains relatively constant over a full rotation of the external field, the capsule must be synchronously rotating with the field, but if the capsule is stationary or in step-out, α will periodically change signs (see Fig. 4.6). To prevent false positives that may occur when the capsule is rotating synchronously with a lead angle near zero, in addition to the sign change, the condition that $|\alpha| > \pi/2\,\text{rad}$ must be met at least once in a given rotation to determine that the rotation is not synchronous.

4.6.2 Initial Localization of a Stationary Capsule

Initially, we assume no precise prior location information, just that the capsule is placed somewhere in a known workspace (e.g., the patient's abdomen). The origin of the capsule's frame, $\mathcal{O}_c$, is located at the center of its internal magnet, the origin of the robot's tool frame, $\mathcal{O}_r$, is placed at the center of the external dipole source, and the static world frame is chosen to reside at the base of the robot, as shown in Fig. 4.2. We assume the robot's tool frame is at some known offset from the world frame $\mathbf{o}_r$, but that it is constrained to remain

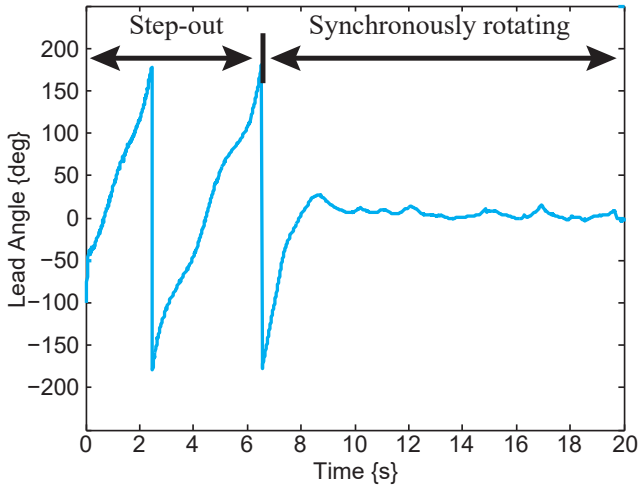

Figure 4.6. The lead angle (α) over time for a tested trajectory with the external field rotating at 0.25 Hz. When the capsule is synchronously rotating with the field, α remains relatively constant. If the capsule is in step-out, the lead angle will oscillate between $\pm 180^{\circ}$.

aligned with the static world frame such that ${}^{w}\mathbf{R}_{r} = \mathbf{I}_{3}$. We will solve for the capsule's 6-DOF pose, comprising position ${}^{r}\mathbf{p}_{c}$ and orientation ${}^{r}\mathbf{R}_{c}$, relative to the robot's tool frame. While it may be beneficial to transform the position and orientation to a static world frame for clinical applications, in terms of controlling the capsule, the robot's tool frame is preferable because all magnetic equations are derived with respect to the actuator magnet. As the pose of the robot's tool frame is known from the forward kinematics, and we solve for the 6-DOF capsule pose relative to this frame, it is trivial to transform the capsule's pose into any other desired coordinate frame using a homogeneous transformation.

Assuming the capsule has no (or approximately no) net motion, using magnetic field measurements from sensors embedded in the capsule, and rotating the actuator magnet about multiple orthogonal axes, it is possible to determine the 6-DOF capsule pose relative to the external source (i.e., in the robot's tool frame) to within a few millimeters and a few degrees of the true capsule pose using the method from [12]. Here, we modify the method for use with quaternions, since we previously employed the exponential formulation of a rotation matrix.

The capsule's full 6-DOF pose is represented by a 7×1 state vector ${}^{r}\mathbf{s} = \left[{}^{r}\mathbf{p}_{c}^{\mathsf{T}}\ {}^{r}\mathcal{Q}_{c}^{\mathsf{T}}\right]^{\mathsf{T}}$. The capsule's pose is estimated by minimizing the cost function $||\mathbb{B}_{m} - \mathbb{B}_{e}||^{2}$ using the Levenberg-Marquardt algorithm, where $\mathbb{B}_{m}$ is an array of the measured magnetic field readings corresponding to a single rotation of the actuator magnet about each of the $\mathbf{x}_{r}$,

$\mathbf{y}_r$, and $\mathbf{z}_r$ axes, and $\mathbb{B}_e$ is an array of the magnetic field readings estimated by (4.4). As the initial pose is unknown, five initial guesses, which are spread throughout the possible workspace, are used. The estimated pose resulting in the minimum norm of residual error between the estimated and measured sensor readings is chosen.

In this chapter, the same process just described is also used to localize the capsule if it has been determined "lost" or "stuck" (i.e., the uncertainty of the estimate is above a desired threshold, or the capsule has been stationary for an extended period of time).

4.6.3 Real-Time Localization of a Nonstationary Capsule

In our original implementation we utilized the EKF [15]. Here, we compare the EKF results to the SRUKF, which provides a gradient-free approach to match higher-order nonlinearities. Both of the nonlinear Kalman filters use the following system model to describe the capsule's motion and measurements:

$$\mathbf{s}_t = G(\mathbf{s}_{t-1}, \mathbf{u}_{t-1}) + \mathbf{g}_{t-1} \tag{4.18}$$

$$\mathbf{y}_t = H(\mathbf{s}_t, \mathbf{u}_t) + \mathbf{h}_t \tag{4.19}$$

where $\mathbf{s}_t$ is the capsule's state at time step t, $\mathbf{u}_{t-1}$ is the input to the system at the previous time step, G models the system dynamics, $\mathbf{y}_t$ are the estimated observations, H is the measurement model, and $\mathbf{g}_t \sim \mathcal{N}(0, \mathbf{Q}_t)$ and $\mathbf{h}_t \sim \mathcal{N}(0, \mathbf{N}_t)$ are the zero-mean process and measurement noise parameters with known covariances of $\mathbf{Q}_t$ and $\mathbf{N}_t$, respectively. Both of the nonlinear Kalman filters have the same high-level algorithmic structure, alternating between a prediction step based on a process model and an update step that refines the prediction based on the sensor measurements.

4.6.3.1 Process Model Implementation

The same state introduced in the initialization step is used in the Kalman filters: ${}^r\mathbf{s} = [{}^r\mathbf{p}_c^\mathsf{T} \; {}^r\mathcal{Q}_c^\mathsf{T}]^\mathsf{T}$. The system input consists of the actuator magnet's pose (position and dipole orientation) ${}^r\mathbf{u} = \left[{}^r\mathbf{o}_r^\mathsf{T} \; {}^r\mathbf{m}_a{}^\mathsf{T}\right]^\mathsf{T}$. To estimate the capsule's dynamics, the propulsion model introduced in Section 4.5.2 is used, where the capsule's helical thread translates magnetic force and torque into forward and angular velocity (4.12). The magnetic torque and force can be calculated from (4.5) and (4.6), respectively.

Instead of updating the entire 7×1 state in a single function, the position and orienta-

tion are updated individually and combined:

$$\begin{bmatrix} {}^{r}\mathbf{p}_{c} \\ {}^{r}\mathcal{Q}_{c} \end{bmatrix} = \begin{bmatrix} G_{\mathbf{p}}({}^{r}\mathbf{s}_{t-1}, {}^{r}\mathbf{u}_{t-1})^{\mathsf{T}} \\ G_{\mathcal{Q}}({}^{r}\mathbf{s}_{t-1}, {}^{r}\mathbf{u}_{t-1})^{\mathsf{T}} \end{bmatrix}. \tag{4.20}$$

The position is updated using:

$${}^{r}\mathbf{p}_{c,t} = {}^{r}\mathbf{p}_{c,t-1} + \Delta t {}^{r}\mathbf{v}_{c} \tag{4.21}$$

where Δt is the time between discrete updates.

The incremental change in orientation can be found by transforming the angular velocity into a unit quaternion,

$$\mathcal{Q}_{\Delta} = \cos\left(\frac{||{}^{r}\boldsymbol{\omega}_{c}||\Delta t}{2}\right) + \frac{{}^{r}\boldsymbol{\omega}_{c}}{||{}^{r}\boldsymbol{\omega}_{c}||}\sin\left(\frac{||{}^{r}\boldsymbol{\omega}_{c}||\Delta t}{2}\right) \tag{4.22}$$

which we use as a rigid-body operator to update the orientation:

$${}^{r}\mathcal{Q}_{c,t} = \mathcal{Q}_{\Delta}{}^{r}\mathcal{Q}_{c,t-1}. \tag{4.23}$$

Note, $\mathcal{Q}$ should always be normalized after any update to ensure the rotation equations from Appendix A are valid.

The process model noise is difficult to measure, so the covariance was tuned experimentally to provide desired tracking. All states are assumed independent, such that $\mathbf{Q}$ is nonzero only along its diagonal. Due to the slow nature of capsule endoscopy, we know the capsule's next position will be in close proximity to its previous position and place high certainty on the position's process model (the upper left 3×3 submatrix of $\mathbf{Q}$, which have units $\{\mathrm{m}^2\}$). The capsule's orientation is less certain because of the rotating fields and this is reflected in the chosen values (bottom right 4×4 submatrix of $\mathbf{Q}$, which are unitless):

$$\mathbf{Q} = \mathrm{diag}(0.001, 0.001, 0.001, 100, 100, 100, 100) \cdot 10^{-5}.$$

4.6.3.2 Measurement Model Implementation

This method is a recursive variant of the original algorithm presented in [12] and similarly assumes there are n magnetic sensors rigidly embedded inside the capsule (in practice we use $n = 6$). The measurement model H estimates the sensor measurements by projecting the expected dipole field onto the sensor's measuring axis using (4.4). The n measurements are combined into a column vector:

$$H({}^{r}\mathbf{p}_{c}, {}^{r}\mathcal{Q}_{c}, {}^{r}\mathbf{m}_{a}, \mathbf{D}) = \begin{bmatrix} b_{i}({}^{r}\mathbf{p}_{i}, {}^{r}\mathcal{Q}_{c}, {}^{r}\mathbf{m}_{a}) \\ \vdots \\ b_{n}({}^{r}\mathbf{p}_{n}, {}^{r}\mathcal{Q}_{c}, {}^{r}\mathbf{m}_{a}) \end{bmatrix} \tag{4.24}$$

where $\mathbf{D}$ is a $3 \times n$ matrix where the i^{th} column corresponds to ${}^{c}\boldsymbol{\delta}_i$ and is used with ${}^{r}\mathbf{p}_c$ to calculate ${}^{r}\mathbf{p}_i$ using (4.3). Each row in H is calculated using (4.4).

The measurement noise covariance matrix $\mathbf{N}\{\mathrm{T}^2\}$ was estimated using sensor data from five locations spread throughout the workspace. Each sensor is assumed independent so the resulting values were placed along the diagonal of the 6×6 matrix, with the remaining values set to zero:

$$\mathbf{N} = \mathrm{diag}(51.1, 49.4, 48.4, 57.2, 49.7, 59.1) \cdot 10^{-7}.$$

4.6.3.3 Extended Kalman Filter

We use a discrete-time implementation of the EKF [28], assuming constant inputs between samples, and the system model in (4.18) and (4.19). The EKF method is shown in Alg. 1. The *a priori* estimate predicts the next state $\mathbf{s}$ and its corresponding covariance $\mathbf{P}$ from the process model G and is denoted by the $-$ superscript. The measurement update improves the *a priori* prediction by incorporating the observations to form the *a posteriori* state estimate, which is denoted with a $+$ superscript. The analytic solutions for Jacobian matrices $\mathbf{G}$ (process model) and $\mathbf{H}$ (measurement model) are computed in Appendices D and E, respectively.

4.6.3.4 Square-root Unscented Kalman Filter

Although the EKF is the most widely used state-estimation algorithm for nonlinear systems [28], and it was the method we employed in [15], it has a few less-than-desirable traits. First, if the system is highly nonlinear, the first-order approximation given by the EKF may not be sufficient. Second, calculating the partial derivatives can be complicated and time-consuming. The Unscented Kalman filter provides a gradient-free alternative that is at worst a second-order approximation [29]. The basic philosophy is that, although it is difficult to transform a probability density function through a nonlinear function, it is simple to transform a single point. Choosing a set of points to approximate the desired density function is also straightforward. If we have a known mean $\bar{\mathbf{s}}$ and covariance $\mathbf{P}$ for some state vector $\mathbf{s}$, we can choose a set of vectors known as sigma points whose combined mean and covariance are $\bar{\mathbf{s}}$ and $\mathbf{P}$. It is simple to then transform this set of points using our nonlinear process and measurement models. A weighted combination of the

Algorithm 1 EKF algorithm.

s is the state vector, **P** is the covariance matrix, **z** is a vector of observations, **K** refers to the Kalman gain, **G** is the Jacobian of the process model, and **H** is the Jacobian of the measurement model.

for $t = 1, \ldots, \infty$ **do**
Time update equations: (*a priori*)
    $\mathbf{s}_t^- = G(\mathbf{s}_{t-1}^+, \mathbf{u}_{t-1})$
    $\mathbf{G}_{t-1} = \frac{\partial G}{\partial \mathbf{s}}\Big|_{\mathbf{s}_{t-1}^+, \mathbf{u}_{t-1}}$

    $\mathbf{P}_t^- = \mathbf{G}_{t-1}\mathbf{P}_{t-1}^+\mathbf{G}_{t-1}^\mathsf{T} + \mathbf{Q}_{t-1}$
Measurement update equations: (*a posteriori*)
    $\mathbf{H}_t = \frac{\partial H}{\partial \mathbf{s}}\Big|_{\mathbf{s}_t^-, \mathbf{u}_t}$
    $\mathbf{K}_t = \mathbf{P}_t^-\mathbf{H}_t^\mathsf{T}(\mathbf{H}_t\mathbf{P}_t^-\mathbf{H}_t^\mathsf{T} + \mathbf{N}_t)^{-1}$
    $\mathbf{s}_t^+ = \mathbf{s}_t^- + \mathbf{K}_t(\mathbf{z}_t - H(\mathbf{s}_t^-, \mathbf{u}_t))$
    $\mathbf{P}_t^+ = (\mathbf{I}_7 - \mathbf{K}_t\mathbf{H}_t)\mathbf{P}_t^-$

resulting transformed vectors will provide an estimate of the true mean and covariance that is equally good, or better, than the EKF. For more details regarding the unscented transform see [28]. There is a trade-off when choosing the sigma points between accuracy and computation time. We implemented the sigma points described by [30] because the chosen 2j+1 sigma points (where j is the length of the state vector) and scaling factor κ (where κ determines the spread of the sigma points) gives the ability to match higher-order moments if the distribution is Gaussian.

$$
\begin{aligned}
\mathcal{X}_0 &= \mathbf{s} \\
\mathcal{X}_i &= \mathbf{s} + \left(\sqrt{(j+\kappa)\mathbf{P}}\right)_i^\mathsf{T} \quad i = 1, \ldots, j \\
\mathcal{X}_{j+i} &= \mathbf{s} - \left(\sqrt{(j+\kappa)\mathbf{P}}\right)_i^\mathsf{T} \quad i = 1, \ldots, j \\
\boldsymbol{\varphi}_0 &= \frac{\kappa}{j+\kappa} \\
\boldsymbol{\varphi}_i &= \frac{1}{2(j+\kappa)} \quad i = 1, \ldots, 2j
\end{aligned}
\tag{4.25}
$$

$\mathcal{X}$ is a set of sigma points, $\left(\sqrt{(j+\kappa)\,\mathbf{P}}\right)_i$ is the i^{th} row of the matrix $\sqrt{(j+\kappa)\,\mathbf{P}}$, and $\boldsymbol{\varphi}$ is a weight vector.

The square-root variant of the Unscented Kalman filter was implemented because of its improved numerical stability [31] over the original Unscented Kalman filter. The SRUKF

algorithm is described in Alg. 2. In this formulation, $\mathbf{S}$ is assumed to be the *lower* Cholesky factor. It should be noted that some implementations (e.g., MATLAB) return the *upper* Cholesky factor. The implementation of the SRUKF in Alg. 2 is $O(N^3)$; for more time-sensitive applications, other implementations of the SRUKF may be beneficial [32].

4.7 Process Model Parameter Estimation

Our process model (Section 4.6.3.1) relies on knowledge of how the capsule's helix will transfer magnetic force and torque into forward and angular velocity from the propulsion matrix (see (4.12)). This matrix has three free parameters (λ_1, λ_2, and λ_3) which are dependent on both the capsule and lumen. In our prior implementation [15], these parameters were experimentally estimated in the lumen prior to commencing trials. Ideally, these parameters could be found on-line and change as the capsule moves through the intestines, adapting to the capsule's current environment. With this aim in mind, an additional SRUKF was implemented in parallel for parameter estimation. The parameter vector $\boldsymbol{\lambda} = [\lambda_1 \;\; \lambda_3 \;\; \lambda_2]^\mathsf{T}$ is modified to minimize the error between the process model's estimate and the sensor readings. For physical realism, $\boldsymbol{\lambda}$ is constrained to positive values.

A modified SRUKF for use in parameter estimation is described in [31] and is shown in Alg. 3. It is similar to the original SRUKF except the process model predicts that the next estimate will be equivalent to the previous state (Alg. 3, line 3). An exponential weighting factor, ζ, is used in place of the process noise covariance update.

In our implementation, the measurement model (H_r) is equivalent to the process model of the state estimate SRUKF (Alg. 3, line 6). Instead of using sensor measurements, the predicted state is compared against the observed state estimate $\mathbf{s}_t$ (Alg. 3, line 12). The measurement noise covariance matrix $\mathbf{N}_p$ was experimentally tuned to provide desired results. Its units are the same as $\mathbf{Q}$.

$$\mathbf{N}_p = \mathbf{I}_7 \cdot 10^{-4}$$

4.8 Complete Closed-Loop Localization and Propulsion System

A block diagram depicting the complete closed-loop localization and propulsion system is shown in Fig. 4.1. Given the capsule's estimated pose from either the initialization or the nonlinear Kalman filter, and whether or not the capsule is rotating with the applied

Algorithm 2 The SRUKF algorithm used for state estimation from [31].

$\mathbf{s}$ is the state vector, $\mathbf{u}$ is the input vector, $\mathbf{z}$ is a vector of observations, $\mathbf{S}$ is square-root of the covariance matrix ($\mathbf{P} = \mathbf{S}\mathbf{S}^\mathsf{T}$), $\boldsymbol{\varphi}$ is a vector of weights defined in (4.25) κ is a scaling factor influencing the spread of the sigma vectors (we use $\kappa = 1$), qr refers to the QR decomposition, cUpdate is a rank-1 update to the Cholesky factorization (an update or downdate is performed dependent on the sign of $\boldsymbol{\varphi}_0$), chol returns the Cholesky factorization, sgn is the signum function, G is the function describing the process model, and H is the measurement model. The subscripts on $\boldsymbol{\varphi}$, $\mathcal{X}$, and $\mathcal{Y}$ refer to the vector index.

for $t = 1, \ldots, \infty$ **do**
  $\mathcal{X}^*_{t-1} = \text{CALCSIGMAPOINTS}(\mathbf{s}_{t-1}, \mathbf{S}_{t-1}, \kappa)$
  Time update equations: (*a priori*)
  $\mathcal{X}^*_{t|t-1} = G(\mathcal{X}_{t-1}, \mathbf{u}_{t-1})$
  $\mathbf{s}^-_t = \sum_{i=0}^{2j} \boldsymbol{\varphi}_i \mathcal{X}^*_{i,t|t-1}$
  $\mathbf{S}^-_t = \text{qr}\left(\left[\sqrt{\boldsymbol{\varphi}_1}(\mathcal{X}^*_{1:2n,t|t-1} - \mathbf{s}^-_t)\ \sqrt{\mathbf{Q}}\right]\right)$
  $\mathbf{S}^-_t = \text{cUpdate}\left(\mathbf{S}^-_t, \mathcal{X}_{0,t|t-1} - \mathbf{s}^-_t, \text{sgn}(\boldsymbol{\varphi}_0)\right)$
  $\mathcal{X}_{t-1} = \text{CALCSIGMAPOINTS}(\mathbf{s}^-_t, \mathbf{S}^-_t, \kappa)$
  Estimate observations:
  $\mathcal{Y}_{t|t-1} = H(\mathcal{X}_{t|t-1}, \mathbf{u}_t)$
  $\tilde{\mathbf{z}}_t = \sum_{i=0}^{2n} \boldsymbol{\varphi}_i \mathcal{Y}_{i,t|t-1}$
  Measurement update equations: (*a posteriori*)
  $\mathbf{S}_y = \text{qr}\left(\left[\sqrt{\boldsymbol{\varphi}_1}\left(\mathcal{Y}_{1:2j,k} - \tilde{\mathbf{z}}_t\right)\ \sqrt{\mathbf{N}}\right]\right)$
  $\mathbf{S}_y = \text{cUpdate}\left(\mathbf{S}_y, \left(\mathcal{Y}_{0,t} - \tilde{\mathbf{z}}_t\right), \text{sgn}(\boldsymbol{\varphi}_0)\right)$
  $\mathbf{P}_{s,z} = \sum_{i=0}^{2j} \boldsymbol{\varphi}_i \left(\mathcal{X}_{i,t|t-1} - \mathbf{s}^-_t\right)\left(\mathcal{Y}_{i,t|t-1} - \tilde{\mathbf{z}}_t\right)^\mathsf{T}$
  $\mathbf{K} = \left(\mathbf{P}_{s,z} / \mathbf{S}_y^\mathsf{T}\right) / \mathbf{S}_y$
  $\mathbf{s}^+_t = \mathbf{s}^-_t + \mathbf{K}(\mathbf{z}_t - \tilde{\mathbf{z}}_t)$
  $\mathbf{U} = \mathbf{K}\mathbf{S}_y$
  $\mathbf{S}^+_t = \mathbf{S}^-_t$
  for $\rho = 1, \ldots,$ columns of $\mathbf{U}$ **do**
    $\mathbf{S}^+_t = \text{cUpdate}\left(\mathbf{S}^+_t, \mathbf{U}(:, \rho), -1\right)$
function CALCSIGMAPOINTS($\mathbf{s}, \mathbf{S}, \kappa$)
  $\boldsymbol{\Sigma} = \sqrt{j + \kappa}\mathbf{S}^\mathsf{T}$
  $\mathcal{X} = [\mathbf{s},\ \ \mathbf{s} + \boldsymbol{\Sigma},\ \ \mathbf{s} - \boldsymbol{\Sigma}]$
return $\mathcal{X}$

Algorithm 3 The SRUKF algorithm used for parameter estimation from [31].

$\boldsymbol{\lambda}$ is the parameter vector, $\mathbf{u}$ is the input vector, $\mathbf{s}_t$ is the current observed state vector, $\mathbf{S}_\lambda$ is square-root of the covariance matrix, $\boldsymbol{\varrho}$ is a vector of weights defined in (4.25), κ determines the spread of the sigma vectors (we use $\kappa = 1$), ζ is an exponential weighting factor (we use $\zeta = 0.9995$), H_λ is the measurement model – in our implementation it is equivalent to G, $\mathbf{N}_p$ is the measurement noise covariance matrix, and j_p is the length of $\boldsymbol{\lambda}$. The subscripts on $\boldsymbol{\varrho}$, $\mathcal{X}$, and $\mathcal{D}$ refer to the vector index. Functions are defined in Alg. 2.

for $t = 1, \ldots, \infty$ **do**
Time update equations: (*a priori*)
  $\boldsymbol{\lambda}_t^- = \boldsymbol{\lambda}_{t-1}^+$
  $\mathbf{S}_{\lambda,t}^- = \zeta^{-1/2}\mathbf{S}_{\lambda,t-1}^+$
  $\mathcal{X}_{t-1} = \text{CALCSIGMAPOINTS}(\boldsymbol{\lambda}_t^-, \mathbf{S}_{\lambda,t}^-, \kappa)$
Estimate observations:
  $\mathcal{D}_{t|t-1} = H_\lambda(\mathcal{X}_{t|t-1}, \mathbf{u}_t)$
  $\tilde{\mathbf{d}}_t = \sum_{i=0}^{2j_p} \boldsymbol{\varrho}_i \mathcal{D}_{i,t|t-1}$
Measurement update equations: (*a posteriori*)
  $\mathbf{S}_d = \text{qr}\left(\left[\sqrt{\boldsymbol{\varrho}_1}\left(\mathcal{D}_{1:2n,k} - \tilde{\mathbf{d}}_t\right) \ \sqrt{\mathbf{N}_p}\right]\right)$
  $\mathbf{S}_d = \text{cUpdate}\left(\mathbf{S}_d, \left(\mathcal{D}_{0,t} - \tilde{\mathbf{d}}_t\right), \text{sgn}(\boldsymbol{\varrho}_0)\right)$
  $\mathbf{P}_{\lambda,d} = \sum_{i=0}^{2j_p} \boldsymbol{\varrho}_i \left(\mathcal{X}_{i,t|t-1} - \boldsymbol{\lambda}_t^-\right)\left(\mathcal{D}_{i,t|t-1} - \tilde{\mathbf{d}}_t\right)^\mathsf{T}$
  $\mathbf{K} = \left(\mathbf{P}_{\lambda,d}/\mathbf{S}_{\mathbf{d}t}^\mathsf{T}\right)/\mathbf{S}_{\mathbf{d}t}$
  $\boldsymbol{\lambda}_t^+ = \boldsymbol{\lambda}_t^- + \mathbf{K}(\mathbf{s}_t - \tilde{\mathbf{d}}_t)$
  $\mathbf{U} = \mathbf{K}\mathbf{S}_d$
  $\mathbf{S}_{\lambda,t}^+ = \mathbf{S}_{\lambda,t}^-$
  for $\rho = 1, \ldots,$ columns of $\mathbf{U}$ **do**
    $\mathbf{S}_{\lambda,t}^+ = \text{cUpdate}\left(\mathbf{S}_{\lambda,t}^+, \mathbf{U}(:,\rho), -1\right)$

field, the external dipole's pose is updated optimally for forward capsule propulsion. Pseudocode is given in Alg. 4. The actuator speed is adjusted to minimize the error between α and α_d, where α_d is the result of the constrained optimization described in Section 4.5.3.

In our experimental setup, the SAMM was mounted on the end-effector of a 6-DOF robotic arm and used as our actuator magnet. Our prototype capsule was introduced in [12] (see Fig. 4.7(a)). It measures 42 mm in length and 13.5 mm in diameter not including the helix for propulsion. The capsule is embedded with six Allegro A1392 linear one-axis Hall-effect sensors arranged surrounding a 108 mm^3 cubic NdFeB permanent magnet. The sensors are read at 100 Hz, but are wirelessly sent to the PC in batches at 20 Hz. The Kalman filters were implemented as though each set of sensor data is received individually at the appropriate times.

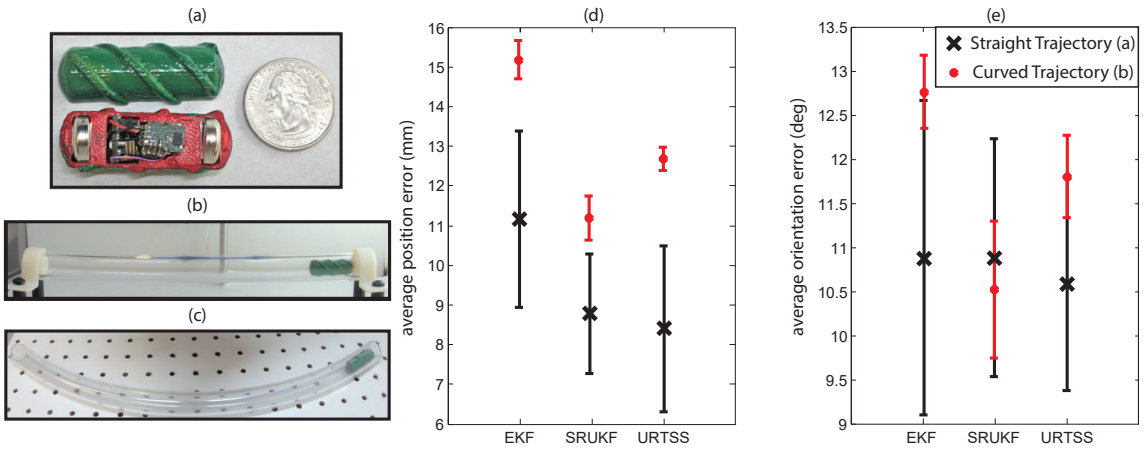

Figure 4.7. Localization performance comparison of the EKF, SRUKF, and URTSS. (a) Our prototype capsule embedded with a permanent magnet and six Hall-effect sensors was introduced in [12]. Five trials from each of the straight (b) and curved (c) lumens were used and the resulting mean and standard deviation of the position (d) and orientation (e) error are shown. Black x's correspond to the straight trajectory and the red dots to the curved path.

Algorithm 4 Psuedocode to update the SAMM pose.

s is the estimated capsule state, **u** is the actuator magnet's current pose, *isRotating* is a Boolean representing the operating regime of the capsule, $||\boldsymbol{\Omega}_a||_{t-1}$ is the actuator's rotation speed at the prior time step, and α is the current lead angle. Due to hardware constraints, we have an upper threshold on the actuator's rotation speed ($\omega_{\max} = 3\,\text{Hz}$), the lower threshold ensures the actuator magnet always provides a rotating field ($\omega_{\min} = 0.25\,\text{Hz}$). $\mathbf{p}_d$ and α_d result from our optimization routine (Section 4.5.3) and are the desired position offset between the capsule and the dipole source and desired lead angle, respectively.

```
1: ʳp_c ← s[1:3], ʳQ_c ← s[4:7]
2: ʳR_c ← QUATERNIONTOROTATIONMATRIX(ʳQ_c)
3: ʳΩ̂_c ← ʳR_c(:,1)
4: [p_d, α_d] ←CALCULATEOPTIMALSAMMPOSE(s, u)
5: ʳp_{r,t} ← ʳp_c + ʳp_{r,t−1} − ʳp_d
6: ω_a ← ||Ω_a||_{t−1}
7: Ω̂_{a,t} ← Eq. (4.10)
8: if !isRotating then Ω_{a,t} = Ω̂_a ω_min
9: else
10:     if (α > α_d & 0.99ω_a ≥ ω_min) then
11:         Ω_{a,t} = 0.99ω_a Ω̂_{a,t}
12:     else if (α < α_d & 1.01ω_a ≤ ω_max) then
13:         Ω_{a,t} = 1.01ω_a Ω̂_{a,t}
14:     else Ω_{a,t} = ω_a Ω̂_{a,t}
```

4.8.1 Experimental Comparison of Kalman Filters

To compare the performance of the EKF and the SRUKF we tested each algorithm on data logged from a set of ten trajectories where the capsule's 5-DOF pose is known using a stereo vision system. The data set included five trajectories through a straight lumen (Fig. 4.7(b)) and five trajectories through a slightly curved lumen (Fig. 4.7(c)). In the curved trajectory, the ground truth orientation was estimated by fitting a curve to the camera data and extrapolating the tangent line at the current position. The SRUKF significantly increased the localization accuracy compared to the EKF, with an average reduction in error of 24% in position and 10% in orientation (see Fig. 4.7(d) and 4.7(e)). Orientation error refers to angle-axis representation with respect to the capsule's heading; the capsule's roll angle is not detected visually, so its error is not reported. We found a significant statistical advantage (with 95% confidence) to using the SRUKF over the EKF for both position and orientation in the curved-lumen trials. Although there was a statistically significant advantage to using an SRUKF for position estimates in the straight trajectories (with 90% confidence), we did not find any significant benefit to the use of the SRUKF for orientation, although our data set is not large enough to definitively say that there is no difference. We believe the difference in results between the straight and curved trajectories is due to the increased nonlinearities and modeling inaccuracies present in the curved-lumen trials.

We also implemented the Unscented Rauch-Tung-Striebel smoother (URTSS) to determine if increasing the time horizon (including future measurements) could further improve our localization results. The URTSS works by passing through the data twice: A forward pass through the data uses an Unscented Kalman filter to estimate the state, and the smoothing solution is computed in a backward pass (for details on the URTSS refer to [33]). Although the URTSS does slightly improve accuracy in straight trajectories (Fig. 4.7(d) and 4.7(e)), we found no significant difference in using it over the SRUKF. In the curved trials, the URTSS performs worse than the SRUKF (with 95% confidence). The worse performance on the curved trajectories is likely due to our assumptions in the process model that restrict the capsule to forward or backward motion along its principle axis. Based on these results, all further demonstrations will use the SRUKF.

4.8.2 Experiments in Phantom Intestines

In all experimental demonstrations, the placement of the actuator magnet and its rotation speed are the result of the optimization routine described in Section 4.5. It maximizes the capsule's forward velocity, which is the result of a combination of two terms ($\lambda_1 \mathbf{f}$) and ($\lambda_2 \boldsymbol{\tau}$), where λ_1 and λ_2 change over time as a result of the parameter-estimation SRUKF. The optimization tends to result in maximizing one of the terms with a desired θ (the angle between $\hat{\boldsymbol{\Omega}}_a$ and $\hat{\mathbf{p}}_c$) of either $\theta = 0^\circ$ or $\theta = 90^\circ$. In general, to maximize the first term the optimization tries to achieve a configuration where the actuator magnet is in front of the capsule ($\theta = 0^\circ$) and the field is rotated at slow speeds. However, the constraints often prevent this from happening in reality. Note that although radial positions maximize force magnitude (see Fig. 4.3), the maximum force magnitude does not necessarily translate to maximum magnetic force in the desired propulsion direction. Positions in front of the capsule are preferable, and chosen by our constrained optimization, because the magnetic field gradients pull the capsule toward the actuator magnet. If the second term is maximized, the optimization generally results in the actuator magnet being placed directly above the capsule (in a radial position $\theta = 90^\circ$) at relatively higher rotation speeds, such that α approaches 90° to maximize torque.

To illustrate the effect of the improvements we implemented since the system's introduction, we replicated the experiment from [15] using the Boston Scientific phantom of the small intestines (Fig. 4.8). The magnitude of $\mathbf{p}_c$ was set for consistency with the prior trial, but instead of using a fixed desired position offset, in our current experiment $\mathbf{p}_c$ is the result of the constrained optimization function and the rotation speed $\|\boldsymbol{\Omega}_a\|$ is adjusted to regulate α. Our improved system completed the trajectory in approximately a third of the time reported in [15] with an average speed of 6.4 mm/s. Note the results in [15] already tripled the average capsule speed from our previous decoupled localization and propulsion system [12].

4.8.3 Experiments in *Ex vivo* Bovine Intestines

Additional tests were completed in fresh bovine intestines. Prior to each test, the capsule was wrapped in polytetrafluoroethylene (PTFE) thread seal tape to waterproof the capsule and protect the embedded electronics. The intestines were placed in a wet

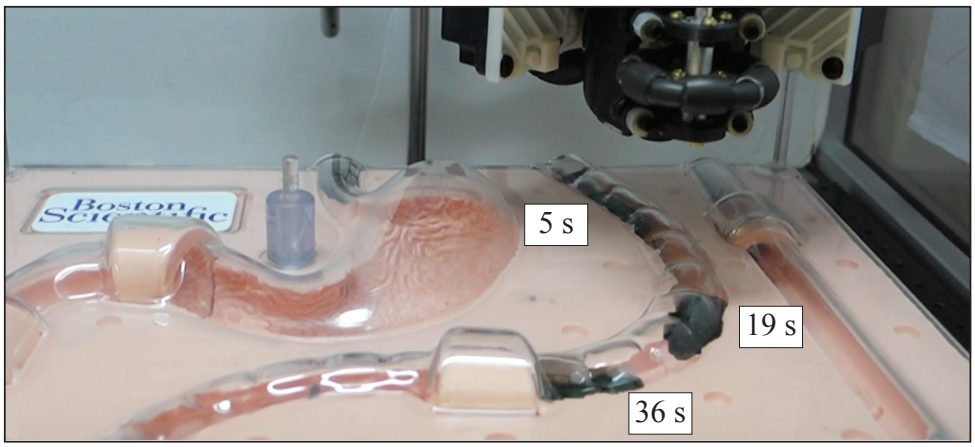

Figure 4.8. A reproduction of an experiment in [15] with $\|\mathbf{p}_c\| \geq 100\,\text{mm}$. The SAMM's position and speed are chosen based on the output from our optimization routine. Please see supplementary video.

container such that the intestines were free to move. A clear plastic lid fixed the ends of the intestines in place and was used to simulate the skin layer preventing the capsule from leaving the workspace. The capsule successfully navigated seven of the nine trials performed across three segments of intestines arranged in a tight U-shaped trajectory. Table 4.1 intestine segments (a)–(c), detail the tested intestines and results in our initial experiment.

The capsule was unable to complete a few segments of intestine, which were not reported in Table 4.1. We believe these failures were the result of two main causes: (1) Some segments of intestines had strictures that were too small for our currently over-sized capsule to navigate. (2) The most common problem was that the intestines would twist with the capsule, trapping the capsule such that it continues to rotate, but there is not enough magnetic torque and force generated to continue its forward motion. This was also the reason for the two failed attempts reported in Table 4.1. Typically, this resulted when the actuator magnet was rotated at high speeds in a radial position attempting to maximize torque. Note that while the intestines twisting resulted in several failed trials, it is not always an issue. In some cases, the intestines will twist with the capsule and then untwist after the capsule has moved through (see supplementary video). It is also likely this will be less of problem in *in vivo* testing because connective tissue will likely make the intestines more rigid than our current test setup.

Table 4.1. Experimental Results for Tested U-Shaped Trajectories in Bovine Small Intestines.

	Intestine Segment			
	(a)	(b)	(c)	(d)
$\|\boldsymbol{\Omega}_{a,\max}\|$ {Hz}	3.0	3.0	3.0	0.5
Length {mm}	635	381	559	483
Completed trials (3 attempts)	3	2	2	3
Mean $\bar{\mathbf{v}}_c$ {mm/s}	3.8	2.3	5.9	2.3
Min $\bar{\mathbf{v}}_c$ {mm/s}	3.4	2.3	5.1	1.3

To address the twisting issue, we subsequently tested an additional segment of intestine but reduced the maximum rotation speed of the actuator magnet $\|\boldsymbol{\Omega}_{a,\max}\|$ to 0.5 Hz (Table 4.1, intestine segment (d)). With this new "low gear" method, the capsule successfully traversed a U-shaped trajectory in all three tested trials. In preliminary testing with $\|\boldsymbol{\Omega}_{a,\max}\| = 3.0\,\text{Hz}$, the capsule was unable to complete a U-shaped trajectory on any of the three attempts in intestine segment (d). If *in vivo* testing has similar twisting issues that prevent the capsule's forward motion, a propulsion method that further explores limiting the capsule and actuator magnet's rotation speeds should be explored.

Limiting the rotation speed of the actuator magnet typically results in a slower average capsule velocity ($\bar{\mathbf{v}}_c$), which is calculated as the total length of intestines traversed divided by the completion time. Across the seven successful trials with $\|\boldsymbol{\Omega}_{a,\max}\| = 3.0\,\text{Hz}$, $\bar{\mathbf{v}}_c$ = 4.1 mm/s, this is reduced to 2.3 mm/s across the three trials when $\|\boldsymbol{\Omega}_{a,\max}\| = 0.5\,\text{Hz}$. Although, the results with $\|\boldsymbol{\Omega}_{a,\max}\| = 0.5\,\text{Hz}$ provide similar average capsule velocities to those that resulted from intestine segment (b), the minimum $\bar{\mathbf{v}}_c$ when each successful trial is considered individually is approximately half when the actuator's speed is limited. Fig. 4.9 depicts the trial resulting in the minimum average capsule velocity for each segment of intestine successfully navigated, corresponding to the bottom row in Table 4.1. Note, when the capsule gets trapped in a fold (intestines segments (b) and (d)), this is automatically detected using the method in Section 4.6.1. The capsule's pose is relocalized using the method described in Section 4.6.2 and then its propulsion continues.

For further demonstration, an S-shape trajectory was navigated in intestine segment (a) with $\|\boldsymbol{\Omega}_{a,\max}\| = 3.0\,\text{Hz}$ (Fig. 4.10). This resulted in an average capsule speed of 3.5 mm/s. In this trajectory, the capsule gets trapped in a fold, which is detected, and it is then re-

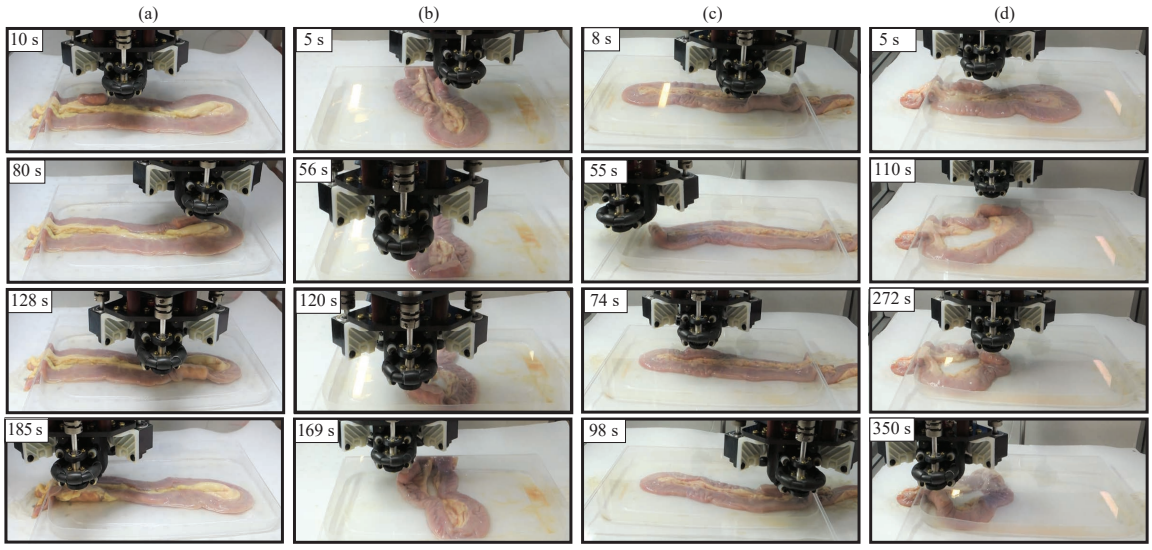

Figure 4.9. Experimental demonstrations of simultaneous localization and closed-loop optimal capsule propulsion through four distinct segments of intestines intially arranged in a tight U-turn (where (a)–(d) correspond to the intestine segments described in Table 4.1). In all shown trajectories, the SAMM's position and speed are chosen based on the output from our optimization routine with $\|\mathbf{p}_c\| \geq 70\,\text{mm}$. Please see supplementary video.

localized and the propulsion is continued.

At the slowest average speed (2.3 mm/s) traversing an average human small intestine would take approximately 43 minutes (compared to the 150–180 minutes taken by food due to peristalsis). In our current setup the actuator magnet must be in close proximity to the capsule; in the bovine intestines (Fig. 4.9 and Fig. 4.10), we constrain $\|\mathbf{p}_c\| \geq 70\,\text{mm}$ (i.e., $p_{\min} = 70\,\text{mm}$). This is a result of the size of our prototype SAMM device. Due to the homothetic property of magnetic fields, if we scaled the size of the external spherical permanent magnet by η, the workspace size would also scale by η.

4.9 Conclusion

This chapter describes the culmination of efforts in our group to enable active wireless capsule endoscopy by combining magnetic localization, propulsion, and proprioceptive sensing into a single closed-loop localization-propulsion system. A Square-root Unscented Kalman filter (SRUKF) is used in the capsule localization, and another SRUKF is used to estimate the process model parameters, which change throughout the trajectory. An opti-

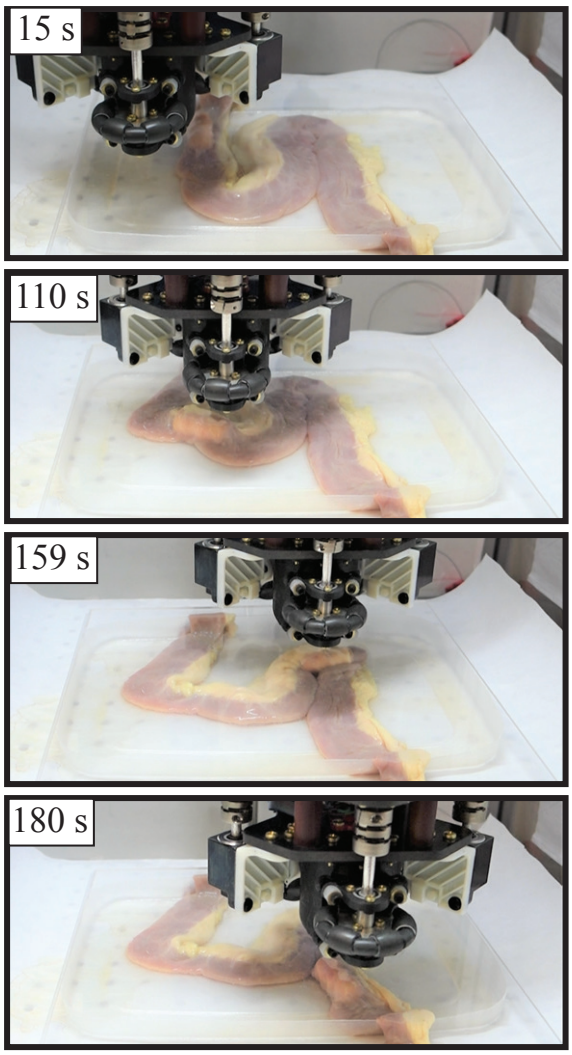

Figure 4.10. Experimental demonstration of simultaneous localization and closed-loop optimal capsule propulsion through intestine segment (a) from Table 4.1 initially arranged in an S-shaped trajectory with $\|\mathbf{p}_c\| \geq 70\,\text{mm}$. Please see supplementary video.

mization routine is utilized to calculate the desired actuator-magnet position and rotation speed to maximize the capsule's forward velocity. We demonstrate our system is able to simultaneously localize and propel a magnetic capsule of approximately clinical scale through tortuous bovine small intestines (*ex vivo*) using a single rotating dipole field for both localization and propulsion.

4.10 References

[1] G. Ciuti *et al.*, "Frontiers of robotic endoscopic capsules: a review," *J. Micro-Bio Robotics*, vol. 11, no. 1, pp. 1–18, June 2016.

[2] A. Z. Taddese, P. R. Slawinski, K. L. Obstein, and P. Valdastri, "Nonholonomic closed-loop velocity control of a soft-tethered magnetic capsule endoscope," in *IEEE/RSJ Int. Conf. Intelligent Robots and Systems*, 2016, pp. 1139–1144.

[3] M. Salerno, R. Rizzo, E. Sinibaldi, and A. Menciassi, "Force calculation for localized magnetic driven capsule endoscopes," in *IEEE Int. Conf. Robotics and Automation*, 2013, pp. 5354–5359.

[4] G. Ciuti, P. Valdastri, A. Menciassi, and P. Dario, "Robotic magnetic steering and locomotion of capsule endoscope for diagnostic and surgical endoluminal procedures," *Robotica*, vol. 28, pp. 199–207, Mar. 2010.

[5] J. Kim, Y. Kwon, and Y. Hong, "Automated alignment of rotating magnetic field for inducing a continuous spiral motion on a capsule endoscope with a twistable thread mechanism," *Int. J. of Prec. Eng. & Manu.*, vol. 13, no. 3, pp. 371–377, Mar. 2012.

[6] A. Uchiyama, H. Kawano, K. Arai, K. Ishiyama, and M. Sendoh, "Medical device guidance system," 2010, US Patent 7,711,408.

[7] Y. Zhang, S. Jiang, X. Zhang, X. Ruan, and D. Guo, "A variable-diameter capsule robot based on multiple wedge effects," *IEEE/ASME Trans. Mechatronics*, vol. 16, no. 2, pp. 241–254, Apr. 2011.

[8] H. Zhou, G. Alici, T. D. Than, and W. Li, "Modeling and experimental characterization of propulsion of a spiral-type microrobot for medical use in gastrointestinal tract," *IEEE Trans. Biomedical Engineering*, vol. 60, no. 6, pp. 1751–1759, June 2013.

[9] T. D. Than, G. Alici, H. Zhou, and W. Li, "A review of localization systems for robotic endoscopic capsules," *IEEE Trans. Bio. Eng.*, vol. 59, no. 9, pp. 2387–2399, Sept. 2012.

[10] A. W. Mahoney and J. J. Abbott, "Generating rotating magnetic fields with a single permanent magnet for propulsion of untethered magnetic devices in a lumen," *IEEE Trans. Robotics*, vol. 30, no. 2, pp. 411–420, Apr. 2014.

[11] E. Paperno, I. Sasada, and E. Leonovich, "A new method for magnetic position and orientation tracking," *IEEE Trans. Magn.*, vol. 37, no. 4, pp. 1938–1940, July 2001.

[12] K. M. Popek, T. Schmid, and J. J. Abbott, "Six-degree-of-freedom localization of an untethered magnetic capsule using a single rotating magnetic dipole," *IEEE Robotics and Automation Letters*, vol. 2, no. 1, pp. 305–312, Jan. 2017.

[13] M. Kim, Y. Hong, and E. Lim, "Position and orientation detection of capsule endoscopes in spiral motion," *Int. J of Prec. Eng. and Manu.*, vol. 11, no. 1, pp. 31–37, Feb. 2010.

[14] D. Son, S. Yim, and M. Sitti, "A 5-D localization method for a magnetically manipulated untethered robot using a 2-D array of hall-effect sensors," *Trans on Mech*, vol. 21, no. 2, pp. 708–716, Apr. 2016.

[15] K. M. Popek, T. Hermans, and J. J. Abbott, "First demonstration of simultaneous localization and propulsion of a magnetic capsule in a lumen using a single rotating magnet," in *IEEE Int. Conf. Robotics and Automation*, 2017, pp. 1154–1160.

[16] K. Madani, S. Khanmohammadi, and V. Azimirad, "Finding optimal actuation configuration for magnetically driven capsule endoscopy based on genetic algorithm," *J. Medical and Biological Engineering*, vol. 36, pp. 776–787, Dec. 2016.

[17] S. E. Wright, A. W. Mahoney, K. M. Popek, and J. J. Abbott, "The spherical-actuator-magnet manipulator: A permanent-magnet robotic end-effector," *IEEE Trans. Robotics*, vol. PP, no. 99, pp. 1–12, 2017.

[18] K. M. Miller, A. W. Mahoney, T. Schmid, and J. J. Abbott, "Proprioceptive magnetic-field sensing for closed-loop control of magnetic capsule endoscopes," in *IEEE Int. Conf. Intel. Robots & Sys.*, 2012, pp. 1994–1999.

[19] E. P. Furlani, *Permanent magnet and electromechanical devices: materials, analysis, and applications*, 1st ed, San Diego, CA, USA: Academic Press, 2001.

[20] A. J. Petruska and J. J. Abbott, "Omnimagnet: An omnidirectional electromagnet for controlled dipole-field generation," *IEEE Trans. Magnetics*, vol. 50, no. 7, pp. 8400810, July 2014.

[21] A. J. Petruska, A. W. Mahoney, and J. J. Abbott, "Remote manipulation with a stationary computer-controlled magnetic dipole source," *IEEE Trans on Robotics*, vol. 30, no. 5, pp. 1222–1227, Oct. 2014.

[22] T. W. R. Fountain, P. V. Kailat, and J. J. Abbott, "Wireless control of magnetic helical microrobots using a rotating-permanent-magnet manipulator," in *Proc. IEEE Int. Conf. Robotics and Automation*, 2010, pp. 576–581.

[23] A. W. Mahoney and J. J. Abbott, "Control of untethered magnetically actuated tools with localization uncertainty using a rotating permanent magnet," in *IEEE Int. Conf. Biomedical Robotics and Biomechatronics*, 2012, pp. 1632–1637.

[24] L. Zhang *et al.*, "Characterizing the swimming properties of artificial bacterial flagella," *Nano Letters*, vol. 9, no. 10, pp. 3663–3667, Oct. 2009.

[25] A. W. Mahoney, J. C. Sarrazin, E. Bamberg, and J. J. Abbott, "Velocity control with gravity compensation for magnetic helical microswimmers," *Advanced Robotics*, vol. 25, no. 8, pp. 1007–1028, May 2011.

[26] J. Schulman *et al.*, "Motion planning with sequential convex optimization and convex collision checking," *Int. J. Robotics Research*, vol. 33, no. 9, pp. 1251–1270, Aug. 2014.

[27] P. E. Gill, W. Murray, and M. A. Saunders, "SNOPT: An SQP alg orithm for large-scale constrained optimization," *SIAM Rev.*, vol. 47, pp. 99–131, Mar. 2005.

[28] D. Simon, *Optimal State Estimation*, 1st ed. Hoboken, NJ, USA: John Wiley & Sons, Inc., 2006.

[29] S. J. Julier and J. K. Uhlmann, "Unscented filtering and nonlinear estimation," *Proc. IEEE*, vol. 92, no. 3, pp. 401–422, Mar. 2004.

[30] S. Julier, J. Uhlmann, and H. F. Durrant-Whyte, "A new method for the nonlinear transformation of means and covariances in filters and estimators," *IEEE Trans. Automatic Control*, vol. 45, no. 3, pp. 477–482, Mar. 2000.

[31] R. Van Der Merwe and E. A. Wan, "The square-root unscented kalman filter for state and parameter-estimation," in *IEEE Int. Conf. Acoustics, Speech, and Signal Processing*, 2001, pp. 3461–3464.

[32] S. Holmes, G. Klein, and D. W. Murray, "A square root unscented kalman filter for visual monoslam," in *IEEE Int. Conf. Robotics and Automation*, 2008, pp. 3710–3716.

[33] S. Särkkä, "Unscented Rauch–Tung–Striebel smoother," *IEEE Trans. Automatic Control*, vol. 53, no. 3, pp. 845–849, Apr. 2008.

CHAPTER 5

DISCUSSION AND FUTURE WORK

This dissertation has explored advancements in closed-loop propulsion of wireless capsule endoscopes using magnetic fields. There are several possible directions to further advance this technology. This work briefly explored optimizing the trajectory of the actuator magnet (for forward capsule propulsion), but this field remains largely unstudied for applications in capsule endoscopy. For example, our current system described in Chapter 4 optimizes for a single time step and is only constrained by one obstacle. A clinical system would likely have a more complex workspace and expanding the time horizon of the optimization could provide a smoother trajectory by anticipating changes in direction based on an obstacle that would present itself in the future.

The current experiments detailed in this dissertation are limited by the size of the prototype capsule and SAMM devices. Possible future work includes designing a smaller prototype capsule that is at the exact scale of commercially available devices including a camera. Another active area of research involves trying to automatically classify features from the video taken by capsule endoscopes [1]. Currently, clinicians manually go through more than 50,000 images taken during the procedure and annotate those that are important [1, 2, 3]. While it is possible to localize the capsule based on the video stream, it is limited to the particular region (e.g., esophagus) [4]. Fusing the video data with the magnetic localization algorithms explored in Chapters 3 and 4 could potentially improve the overall capsule pose estimate. Alternatively, adding video data to the localization could give fixed waypoints in the gastrointestinal tract (e.g, pylorus) to further refine the localization estimate and its translation to the patient's gastrointestinal tract rather than relying on the relative distance between the actuator magnet and the capsule.

Although our current localization methods are sufficient for propelling the capsule online, clinicians may desire a more accurate estimate of the capsule's pose for procedures that result from data the capsule acquired (e.g., locating and removing a legion). A more

comprehensive process model may be used off-line in a post-processing step that does not restrict the capsule to translation along and rotation about its principle axis (e.g., allows rotation of the capsule's heading). Use of a more realistic model would likely improve the smoothing results given in Chapter 4.

Additionally, our results are limited to the small intestines, where the capsule is assumed to be constrained to a lumen. Prior work has used a single permanent magnet to levitate a magnetic capsule in a simulated fluid-filled stomach [5]. As it only provides 5-DOF control, it assumes the capsule's dipole moment will align with the externally applied field, and the capsule's magnet was placed parallel to the capsule's principle axis. No control is needed over rotation about its principle axis. To provide a full exploration of the gastrointestinal tract, exploring if this method could be reproduced with the same magnet placement used in this dissertation (the capsule's dipole moment perpendicular to the principle axis of the capsule) should be explored. Further, using similar methods of slowly aligning the capsule to a quasi-static field could provide additional degrees of freedom to control the capsule's heading (e.g., to image the entire intestinal wall in the colon).

Next steps should include developing a larger SAMM device that can actuate the capsule at clinically realistic distances (300 mm). This will enable further animal testing (e.g., navigating an entire porcine GI tract) and bring magnetic localization and propulsion closer to a feasible clinical system.

5.1 References

[1] M. T. Coimbra and J. P. S. Cunha, "Mpeg-7 visual descriptors - contributions for automated feature extraction in capsule endoscopy," *IEEE Trans on Circuits and Systems for Video Technology*, vol. 16, no. 5, pp. 628–637, May 2006.

[2] J. P. S. Cunha, M. Coimbra, P. Campos, and J. M. Soares, "Automated topographic segmentation and transit time estimation in endoscopic capsule exams," *IEEE Trans on Medical Imaging*, vol. 27, no. 1, pp. 19–27, Dec. 2008.

[3] A. Karargyris and N. Bourbakis, "Detection of small bowel polyps and ulcers in wireless capsule endoscopy videos," *IEEE Trans on Biomedical Engineering*, vol. 58, no. 10, pp. 2777–2786, May 2011.

[4] J. Bulat *et al.*, "Data processing tasks in wireless gi endoscopy: Image-based capsule localization & navigation and video compression," in *IEEE Int. Conf. Eng in Medicine and Biology Society*, 2007, pp. 2815–2818.

[5] A. W. Mahoney and J. J. Abbott, "Five-degree-of-freedom manipulation of an untethered magnetic device in fluid using a single permanent magnet with application in stomach capsule endoscopy," *Int. J of Robotics Research*, vol. 35, no. 1-3, pp. 129–147, Jan. 2015.

CHAPTER 6

CONCLUSION

This dissertation presents advancements in magnetic propulsion and localization of screw-type capsules. A complete optimized magnetic localization-propulsion system was presented that can successfully navigate complex trajectories in animal intestines.

A robotic end-effector that provides a singularity-free method of controlling a spherical permanent magnet to rotate about any arbitrary axis was described. This end-effector removes the need for a high-degree-of-freedom robotic arm and simplifies the control strategy by removing singularity constraints. Because it relies on a spherical permanent magnet, no inaccuracies are introduced into our localization models through the use of the simple point-dipole equation.

A prototype capsule was designed embedded with Hall-effect sensors to sense the capsule's regime in the field and provide information needed to localize the full 6-DOF capsule pose. The chosen sensor array layout increases the accuracy of the magnetic field readings by removing the need for large-range sensors used in prior work. Two localization methods were described. The first, used when the capsule has approximately no net motion, can localize the full 6-DOF capsule pose to within 4.9 ± 2.9 mm and 3.3 ± 1.7 degrees (mean $\pm$ standard deviation) across our tested workspace of 100 mm to 200 mm with no prior location information. The second method uses a square-root variant of the Unscented Kalman Filter to estimate the capsule's pose as it synchronously rotates with the applied field. A simplified process model was employed that restricted the capsule's movement along its principle axis. While the localization errors for the rotating capsule are higher with 11.4 ± 2.6 mm and 10.9 ± 0.9 degrees, it is sufficiently accurate to propel the capsule through complex trajectories.

A localization-propulsion system that uses the estimated capsule pose from either of the localization methods and then calculates the optimal pose of the actuator magnet to maximize the forward velocity of the capsule was described. An additional square-root

Unscented Kalman filter was implemented to estimate the capsule's propulsion parameters. The optimal pose of the actuator magnet changes based on the capsule's current movement in the field and is able to successfully navigate two trajectories in bovine intestines.

This dissertation's results show the feasibility of a single rotating dipole to successfully propel and localize a screw-type magnetic capsule in the intestines and encourages further study to create a clinically realistic magnetically actuated capsule endoscope.

APPENDIX A

QUATERNION REVIEW

Quaternions are an alternative to rotation matrices for representing orientations and rotations of Euclidean vectors [1]. Consider a rotation matrix $\mathbf{R}$, which can be represented in the angle-axis representation $(\theta, \hat{\mathbf{k}})$. A quaternion $\mathcal{Q}$ is a 4×1 vector that is constructed from the angle-axis representation:

$$\mathcal{Q} = \begin{bmatrix} q_0 \\ \mathbf{q} \end{bmatrix},\ q_0 = \cos\left(\frac{\theta}{2}\right),\ \mathbf{q} = \hat{\mathbf{k}}\sin\left(\frac{\theta}{2}\right) \tag{A.1}$$

where q_0 and $\mathbf{q}$ are the scalar and vector parts of the quaternion, respectively. A quaternion's conjugate is defined as

$$\mathcal{Q}^* = \begin{bmatrix} q_0 \\ -\mathbf{q} \end{bmatrix}. \tag{A.2}$$

Quaternion multiplication is not commutative and is defined as:

$$\mathcal{Q}\cdot\mathcal{K} = \begin{bmatrix} q_0 & -\mathbf{q}^{\mathsf{T}} \\ \mathbf{q} & q_0\mathbf{I}_3 + \mathrm{S}[\mathbf{q}] \end{bmatrix}\begin{bmatrix} k_0 \\ \mathbf{k} \end{bmatrix}. \tag{A.3}$$

Quaternions can be used in a similar fashion to rotation matrices to rotate any arbitrary vector $\boldsymbol{\nu}$ into a different coordinate frame by conjugating $\boldsymbol{\nu}$ by $\mathcal{Q}$ [2]:

$$\begin{aligned} {}^j\boldsymbol{\nu} &= {}^j\mathcal{Q}_i\,{}^i\boldsymbol{\nu}\,{}^j\mathcal{Q}_i^* \\ &= \left(q_0^2 - \mathbf{q}\cdot\mathbf{q}\right){}^i\boldsymbol{\nu} + 2q_0\mathbf{q}\times{}^i\boldsymbol{\nu} + 2\mathbf{q}\left(\mathbf{q}\cdot{}^i\boldsymbol{\nu}\right). \end{aligned} \tag{A.4}$$

The inverse rotation is performed in a similar way:

$$\begin{aligned} {}^j\boldsymbol{\nu} &= {}^j\mathcal{Q}_i^*\,{}^j\boldsymbol{\nu}\,{}^j\mathcal{Q}_i \\ &= \left(q_0^2 - \mathbf{q}\cdot\mathbf{q}\right){}^j\boldsymbol{\nu} + 2q_0\,{}^i\boldsymbol{\nu}\times\mathbf{q} + 2\mathbf{q}\left(\mathbf{q}\cdot{}^i\boldsymbol{\nu}\right). \end{aligned} \tag{A.5}$$

We frequently rotate vectors using quaternions in our process and measurement models in the Kalman filters, so the partial derivatives of (A.4) and (A.5) with respect to both $\mathcal{Q}$ and $\boldsymbol{\nu}$ are derived next.

$$\Pi(\boldsymbol{\nu}, \mathcal{Q}) = \frac{\partial \mathcal{Q}\boldsymbol{\nu}\mathcal{Q}^*}{\partial \mathcal{Q}} = \begin{bmatrix} \frac{\partial \mathcal{Q}\boldsymbol{\nu}\mathcal{Q}^*}{\partial q_0} & \frac{\partial \mathcal{Q}\boldsymbol{\nu}\mathcal{Q}^*}{\partial \mathbf{q}} \end{bmatrix} \tag{A.6}$$

where

$$\frac{\partial \mathcal{Q}\boldsymbol{\nu}\mathcal{Q}^*}{\partial q_0} = 2q_0\boldsymbol{\nu} + 2\mathbf{q} \times \boldsymbol{\nu} \tag{A.7}$$

$$\frac{\partial \mathcal{Q}\boldsymbol{\nu}\mathcal{Q}^*}{\partial \mathbf{q}} = 2\left(q_0 \mathbb{S}[\boldsymbol{\nu}]^\mathsf{T} + \mathbf{q}\boldsymbol{\nu}^\mathsf{T} + (\mathbf{q} \cdot \boldsymbol{\nu})\,\mathbf{I}_3 - \boldsymbol{\nu}\mathbf{q}^\mathsf{T}\right) \tag{A.8}$$

and

$$\Pi^*(\boldsymbol{\nu}, \mathcal{Q}) = \frac{\partial \mathcal{Q}^*\boldsymbol{\nu}\mathcal{Q}}{\partial \mathcal{Q}} = \begin{bmatrix} \frac{\partial \mathcal{Q}^*\boldsymbol{\nu}\mathcal{Q}}{\partial q_0} & \frac{\partial \mathcal{Q}^*\boldsymbol{\nu}\mathcal{Q}}{\partial \mathbf{q}} \end{bmatrix} \tag{A.9}$$

where

$$\frac{\partial \mathcal{Q}^*\boldsymbol{\nu}\mathcal{Q}}{\partial q_0} = 2q_0\boldsymbol{\nu} + 2\boldsymbol{\nu} \times \mathbf{q} \tag{A.10}$$

$$\frac{\partial \mathcal{Q}^*\boldsymbol{\nu}\mathcal{Q}}{\partial \mathbf{q}} = 2\left(q_0 \mathbb{S}[\boldsymbol{\nu}] + \mathbf{q}\boldsymbol{\nu}^\mathsf{T} + (\mathbf{q} \cdot \boldsymbol{\nu})\,\mathbf{I}_3 - \boldsymbol{\nu}\mathbf{q}^\mathsf{T}\right) \tag{A.11}$$

$$\Upsilon(\mathcal{Q}) = \frac{\partial \mathcal{Q}\boldsymbol{\nu}\mathcal{Q}^*}{\partial \boldsymbol{\nu}} = (q_0^2 - \mathbf{q} \cdot \mathbf{q})\mathbf{I}_3 + 2q_0\mathbb{S}[\mathbf{q}] + 2\mathbf{q}\mathbf{q}^\mathsf{T} \tag{A.12}$$

and

$$\Upsilon^*(\mathcal{Q}) = \frac{\partial \mathcal{Q}^*\boldsymbol{\nu}\mathcal{Q}}{\partial \boldsymbol{\nu}} = (q_0^2 - \mathbf{q} \cdot \mathbf{q})\mathbf{I}_3 + 2q_0\mathbb{S}[\mathbf{q}]^\mathsf{T} + 2\mathbf{q}\mathbf{q}^\mathsf{T}. \tag{A.13}$$

The partial derivative of a quaternion with respect to its rotation vector is also required for the EKF process model Jacobian. From [1], the derivative of a quaternion with respect to its rotation vector $\mathbf{k} = \theta\hat{\mathbf{k}}$ is:

$$\frac{\partial \mathcal{Q}}{\partial \mathbf{k}} = \frac{1}{2||\mathbf{k}||^3} \begin{bmatrix} -k_1\|\mathbf{k}\|^2 s_k & -k_2||\mathbf{k}||^2 s_k & -k_3||\mathbf{k}||^2 s_k \\ \sigma + k_1^2\epsilon & k_1k_2\epsilon & k_1k_3\epsilon \\ k_1k_2\epsilon & \sigma + k_2^2\epsilon & k_2k_3\epsilon \\ k_1k_3\epsilon & k_2k_3\epsilon & \sigma + k_3^2\epsilon \end{bmatrix} \tag{A.14}$$

where

$$s_k = \sin\left(\frac{\|\mathbf{k}\|}{2}\right) \tag{A.15}$$

$$\epsilon = \cos\left(\frac{\|\mathbf{k}\|}{2}\right)\|\mathbf{k}\| - 2s_k \tag{A.16}$$

$$\sigma = 2||\mathbf{k}||^2 s_k \tag{A.17}$$

and $\mathbf{k} = [k_1\ k_2\ k_3]^\mathsf{T}$.

A.1 References

[1] J. Diebel, "Representing attitude: Euler angles, unit quaternions, and rotation vectors," *Matrix*, vol. 58, no. 15-16, pp. 1–35, Oct. 2006.

[2] J. B. Kuipers, *Quaternions and Rotation Sequences - A Primer with Applications to Orbits, Aerospace, and Virtual Reality*, Princeton, N. J., USA: Princeton University Press, 1999.

APPENDIX B

ESTIMATING AVERAGE MAGNETIC FORCE AND TORQUE OVER ONE ROTATION

The magnetic torque (4.5) and force (4.6) generated by the point-dipole model (4.1) are functions of the actuator and capsule dipole moments, $\mathbf{m}_a$ and $\mathbf{m}_c$, and the relative position vector $\mathbf{p}_c$. They vary periodically (in magnitude and direction) as the actuator magnet and capsule rotate. How the magnetic torque and force vary depends on two factors: the lead angle α and the position direction $\hat{\mathbf{p}}_c$. Due to the assumption that the capsule dipole moment $\mathbf{m}_c$ and the applied field $\mathbf{b}_c$ are coplanar as they both rotate around $\hat{\mathbf{\Omega}}_c$, the direction of the capsule dipole moment can always be represented as a linear combination of a vector $\hat{\mathbf{b}}_c$ that is parallel to the applied field and a vector $\hat{\mathbf{b}}_c^{\perp} = \widehat{\mathbf{b}_c \times \hat{\mathbf{\Omega}}_c}$ that is orthogonal to the applied field:

$$\hat{\mathbf{m}}_c = \mathrm{c}(\alpha)\hat{\mathbf{b}}_c + \mathrm{s}(\alpha)\hat{\mathbf{b}}_c^{\perp} \tag{B.1}$$

where $\mathrm{c}(\alpha) = \cos(\alpha)$ and $\mathrm{s}(\alpha) = \sin(\alpha)$.

Representing $\hat{\mathbf{m}}_c$ in this way is useful since both the magnetic torque $\boldsymbol{\tau}$ and the magnetic force $\mathbf{f}$ are linear with respect to $\hat{\mathbf{m}}_c$. By substituting (B.1) into (4.5) and (4.6), it is clear that the magnetic torque and force can be represented as linear combinations of the torque and force produced when the capsule's dipole moment is parallel to $\hat{\mathbf{b}}_c$ and $\hat{\mathbf{b}}_c^{\perp}$, respectively:

$$\boldsymbol{\tau} = \mathrm{c}(\alpha)\gamma_1 \mathbf{T}\hat{\mathbf{b}}_c + \mathrm{s}(\alpha)\gamma_1 \mathbf{T}\hat{\mathbf{b}}_c^{\perp} = \mathrm{s}(\alpha)\boldsymbol{\tau}^{\perp} \tag{B.2}$$

$$\mathbf{f} = \mathrm{c}(\alpha)\gamma_2 \mathbf{F}\hat{\mathbf{b}}_c + \mathrm{s}(\alpha)\gamma_2 \mathbf{F}\hat{\mathbf{b}}_c^{\perp} = \mathrm{c}(\alpha)\mathbf{f}^{\parallel} + \mathrm{s}(\alpha)\mathbf{f}^{\perp}, \tag{B.3}$$

where $\mathbf{T}$ is defined in (4.5), $\mathbf{F}$ is defined in (4.6), and the scalars γ_1 and γ_2 are from (4.8) and (4.9), respectively. $\boldsymbol{\tau}^{\perp}$ is the magnetic torque resulting from the component of $\mathbf{m}_c$ parallel to $\hat{\mathbf{b}}_c^{\perp}$, and $\mathbf{f}^{\perp}$ and $\mathbf{f}^{\parallel}$ are the components of magnetic force resulting from the

components of $\mathbf{m}_c$ parallel to $\hat{\mathbf{b}}_c^{\perp}$ and $\hat{\mathbf{b}}_c$, respectively. Note that there is no magnetic torque component resulting from the component of the capsule dipole moment parallel to $\hat{\mathbf{b}}_c$. Representing the magnetic torque and force in this manner decouples analysis for any lead angle α into the analysis of the magnetic torque and force when the capsule dipole moment $\mathbf{m}_c$ is parallel and orthogonal to the applied field $\mathbf{b}_c$ as they both rotate.

Substituting $\hat{\mathbf{b}}_c^{\perp}$ into (4.5) results in the expression for $\boldsymbol{\tau}^{\perp}$ as:

$$\boldsymbol{\tau}^{\perp} = \gamma_1 \|\mathbf{B}_c \hat{\mathbf{m}}_{\mathbf{a}}\| \hat{\boldsymbol{\Omega}}_c. \tag{B.4}$$

Note that $\boldsymbol{\tau}^{\perp}$ is parallel to $\hat{\boldsymbol{\Omega}}_c$ since we have assumed that $\hat{\mathbf{m}}_c$ and $\mathbf{b}_c$ are coplanar through each rotation of $\mathbf{b}_c$ and must also be mutually orthogonal to $\hat{\boldsymbol{\Omega}}_c$ [1].

Substituting $\hat{\mathbf{b}}_c^{\perp}$ and $\hat{\mathbf{b}}_c$ into (4.6) for $\hat{\mathbf{m}}_c$ results in the expressions for $\mathbf{f}^{\perp}$ and $\mathbf{f}^{\parallel}$ as:

$$\begin{aligned}\mathbf{f}^{\perp} = \frac{\gamma_2}{2\|\mathbf{B}_c \hat{\mathbf{m}}_a\| \|\mathbf{B}_c^{-1} \hat{\boldsymbol{\Omega}}_{\mathbf{a}}\|} \Big(& 3(\hat{\mathbf{m}}_a^{\mathsf{T}} \hat{\mathbf{p}}_c)^2 \mathbf{d} - \Big((\hat{\mathbf{m}}_a^{\mathsf{T}} \hat{\mathbf{p}}_c) \mathbf{I}_3 \\ & + (\hat{\mathbf{m}}_a^{\mathsf{T}} \hat{\mathbf{p}}_c) \hat{\mathbf{p}}_c \hat{\mathbf{p}}_c^{\mathsf{T}} - 2 \hat{\mathbf{m}}_a \hat{\mathbf{p}}_c^{\mathsf{T}} \Big) \hat{\mathbf{m}}_a^{\perp} \Big)\end{aligned} \tag{B.5}$$

$$\mathbf{f}^{\parallel} = \frac{\gamma_2}{\|\mathbf{B}_c \hat{\mathbf{m}}_a\|} \Big(\hat{\mathbf{m}}_a \hat{\mathbf{m}}_a^{\mathsf{T}} - \Big(1 + 4(\hat{\mathbf{p}}_c^{\mathsf{T}} \hat{\mathbf{m}}_a)^2 \Big) \mathbf{I}_3 \Big) \hat{\mathbf{p}}_c \tag{B.6}$$

where

$$\mathbf{d} = \hat{\boldsymbol{\Omega}}_a \times \hat{\mathbf{p}}_c \tag{B.7}$$

$$\hat{\mathbf{m}}_a^{\perp} = \hat{\mathbf{m}}_a \times \hat{\boldsymbol{\Omega}}_a. \tag{B.8}$$

The magnetic force component $\mathbf{f}^{\parallel}$ tends to be generally attractive in nature and $\mathbf{f}^{\perp}$ tends to generally point in the same direction as $\mathbf{d}$ (i.e., neither attractive nor repulsive) for any position $\mathbf{p}_c$.

To calculate the average magnetic torque $\bar{\boldsymbol{\tau}}$ and the average magnetic force $\bar{\mathbf{f}}$, first the parallel and orthogonal components are derived with equations (B.9), (B.11), (B.14). These derivations assume the lead angle and the position offset remain constant throughout one complete rotation of the actuator magnet. Note, it is unlikely that α remains constant through one rotation unless the actuator's speed is actively controlled for this purpose, if α varies $\bar{\boldsymbol{\tau}}$ and $\bar{\mathbf{f}}$ provide an approximation assuming a nominal α. The total average torque and force, can be broken into components resulting from the capsule dipole moment being orthogonal and parallel to the rotating applied field.

The average magnetic torque when the capsule moment is orthogonal to the applied field (such that $\alpha = 90^\circ$) is denoted by $\bar{\boldsymbol{\tau}}^\perp$, and is calculated as:

$$\bar{\boldsymbol{\tau}}^\perp = \frac{1}{2\pi}\oint_{2\pi} \boldsymbol{\tau}^\perp \mathrm{d}\mathbf{m}_a = \frac{2\gamma_1}{\pi\sqrt{1-\phi}} E(\phi)\hat{\boldsymbol{\Omega}}_c \tag{B.9}$$

where

$$\phi = 3\|\mathbf{d}\|^2/(1+3\|\mathbf{d}\|^2) \tag{B.10}$$

ϕ is bounded by $0 \leq \phi \leq 3/4$ and $E(\phi)$ is a complete elliptic integral of the second kind. Note that, except for a few special cases, there are no closed-form evaluations of elliptic integrals, although efficient numerical methods are provided in most computational mathematics software packages to compute them.

The average magnetic force when the capsule moment is parallel to the applied field ($\alpha = 0^\circ$) is denoted by $\bar{\mathbf{f}}^\parallel$ and is

$$\bar{\mathbf{f}}^\parallel = \frac{1}{2\pi}\oint_{2\pi} \mathbf{f}^\parallel \mathrm{d}\mathbf{m}_a = \frac{2\gamma_2}{\pi}\Big(\bar{\mathbf{M}} - (\bar{m} + 4\hat{\mathbf{p}}_c^\mathsf{T}\bar{\mathbf{M}}\hat{\mathbf{p}}_c)\mathbf{I}_3\Big)\hat{\mathbf{p}}_c \tag{B.11}$$

where

$$\bar{\mathbf{M}} = \frac{\sqrt{1-\phi}}{\phi}\Big(E(\phi) + (\phi-1)K(\phi)\Big)\hat{\mathbf{e}}\hat{\mathbf{e}}^\mathsf{T} \tag{B.12}$$

$$\bar{m} = \sqrt{1-\phi}K(\phi) \tag{B.13}$$

$\hat{\mathbf{e}} = \left(\mathbf{I}_3 - \hat{\boldsymbol{\Omega}}_a\hat{\boldsymbol{\Omega}}_a^\mathsf{T}\right)\hat{\mathbf{p}}_c$ and $K(\phi)$ is the complete elliptic integral of the first kind. The average magnetic force when the capsule moment is orthogonal to the applied field ($\alpha = 90^\circ$) is denoted by $\bar{\mathbf{f}}^\perp$ and is given by

$$\begin{aligned}\bar{\mathbf{f}}^\perp &= \frac{1}{2\pi}\oint_{2\pi} \mathbf{f}^\perp \mathrm{d}\hat{\mathbf{m}}_a \\ &= \frac{2\gamma_2}{\pi\phi}\Big((2\phi-1)E(\phi) - (\phi-1)K(\phi)\Big)\mathbf{d},\end{aligned} \tag{B.14}$$

which points entirely in the direction of $\mathbf{d}$ (from (B.7)) for all capsule positions.

Note that the path taken by $\mathbf{m}_a$ in the contour integrals (B.9), (B.11), and (B.14) does not vary in time. In reality, it is possible that the trajectory of $\mathbf{m}_a$ may vary in time (e.g., to control the lead angle α). The result of the integrals (B.9), (B.11), and (B.14), in time, will be preserved if the trajectory of $\mathbf{m}_a$, beginning at time t_0 and end at time t_1, satisfies the integral

$$\int_{t_0}^{t_1} \mathbf{m}_a(t)\mathrm{d}t = \mathbf{0}. \tag{B.15}$$

The orthogonal and parallel components of torque (B.9) and force ((B.14) and (B.11)) are combined to find the total average torque and force for *any* constant α:

$$\bar{\boldsymbol{\tau}} = \sin(\alpha)\bar{\boldsymbol{\tau}}^{\perp} \tag{B.16}$$

$$\bar{\mathbf{f}} = \sin(\alpha)\bar{\mathbf{f}}^{\perp} + \cos(\alpha)\bar{\mathbf{f}}^{\parallel} \tag{B.17}$$

Note $\bar{\boldsymbol{\tau}}^{\perp}$, $\bar{\mathbf{f}}^{\parallel}$, and $\bar{\mathbf{f}}^{\perp}$ were derived with the assumption that α and $\mathbf{p}_c$ remain constant through one rotation of the actuator magnet, so these assumptions are inherent to the total average magnetic torque and magnetic force as well.

Figure B.1 shows the accuracy of the averaged magnetic torque and force as an approximation to the instantaneous torque and force as the actuator magnet rotates. Figure B.1(a) shows the maximum, minimum, and range of the error between the average magnetic force and the instantaneous magnetic force normalized by $2\gamma_2$ over one actuator-magnet revolution for varying capsule positions, parameterized by the angle between $\hat{\boldsymbol{\Omega}}_a$ and $\hat{\mathbf{p}}_c$, θ, and lead angles α. The force error is largest in radial positions ($\theta = 90^\circ$) and when the capsule dipole moment is aligned with the rotating field ($\alpha = 0^\circ$). This is the same configuration that maximizes the applied force magnitude.

Figure B.1(b) shows the maximum, minimum, and range of the error between the average magnetic torque and the instantaneous magnetic torque normalized by $2\gamma_1$ over one actuator-magnet revolution for varying capsule positions θ and lead angles α. The minimum normalized torque error is 0 for all configurations of θ and α, which makes the range of the normalized torque error equivalent to the maximum normalized torque error. Comparing Figs. B.1(a) and B.1(b) shows that averaging better approximates the applied magnetic force than the applied magnetic torque, in general.

B.1 References

[1] A. W. Mahoney and J. J. Abbott, "Generating rotating magnetic fields with a single permanent magnet for propulsion of untethered magnetic devices in a lumen," *IEEE Trans. Robotics*, vol. 30, no. 2, pp. 411–420, Apr. 2014.

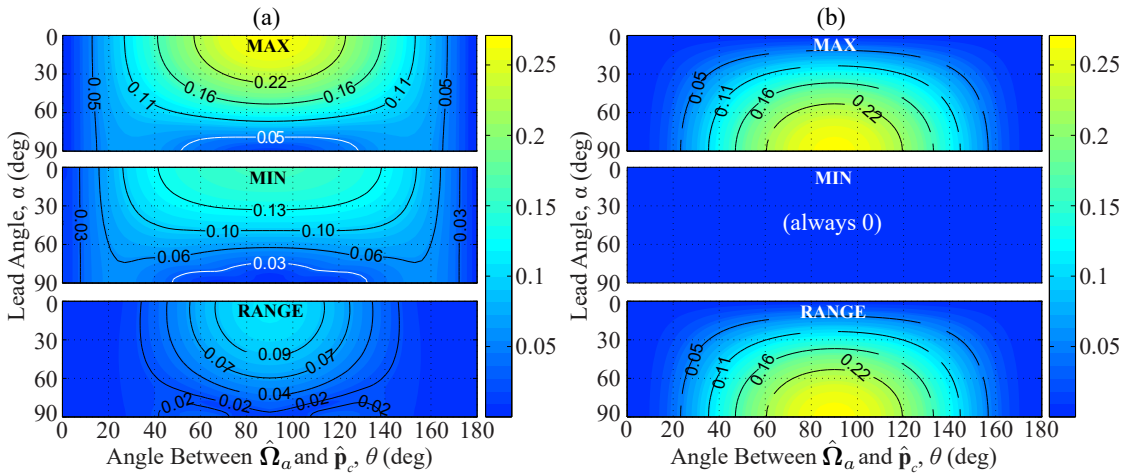

Figure B.1. Illustrates the accuracy of using the average magnetic force and torque to represent the instantaneous magnetic force and torque. (a) The maximum, minimum, and range of the error between the instantaneous magnetic force, $\mathbf{f}$, and the average magnetic force over one actuator-magnet revolution, $\bar{\mathbf{f}}$, normalized by $2\gamma_2$ (i.e., $\|\mathbf{f} - \bar{\mathbf{f}}\|/2\gamma_2$), plotted as a function of the capsule's position relative to the actuator magnet parameterized by θ and the lead angle α. (b) The maximum, minimum, and range of the error between the instantaneous magnetic torque, $\boldsymbol{\tau}$, and the average magnetic torque over one actuator–magnet revolution, $\bar{\boldsymbol{\tau}}$, normalized by $2\gamma_1$ (i.e., $\|\boldsymbol{\tau} - \bar{\boldsymbol{\tau}}\|/2\gamma_1$).

APPENDIX C

ANALYTIC SOLUTIONS FOR PARTIAL DERIVATIVES USED IN SQP

The magnitude of capsule's average spatial velocity is derived from (4.14) as:

$$\|\bar{\mathbf{v}}_c\| = \lambda_1 \hat{\mathbf{l}}^\mathsf{T} \bar{\mathbf{f}} + \lambda_2 \hat{\mathbf{l}}^\mathsf{T} \bar{\boldsymbol{\tau}}. \tag{C.1}$$

This can be rewritten by projecting the average magnetic force (B.17) onto $\hat{\mathbf{l}}$ and recognizing that $\hat{\mathbf{l}}^\mathsf{T} \bar{\mathbf{f}}^\perp = 0$ because we have assumed that the actuator magnet's rotation axis $\hat{\boldsymbol{\Omega}}_a$ is set so the field rotation axis $\hat{\boldsymbol{\Omega}}_c$ is aligned with the lumen axis $\hat{\mathbf{l}}$, and then substituting (B.16) into (C.1) for $\bar{\boldsymbol{\tau}}$, which produces

$$\|\bar{\mathbf{v}}_c\| = \lambda_1 \hat{\mathbf{l}}^\mathsf{T} \bar{\mathbf{f}}^\parallel c(\alpha) + \lambda_2 \hat{\mathbf{l}}^\mathsf{T} \bar{\boldsymbol{\tau}}^\perp s(\alpha). \tag{C.2}$$

The optimization with SQP utilizes the quadratic of the average velocity, which can be written as:

$$\begin{aligned} \|\bar{\mathbf{v}}_c\|^2 = &\left(\lambda_1 \left(\hat{\mathbf{l}}^\mathsf{T} \bar{\mathbf{f}}^\parallel\right) c(\alpha)\right)^2 + 2\lambda_1\lambda_2 \left(\hat{\mathbf{l}}^\mathsf{T} \bar{\mathbf{f}}^\parallel\right) \left(\hat{\mathbf{l}}^\mathsf{T} \bar{\boldsymbol{\tau}}^\perp\right) s(\alpha)c(\alpha) \\ &+ \left(\lambda_2 \left(\hat{\mathbf{l}}^\mathsf{T} \bar{\boldsymbol{\tau}}^\perp\right) s(\alpha)\right)^2. \end{aligned} \tag{C.3}$$

Since neither $\bar{\mathbf{f}}^\parallel$ nor $\bar{\boldsymbol{\tau}}^\perp$ is a function of α, the partial derivative of $\|\bar{\mathbf{v}}_c\|^2$ with respect to α is simply:

$$\begin{aligned} \frac{\partial \|\bar{\mathbf{v}}_c\|^2}{\partial \alpha} = &2\lambda_1\lambda_2 \left(\hat{\mathbf{l}}^\mathsf{T} \bar{\mathbf{f}}^\parallel\right) \left(\hat{\mathbf{l}}^\mathsf{T} \bar{\boldsymbol{\tau}}^\perp\right) \left(c^2(\alpha) - s^2(\alpha)\right) \\ &+ 2s(\alpha)c(\alpha)\left[\left(\lambda_2 \hat{\mathbf{l}}^\mathsf{T} \bar{\boldsymbol{\tau}}^\perp\right)^2 - \left(\lambda_1 \hat{\mathbf{l}}^\mathsf{T} \bar{\mathbf{f}}^\parallel\right)^2\right]. \end{aligned} \tag{C.4}$$

To calculate the partial derivative of $\|\mathbf{v}_c\|$ with respect to $\mathbf{o}_r$, we start by finding the partial derivative with respect to the position vector $\mathbf{p}_c$, because the magnetic force and torque are written in terms of $\mathbf{p}_c$. The partial derivatives of $\bar{\boldsymbol{\tau}}^\perp$ from (B.9) and of $\bar{\mathbf{f}}^\parallel$ from (B.11) with respect to $\mathbf{p}_c$:

$$\frac{\partial \bar{\boldsymbol{\tau}}^{\perp}}{\partial \mathbf{p}_c} = w_1 \hat{\boldsymbol{\Omega}}_c \Big(E \hat{\mathbf{p}}_c + \frac{E - (1-\phi)K}{4\phi(1-\phi)} \hat{\boldsymbol{\Omega}}_c^{\mathsf{T}} \hat{\mathbf{p}}_c \mathbf{W}_1 \hat{\boldsymbol{\Omega}}_c \Big)^{\mathsf{T}} \tag{C.5}$$

$$\frac{\partial \bar{\mathbf{f}}^{\parallel}}{\partial \mathbf{p}_c} = \frac{2\gamma_2}{\pi} \Bigg(-5\big(\bar{\mathbf{M}} - (\bar{m} + 4\hat{\mathbf{p}}_c^{\mathsf{T}} \bar{\mathbf{M}} \hat{\mathbf{p}}_c)\mathbf{I}_3\big) \frac{\hat{\mathbf{p}}_c \hat{\mathbf{p}}_c^{\mathsf{T}}}{\|\mathbf{p}_c\|} + \frac{1}{\|\mathbf{p}_c\|} \big(\mathbf{W}_2 - \mathbf{W}_3 - 4\mathbf{W}_4\big) \Bigg) \tag{C.6}$$

where

$$w_1 = \frac{-6\gamma_1}{\sqrt{1-\phi}\|\mathbf{p}_c\|\pi} \tag{C.7}$$

$$\mathbf{W}_1 = \mathbf{I}_3 - \hat{\mathbf{p}}_c \hat{\mathbf{p}}_c^{\mathsf{T}} \tag{C.8}$$

$$\mathbf{W}_2 = w_2 \mathbf{W}_5 \hat{\mathbf{p}}_c \mathbf{w}_1^{\mathsf{T}} + w_3 (\mathbf{W}_5 - \mathbf{W}_6 \mathbf{W}_7) \tag{C.9}$$

$$\mathbf{W}_3 = \frac{3\,(K-E)}{4\phi\sqrt{1-\phi}} \hat{\mathbf{p}}_c \hat{\mathbf{p}}_c^{\mathsf{T}} \boldsymbol{\Omega}_c \boldsymbol{\Omega}_c^{\mathsf{T}} \mathbf{W}_1 + \sqrt{1-\phi} K \mathbf{I}_3 \tag{C.10}$$

$$\mathbf{W}_4 = \mathbf{p}_c \mathbf{w}_2^{\mathsf{T}} + w_3 \left(1 - \left(\hat{\mathbf{p}}_c^{\mathsf{T}} \boldsymbol{\Omega}_a\right)^2\right) \mathbf{I}_3 \tag{C.11}$$

$$w_2 = \frac{(\phi - 2)\,E + 2\,(1-\phi)\,K}{2\phi^2\sqrt{1-\phi}} \tag{C.12}$$

$$w_3 = \frac{\sqrt{1-\phi}}{\phi}\,(E - (1-\phi)K) \tag{C.13}$$

$$\mathbf{w}_1 = -1.5 \left(\boldsymbol{\Omega}_c^{\mathsf{T}} \hat{\mathbf{p}}_c\right) \mathbf{W}_1 \boldsymbol{\Omega}_c \tag{C.14}$$

$$\mathbf{w}_2 = -2w_3 \left(1 - \left(\hat{\mathbf{p}}_c^{\mathsf{T}} \boldsymbol{\Omega}_a\right)^2\right) \frac{\hat{\mathbf{p}}_c}{\|\mathbf{p}_c\|} + \frac{\mathbf{w}_3}{\|\mathbf{p}_c\|^2} \tag{C.15}$$

$$\mathbf{W}_5 = \mathbf{I}_3 - \hat{\boldsymbol{\Omega}}_a \hat{\boldsymbol{\Omega}}_a^{\mathsf{T}} \tag{C.16}$$

$$\mathbf{W}_6 = \boldsymbol{\Omega}_a \hat{\mathbf{p}}_c^{\mathsf{T}} + (\hat{\mathbf{p}}_c^{\mathsf{T}} \boldsymbol{\Omega}_a)\mathbf{I}_3 \tag{C.17}$$

$$\mathbf{W}_7 = \frac{3\mathbf{W}_5 \mathbf{W}_8 \mathbf{W}_1}{\sqrt{1 + 3\left(\boldsymbol{\Omega}_c^{\mathsf{T}} \hat{\mathbf{p}}_c\right)^2}} \tag{C.18}$$

$$\mathbf{W}_8 = \left(\hat{\mathbf{p}}_c^{\mathsf{T}} \boldsymbol{\Omega}_c\right) \mathbf{I}_3 + \hat{\mathbf{p}}_c \boldsymbol{\Omega}_c^{\mathsf{T}} \tag{C.19}$$

$$\mathbf{w}_3 = \frac{-3w_2}{2\|\mathbf{p}_c\|} \left(\boldsymbol{\Omega}_c^{\mathsf{T}} \hat{\mathbf{p}}_c\right) \mathbf{W}_1 \boldsymbol{\Omega}_c \left(\mathbf{p}_c^{\mathsf{T}} \mathbf{p}_c - \left(\mathbf{p}_c^{\mathsf{T}} \boldsymbol{\Omega}_a\right)^2\right) + \left(\frac{\sqrt{1-\phi}}{\phi}\right) (E - (1-\phi)\,K)\,\mathbf{w}_4 \tag{C.20}$$

$$\mathbf{w}_4 = 2\left[\mathbf{p}_c - \left(\mathbf{p}_c^{\mathsf{T}} \boldsymbol{\Omega}_a\right) \left(\boldsymbol{\Omega}_a + \frac{1}{\|\mathbf{p}_c\|} \mathbf{W}_7^{\mathsf{T}} \mathbf{p}_c\right)\right] \tag{C.21}$$

$\bar{\mathbf{M}}$ is from (B.12), $\bar{m}$ is calculated with (B.13), K and E are the complete elliptic integrals of the first and second kind, which are functions of the scalar ϕ from (B.10). The partial

derivative of $\|\mathbf{v}_c\|^2$ with respect to $\mathbf{p}_c$ can then be written as:

$$\frac{\partial \|\bar{\mathbf{v}}_c\|^2}{\partial \mathbf{p}_c} = \frac{\partial \mathbf{w}_5}{\partial \mathbf{p}_c} + \frac{\partial \mathbf{w}_6}{\partial \mathbf{p}_c} + \frac{\partial \mathbf{w}_7}{\partial \mathbf{p}_c} \tag{C.22}$$

where

$$\frac{\partial \mathbf{w}_5}{\partial \mathbf{p}_c} = 2\lambda_1^2 \left(c(\alpha)\right)^2 \left(\hat{\mathbf{l}}^\mathsf{T} \mathbf{f}^{\|}\right) \hat{\mathbf{l}}^\mathsf{T} \frac{\partial \mathbf{f}^{\|}}{\partial \mathbf{p}_c} \tag{C.23}$$

$$\frac{\partial \mathbf{w}_6}{\partial \mathbf{p}_c} = 2\lambda_1 \lambda_2 c(\alpha) s(\alpha) \left[\left(\hat{\mathbf{l}}^\mathsf{T} \frac{\partial \mathbf{f}^{\|}}{\partial \mathbf{p}_c} \right) \left(\hat{\mathbf{l}}^\mathsf{T} \boldsymbol{\tau}^{\perp} \right) \right. \tag{C.24}$$

$$\left. + \left(\hat{\mathbf{l}}^\mathsf{T} \frac{\partial \bar{\boldsymbol{\tau}}^{\perp}}{\partial \mathbf{p}_c} \right) \left(\hat{\mathbf{l}}^\mathsf{T} \mathbf{f}^{\|} \right) \right] \tag{C.25}$$

$$\frac{\partial \mathbf{w}_7}{\partial \mathbf{p}_c} = 2\lambda_2^2 \left(s(\alpha)\right)^2 \left(\hat{\mathbf{l}}^\mathsf{T} \bar{\boldsymbol{\tau}}^{\perp}\right) \left(\hat{\mathbf{l}}^\mathsf{T} \frac{\partial \bar{\boldsymbol{\tau}}^{\perp}}{\partial \mathbf{p}_c} \right). \tag{C.26}$$

The partial derivative of $\|\bar{\mathbf{v}}_c\|^2$ with respect to $\mathbf{o}_r$ is calculated using the chain rule:

$$\frac{\partial \|\bar{\mathbf{v}}_c\|^2}{\partial \mathbf{o}_r} = \frac{\partial \|\bar{\mathbf{v}}_c\|^2}{\partial \mathbf{p}_c} \frac{\partial \mathbf{p}_c}{\partial \mathbf{o}_r} \tag{C.27}$$

where

$$\frac{\partial \mathbf{p}_c}{\partial \mathbf{o}_r} = -\mathbf{I}_3. \tag{C.28}$$

SQP also requires partial derivatives for the constraints, the first (4.16), can be written as:

$$\frac{\partial (\hat{\mathbf{l}} \cdot \mathbf{v}_c)}{\partial \mathbf{o}_r} = \hat{\mathbf{l}}^\mathsf{T} \left(\frac{\partial \mathbf{v}_c}{\partial \mathbf{p}_c} \frac{\partial \mathbf{p}_c}{\partial \mathbf{o}_r} \right) \tag{C.29}$$

where

$$\frac{\partial \mathbf{v}_c}{\partial \mathbf{p}_c} = \frac{\partial \mathbf{v}_c}{\partial \mathbf{f}} \frac{\partial \mathbf{f}}{\partial \mathbf{p}_c} + \frac{\partial \mathbf{v}_c}{\partial \boldsymbol{\tau}} \frac{\partial \boldsymbol{\tau}}{\partial \mathbf{p}_c}. \tag{C.30}$$

The pieces of the partial derivative of $\mathbf{v}_c$ with respect to $\mathbf{p}_c$ are derived in Appendix D. By replacing $\mathbf{p}_t$ with its definition, the partial derivative of the second constraint (4.17) can be written simply as:

$$\frac{\partial (\hat{\mathbf{n}} \cdot \mathbf{p}_t - p_{\min})}{\partial \mathbf{o}_r} = \frac{\partial (\hat{\mathbf{n}} \cdot (\mathbf{o}_r - \mathbf{o}_t) - p_{\min})}{\partial \mathbf{o}_r} = \hat{\mathbf{n}}^\mathsf{T}. \tag{C.31}$$

All constraint derivatives with respect to α are zero.

APPENDIX D

ANALYTIC SOLUTIONS FOR THE PROCESS MODEL JACOBIAN USED IN THE EXTENDED KALMAN FILTER

For compactness, throughout this appendix, all vectors should be assumed to be in the robot's r frame unless explicitly labeled otherwise. In addition, we will use $\mathbf{p} = \mathbf{p}_c$ and $\mathcal{Q} = {}^r\mathcal{Q}_c$. The partial derivatives of the quaternion rotation equations in (A.4) and (A.5) with respect to $\mathcal{Q}$ and the vector $\boldsymbol{\nu}$ are derived in Appendix A and are denoted here by the functions Π, Π^*, Y, and Y^*.

The Jacobian matrix for the process model function, $\mathbf{G}(\mathbf{s}, \mathbf{u})$, was derived and is given by:

$$\mathbf{G} = \begin{bmatrix} \frac{dG_{\mathbf{p}}}{d\mathbf{p}} & \frac{dG_{\mathbf{p}}}{d\mathcal{Q}} \\ \frac{dG_{\mathcal{Q}}}{d\mathbf{p}} & \frac{dG_{\mathcal{Q}}}{d\mathcal{Q}} \end{bmatrix} \tag{D.1}$$

where the four submatrices are defined as:

$$\frac{dG_{\mathbf{p}}}{d\mathbf{p}} = \frac{\partial G_{\mathbf{p}}}{\partial \mathbf{v}_c}\left(\frac{\partial \mathbf{v}_c}{\partial \mathbf{f}}\frac{\partial \mathbf{f}}{\partial \mathbf{p}} + \frac{\partial \mathbf{v}_c}{\partial \boldsymbol{\tau}}\frac{\partial \boldsymbol{\tau}}{\partial \mathbf{p}}\right) + \frac{\partial G_{\mathbf{p}}}{\partial \mathbf{p}} \tag{D.2}$$

$$\frac{dG_{\mathbf{p}}}{d\mathcal{Q}} = \frac{\partial G_{\mathbf{p}}}{\partial \mathbf{v}_c}\left(\frac{\partial \mathbf{v}_c}{\partial \mathbf{f}}\frac{\partial \mathbf{f}}{\partial \mathcal{Q}} + \frac{\partial \mathbf{v}_c}{\partial \boldsymbol{\tau}}\frac{\partial \boldsymbol{\tau}}{\partial \mathcal{Q}} + \frac{\partial \mathbf{v}_c}{\partial \mathcal{Q}}\right) \tag{D.3}$$

$$\frac{dG_{\mathcal{Q}}}{d\mathbf{p}} = \frac{\partial G_{\mathcal{Q}}}{\partial \boldsymbol{\omega}_c}\left(\frac{\partial \boldsymbol{\omega}_c}{\partial \mathbf{f}}\frac{\partial \mathbf{f}}{\partial \mathbf{p}} + \frac{\partial \boldsymbol{\omega}_c}{\partial \boldsymbol{\tau}}\frac{\partial \boldsymbol{\tau}}{\partial \mathbf{p}}\right) \tag{D.4}$$

$$\frac{dG_{\mathcal{Q}}}{d\mathcal{Q}} = \frac{\partial G_{\mathcal{Q}}}{\partial \boldsymbol{\omega}_c}\left(\frac{\partial \boldsymbol{\omega}_c}{\partial \mathbf{f}}\frac{\partial \mathbf{f}}{\partial \mathcal{Q}} + \frac{\partial \boldsymbol{\omega}_c}{\partial \boldsymbol{\tau}}\frac{\partial \boldsymbol{\tau}}{\partial \mathcal{Q}} + \frac{\partial \boldsymbol{\omega}_c}{\partial \mathcal{Q}}\right) + \frac{\partial G_{\mathcal{Q}}}{\partial \mathcal{Q}}. \tag{D.5}$$

If we rewrite the magnetic torque (4.5) as:

$$\boldsymbol{\tau} = \frac{\mu_0}{4\pi||\mathbf{p}||^3}\mathbf{m}_c \times (\mathbf{B}_c\mathbf{m}_a) = \frac{\mu_0}{4\pi||\mathbf{p}||^3}\mathrm{S}[\mathbf{m}_c]\mathbf{B}_c\mathbf{m}_a \tag{D.6}$$

the partial derivative of $\boldsymbol{\tau}$ with respect to $\mathcal{Q}$ and $\mathbf{p}$ can be written as:

$$\frac{\partial \boldsymbol{\tau}}{\partial \mathcal{Q}} = \frac{\mu_0}{4\pi||\mathbf{p}||^3}\mathrm{S}[\mathbf{B}_c\mathbf{m}_a]^{\mathsf{T}}\Pi({}^c\mathbf{m}_c, \mathcal{Q}) \tag{D.7}$$

$$\frac{\partial \boldsymbol{\tau}}{\partial \mathbf{p}} = \frac{3\mu_0}{4\pi}\mathbb{S}[\mathcal{Q}^c \mathbf{m}_c \mathcal{Q}^*]\Bigg(\frac{\left((\mathbf{p}^\mathsf{T}\mathbf{m}_a)\mathbf{I}_3 + \mathbf{p}\mathbf{m}_a^\mathsf{T} + \mathbf{m}_a\mathbf{p}^\mathsf{T}\right)}{\|\mathbf{p}\|^5} - \frac{5(\mathbf{p}^\mathsf{T}\mathbf{m}_a)\mathbf{p}\mathbf{p}^\mathsf{T}}{\|\mathbf{p}\|^7}\Bigg) \tag{D.8}$$

where $\mathbf{B}_c$ is from (4.1).

The magnetic force (4.6) can be rewritten as:

$$\mathbf{f} = \frac{3\mu_0}{4\pi||\mathbf{p}||^4}\left(\mathbf{m}_a\mathbf{p}^\mathsf{T} + \mathbf{p}\mathbf{m}_a^\mathsf{T} + \left(\mathbf{p}^\mathsf{T}\mathbf{Z}\mathbf{m}_a\right)\mathbf{I}_3\right)\mathbf{m}_c \tag{D.9}$$

where $\mathbf{Z}$ is defined in (4.7), such that its partial derivative with respect to $\mathcal{Q}$ is calculated as:

$$\frac{\partial \mathbf{f}}{\partial \mathcal{Q}} = \frac{3\mu_0}{4\pi||\mathbf{p}||^4}\left(\mathbf{m}_a\hat{\mathbf{p}}^\mathsf{T} + (\mathbf{m}_a^\mathsf{T}\hat{\mathbf{p}})\mathbf{I}_3 + \hat{\mathbf{p}}\mathbf{m}_a^\mathsf{T}\mathbf{Z}^\mathsf{T}\right)\Pi({}^c\mathbf{m}_c, \mathcal{Q}). \tag{D.10}$$

The derivative of force with respect to $\mathbf{p}$ is calculated as:

$$\frac{\partial \mathbf{f}}{\partial \mathbf{p}} = \frac{\gamma_2}{||\mathbf{p}||}\Bigg(\mathbf{X} - 5\hat{\mathbf{p}}\hat{\mathbf{p}}^\mathsf{T}\mathbf{X} - 5\mathbf{X}\hat{\mathbf{p}}\hat{\mathbf{p}}^\mathsf{T} - 5\left(\hat{\mathbf{m}}_c^\mathsf{T}(3\hat{\mathbf{p}}\hat{\mathbf{p}}^\mathsf{T} - \mathbf{I}_3)\hat{\mathbf{m}}_a\right)\hat{\mathbf{p}}\hat{\mathbf{p}}^\mathsf{T}\Bigg) \tag{D.11}$$

where

$$\mathbf{X} = \hat{\mathbf{m}}_a\hat{\mathbf{m}}_c^\mathsf{T} + \hat{\mathbf{m}}_c\hat{\mathbf{m}}_a^\mathsf{T} + \left(\hat{\mathbf{m}}_c^\mathsf{T}\mathbf{Z}\hat{\mathbf{m}}_a\right)\mathbf{I}_3. \tag{D.12}$$

Using the current values of $\boldsymbol{\tau}$ and $\mathbf{f}$, the partial derivatives of the forward and angular velocities are found:

$$\frac{\partial \boldsymbol{\omega}_c}{\partial \boldsymbol{\tau}} = \boldsymbol{\Lambda}_3 \tag{D.13}$$

$$\frac{\partial \boldsymbol{\omega}_c}{\partial \mathbf{f}} = \boldsymbol{\Lambda}_2^\mathsf{T} \tag{D.14}$$

$$\frac{\partial \mathbf{v}_c}{\partial \boldsymbol{\tau}} = \boldsymbol{\Lambda}_2 \tag{D.15}$$

$$\frac{\partial \mathbf{v}_c}{\partial \mathbf{f}} = \boldsymbol{\Lambda}_1 \tag{D.16}$$

where $\boldsymbol{\Lambda}_1, \boldsymbol{\Lambda}_2$, and $\boldsymbol{\Lambda}_3$ are defined in terms of the scalars λ_1, λ_3, and λ_2 and the vector describing the lumen direction $\hat{\mathbf{l}}$ (see (4.13)).

In our setup, we assume the lumen and the principle axis of the capsule (${}^r\hat{\mathbf{x}}_c$) are aligned, such that $\hat{\mathbf{l}} = {}^r\mathcal{Q}_c{}^c\hat{\mathbf{x}}_c{}^r\mathcal{Q}_c^*$. The partial derivatives of the spatial and angular velocities with respect to $\mathcal{Q}$ can be written as:

$$\frac{\partial \mathbf{v}_c}{\partial \hat{\mathbf{I}}} = \lambda_1 \hat{\mathbf{I}}\mathbf{f}^\mathsf{T} + \lambda_1(\hat{\mathbf{I}}^\mathsf{T}\mathbf{f})\mathbf{I}_3 + \lambda_2 \hat{\mathbf{I}}\boldsymbol{\tau}^\mathsf{T} + \lambda_2(\hat{\mathbf{I}}^\mathsf{T}\boldsymbol{\tau})\mathbf{I}_3 \tag{D.17}$$

$$\frac{\partial \mathbf{v}_c}{\partial \mathcal{Q}} = \frac{\partial \mathbf{v}}{\partial \hat{\mathbf{I}}} \Pi({}^c\hat{\mathbf{x}}_c, \mathcal{Q}) \tag{D.18}$$

$$\frac{\partial \boldsymbol{\omega}_c}{\partial \hat{\mathbf{I}}} = \lambda_2 \hat{\mathbf{I}}\mathbf{f}^\mathsf{T} + \lambda_2(\hat{\mathbf{I}}^\mathsf{T}\mathbf{f})\mathbf{I}_3 + \lambda_3 \hat{\mathbf{I}}\boldsymbol{\tau}^\mathsf{T} + \lambda_3(\hat{\mathbf{I}}^\mathsf{T}\boldsymbol{\tau})\mathbf{I}_3 \tag{D.19}$$

$$\frac{\partial \boldsymbol{\omega}_c}{\partial \mathcal{Q}} = \frac{\partial \boldsymbol{\omega}_c}{\partial \hat{\mathbf{I}}} \Pi({}^c\hat{\mathbf{x}}_c, \mathcal{Q}). \tag{D.20}$$

The remaining partial derivatives for the position update are derived from (4.21):

$$\frac{\partial G_\mathbf{p}}{\partial \mathbf{v}_c} = \Delta t \; \mathbf{I}_3 \tag{D.21}$$

$$\frac{\partial G_\mathbf{p}}{\partial \mathbf{p}} = \mathbf{I}_3. \tag{D.22}$$

The following partial derivatives are calculated from the orientation update (4.22). $\mathcal{Q}_\Delta = [q_\Delta \; \mathbf{q}_\Delta^\mathsf{T}]^\mathsf{T}$ refers to the incremental change in orientation that is created using the capsule's speed over some time increment Δt with its rotation vector: $\mathbf{k}_\Delta = \Delta t \boldsymbol{\omega}_c$. Utilizing (A.14), we compute:

$$\frac{\partial G_\mathcal{Q}}{\partial \boldsymbol{\omega}_c} = \begin{bmatrix} q_0 & -\mathbf{q}^\mathsf{T} \\ \mathbf{q} & q_0\mathbf{I}_3 - \mathrm{S}[\mathbf{q}] \end{bmatrix} \frac{\partial \mathcal{Q}_\Delta}{\partial \mathbf{k}_\Delta} \Delta_t \tag{D.23}$$

$$\frac{\partial G_\mathcal{Q}}{\partial \mathcal{Q}} = \begin{bmatrix} q_\Delta & -\mathbf{q}_\Delta^\mathsf{T} \\ \mathbf{q}_\Delta & q_\Delta\mathbf{I}_3 + \mathrm{S}[\mathbf{q}_\Delta]^\mathsf{T} \end{bmatrix}. \tag{D.24}$$

APPENDIX E

ANALYTIC SOLUTIONS FOR THE MEASUREMENT MODEL JACOBIAN USED IN THE EXTENDED KALMAN FILTER

An explicit representation of the Jacobian matrix for the measurement model, $\mathbf{H}(\mathbf{s}, \mathbf{u})$, is given by:

$$\mathbf{H} = \begin{bmatrix} \frac{\partial H}{\partial \mathbf{p}} & \frac{\partial H}{\partial \mathcal{Q}} \end{bmatrix}. \tag{E.1}$$

The measurement model H_i can be rewritten in terms of $\mathbf{p}$ and $\mathcal{Q}$:

$$H_i = {}^c\hat{\boldsymbol{\beta}}^\mathsf{T} a \mathcal{Q}^* \mathbf{a}_i \mathcal{Q}^* \tag{E.2}$$

where

$$a = \frac{\mu_0}{4\pi \|\mathbf{p} + {}^r\boldsymbol{\delta}_i\|^5} \tag{E.3}$$

$${}^r\mathbf{a}_i = \left(3(\mathbf{p} + {}^r\boldsymbol{\delta}_i)(\mathbf{p} + {}^r\boldsymbol{\delta}_i)^\mathsf{T} - \mathbf{I}_3 \|\mathbf{p} + {}^r\boldsymbol{\delta}_i\|^2\right) \mathbf{m}_a \tag{E.4}$$

and ${}^r\boldsymbol{\delta}_i = \mathcal{Q}^c\boldsymbol{\delta}_i\mathcal{Q}^*$. By setting ${}^c\mathbf{a}_i = \mathcal{Q}^{*r}\mathbf{a}_i\mathcal{Q}$ the partial derivative of H_i with respect to ${}^w\mathbf{p}$ is calculated as:

$$\frac{\partial H_i}{\partial \mathbf{p}} = {}^c\boldsymbol{\beta}^{\mathsf{T}c}\mathbf{a}_i \frac{\partial a}{\partial \mathbf{p}} + a^c\boldsymbol{\beta}^\mathsf{T} \frac{\partial {}^c\mathbf{a}_i}{\partial \mathbf{p}} \tag{E.5}$$

$$\begin{aligned} \frac{\partial \mathbf{a}_i}{\partial \mathbf{p}} = {} & 3\left(\mathbf{I}_3\mathbf{p}^\mathsf{T}\mathbf{m}_a + \mathbf{p}\mathbf{m}_a^\mathsf{T} + {}^r\boldsymbol{\delta}_i\mathbf{m}_a^\mathsf{T} + {}^r\boldsymbol{\delta}_i{}^\mathsf{T}\mathbf{m}_a\mathbf{I}_3\right) \\ & - 2(\mathbf{m}_a\mathbf{p}^\mathsf{T} + \mathbf{m}_a{}^r\boldsymbol{\delta}_i{}^\mathsf{T}) \end{aligned} \tag{E.6}$$

$$\frac{\partial {}^c\mathbf{a}_i}{\partial \mathbf{p}} = \Upsilon^*(\mathcal{Q}) \frac{\partial {}^r\mathbf{a}_i}{\partial \mathbf{p}} \tag{E.7}$$

$$\frac{\partial a}{\partial \mathbf{p}} = \left(\frac{-5\mu_0}{4\pi}\right) \frac{\mathbf{p}^\mathsf{T} + {}^r\boldsymbol{\delta}_i{}^\mathsf{T}}{\|\mathbf{p} + {}^r\boldsymbol{\delta}_i\|^7}. \tag{E.8}$$

Similarly, the derivative of H with respect to $\mathcal{Q}$ is:

$$\frac{\partial H}{\partial \mathcal{Q}} = {}^c\boldsymbol{\beta}^{\mathsf{T}c}\mathbf{a}_i \frac{\partial a}{\partial \mathcal{Q}} + a^c\boldsymbol{\beta}^\mathsf{T} \frac{\partial {}^c\mathbf{a}_i}{d\mathcal{Q}} \tag{E.9}$$

$$\frac{\partial {}^c\mathbf{a}_i}{\partial \mathcal{Q}} = \Upsilon^*(\mathcal{Q}) \frac{\partial {}^r\mathbf{a}_i}{\partial \mathcal{Q}} + \Pi^*({}^r\mathbf{a}_i, \mathcal{Q}) \tag{E.10}$$

$$\frac{\partial^r \mathbf{a}_i}{\partial \mathcal{Q}} = 3\Bigg(\Big((\mathbf{p}^\mathsf{T}\mathbf{m}_a)\mathbf{I}_3 + {}^r\boldsymbol{\delta}_i\mathbf{m}_a^\mathsf{T} + ({}^r\boldsymbol{\delta}_i{}^\mathsf{T}\mathbf{m}_a)\mathbf{I}_3 + \mathbf{p}\mathbf{m}_a^\mathsf{T} \Big) - 2\left(\mathbf{m}_a\mathbf{p}^\mathsf{T} + \mathbf{m}_a{}^r\boldsymbol{\delta}_i{}^\mathsf{T} \right) \Bigg) \Pi({}^c\boldsymbol{\delta}_i, \mathcal{Q}) \tag{E.11}$$

$$\frac{\partial a}{\partial \mathcal{Q}} = \frac{\partial a}{\partial \mathbf{p}} \Pi({}^c\boldsymbol{\delta}_i, \mathcal{Q}). \tag{E.12}$$